CORA Cork Open Research Archive
Cartlann Taighde Oscailte Chorcaí

| | |
|---|---|
| Title | Development and control of electrified axle (eAxle) powertrains for all-terrain heavy-duty vehicles |
| Authors | Healy, Conor |
| Publication date | 2025 |
| Original Citation | Healyer, C. 2025. Development and control of electrified axle (eAxle) powertrains for all-terrain heavy-duty vehicles. PhD Thesis, University College Cork. |
| Type of publication | Doctoral thesis |
| Rights | © 2025, Conor Healy. - https://creativecommons.org/licenses/by-nc-nd/4.0/ |
| Download date | 2026-11-04 05:22:53 |
| Item downloaded from | https://hdl.handle.net/10468/17967 |



UCC
University College Cork, Ireland
Coláiste na hOllscoile Corcaigh

Ollscoil na hÉireann, Corcaigh

**National University of Ireland, Cork**




# Development and Control of Electrified Axle (eAxle) Powertrains for All-Terrain Heavy-Duty Vehicles

Thesis presented by:

**Conor Healy, B.E.**

**0000-0003-0565-1251**

for the degree of

**Doctor of Philosophy**

Supervised by Dr. John G. Hayes

Department of Electrical and Electronic Engineering

University College Cork

2025

**DECLARATION**

*"This is to certify that the work I am submitting is my own and has not been submitted for another degree, either at University College Cork or elsewhere. All external references and sources are clearly acknowledged and identified within the contents. I have read and understood the regulations of University College Cork concerning plagiarism."*

Conor Healy

## ABSTRACT

This thesis summarizes the design, control and validation of a modular electrified axle (eAxle) for all-terrain heavy-duty vehicle applications. The eAxle is designed for 4x4, 6x6 and 8x8 vehicle configurations but can also be used in drivelines where only some axles are powered, such as 6x4 and 8x6 vehicles. The eAxle maintains compatibility with an existing independent suspension system and is suitable for use in multiple on-highway and off-highway sectors, including agriculture, construction vehicles, forest machinery, fire trucks and mining and powered trailers. The eAxle can be used in series-hybrid, battery-electric and hydrogen fuel cell powertrains.

In Chapter 2, a novel method, based on axle loading and weight transfer for powertrain sizing, is proposed and validated through dynamometer testing. This is demonstrated by focusing on a 27-tonne 6x6 vehicle as a case study to determine the eAxle's tractive effort requirements for one of the possible vehicle applications. A novel weight transfer-based approach is used for determining the worst-case (most heavily loaded) axle operating conditions which in turn are used for sizing the powertrain. A three-speed transmission is required to meet the vehicle performance requirements. The performance of the hybrid 6x6 vehicle is evaluated at steady-state operating points and during transient acceleration events. The powertrain sizing method is validated through a comprehensive dynamometer testing program.

In Chapter 3, a novel eAxle packaging concept is developed. The eAxle uses an over-the-shoulder configuration where the pinion-gear, used to drive the differential, is located on the opposite side to the motor and transmission. This enables the eAxle to be packaged more symmetrically on each side of its driveshafts, a key enabler for meeting tight vehicle wheelbase requirements. The over-the-shoulder concept provides access to the pinion-gear's shaft, facilitating the installation of auxiliary drives on the pinion-gear side of the differential. The auxiliary drives include inboard parking brakes and ground-driven steering pumps, both of which are required to meet vehicle safety and redundancy requirements. The eAxle can be mounted with the motor facing the front or rear of the vehicle. This allows for more driveline packaging concepts to be considered and increases the vehicle's maximum approach angle.

In Chapter 4, an efficiency-optimized gear selection map is developed for the eAxle. Raw power loss data for the eAxle's inverter and motor system is analysed and processed allowing power loss and efficiency maps for the inverter and motor system to be developed. The resulting efficiency maps for each of the eAxle's gears are calculated and mapped to a common set of lookup vectors before the most efficient gear for each operating point is selected. While this gear selection map is optimal from an efficiency perspective, practical considerations prevent it from being directly implemented on vehicles. These issues are resolved by developing efficiency-derived upshift and downshift curves for each gear transition. The performance of these gear shift curves is compared with the efficiency-optimized map in simulation. Dynamometer testing is used to validate the gear selection strategies.

In Chapter 5, control algorithms are developed for vehicles with multiple modular eAxles. The algorithms are implemented on a Driveline Control Unit (DCU). The DCU acts as an interface between a vehicle integrator's Vehicle Control Unit (VCU) and the eAxle Control Units (EACUs). Some key DCU features include speed measurement, wheel-slip calculation, available torque calculation, torque vectoring, wheel-slip limitation, driveline efficiency optimization, gear selection and staggered gear-shifting. The DCU also provides additional benefits to vehicle integrators, such as reducing vehicle Controller Area Network (CAN) bus requirements and allowing the VCU to maintain a conventional torque control algorithm focused on vehicle-level torques. The latter is of particular importance for removing the barriers into the electrification space posed by distributed propulsion, a term used to describe a powertrain with multiple independent torque sources.

**ACKNOWLEDGEMENTS**

The author would like to thank Dr. John G. Hayes for his help, guidance and insight throughout the project. The collaboration with Timoney Technology through the design, development and testing of the eAxle was highly valuable. The author would like to acknowledge the Irish Research Council/Research Ireland for supporting this work. Finally, the author is particularly grateful for the family support received while undertaking this project.

## LIST OF PUBLICATIONS

### JOURNAL PAPERS

- C. Healy and J. G. Hayes, "Design and test of a modular 200 kW eAxle for all-terrain heavy-duty vehicle applications", *IEEE Transactions on Transportation Electrification*, under review.
- C. Healy and J. G. Hayes, "An efficiency-optimized automatic gear-selection map for a 200 kW modular eAxle", *IEEE Transactions on Transportation Electrification*, under review.

### CONFERENCE PAPERS

- C. Healy and J. G. Hayes, "Design of a modular e-axle for all-terrain heavy-duty applications considering gradient weight transfer", *IEEE Transportation Electrification Conference and Expo (ITEC)*, 2023.
- C. Healy and J. G. Hayes, "An efficiency-optimized gear-shift map to maximise the performance of a modular e-axle", *International Scientific Conference on Electric Power Engineering (EPE)*, 2024.
- C. Healy and J. G. Hayes, "Speed vectoring algorithms for drivelines with multiple modular e-axles", *International Scientific Conference on Electric Power Engineering (EPE)*, 2024.

### PATENTS

- C. Healy, D. McCarry, M. Doody and G. Fitzpatrick, "An eAxle", United Kingdom Patent GB2408020.2, Jun. 5, 2024, to be published.

## TABLE OF CONTENTS


1 Introduction ..... 1

1.1 Overview ..... 1

1.2 Thesis Objectives ..... 2

1.3 Thesis Structure ..... 2

1.4 General Background ..... 3

1.5 eAxle Specifications ..... 6

1.5.1 eAxle Hardware ..... 6

1.5.2 eAxle Control ..... 9

1.5.3 Driveline Integration ..... 10

2 Development and Validation of Novel Design Methodologies for Electrified Axles ..... 11

2.1 Abstract ..... 11

2.2 Vehicle Performance Requirements ..... 12

2.3 Weight Transfer ..... 16

2.4 Powertrain Sizing ..... 19

2.5 Transmission Design ..... 26

2.6 Vehicle Performance ..... 29

2.6.1 Constant-Speed Performance ..... 29

2.6.2 Acceleration Performance ..... 32

2.7 eAxle Testing ..... 34

2.7.1 eAxle Test Setup ..... 34

2.7.2 Accelerated Life Cycle Testing ..... 36

2.7.3 Grade Climb Testing ..... 38

2.7.4 Maximum Torque Testing ..... 41

2.8 Conclusions ..... 42

3 Optimized Packaging of Electrified Axles ..... 43

3.1 Abstract ..... 43

3.2 eAxle Packaging Background ..... 44

3.3 eAxle Features and Packaging ..... 47
3.4 Auxiliary Kits and Drives ..... 50
3.5 Vehicle Integration ..... 54
3.6 Conclusions ..... 56
4 Gear Selection Algorithms for Multiple Speed Electrified Axles ..... 57
4.1 Abstract ..... 57
4.2 Inverter and Motor Power Loss and Efficiency Maps ..... 58
4.3 eAxle Power Loss and Efficiency Maps ..... 60
4.4 eAxle Gear Selection Curves ..... 64
4.5 eAxle Testing ..... 70
4.5.1 eAxle Test Setup ..... 70
4.5.2 Traction and Regenerative Braking Profiles ..... 70
4.5.3 Peak Acceleration Profiles ..... 72
4.6 Conclusions ..... 73
5 Control of Drivelines with Multiple Electrified Axles ..... 75
5.1 Abstract ..... 75
5.2 Vehicle Control Architecture ..... 76
5.3 Speed Calculation Algorithm ..... 78
5.4 Available Torque Calculation Algorithm ..... 83
5.5 Torque Vectoring Algorithm ..... 83
5.6 Gear Selection Algorithm ..... 84
5.7 Driveline Control Unit Testing ..... 88
5.7.1 Software-in-the-Loop Testing ..... 88
5.7.2 Hardware-in-the-Loop Testing ..... 93
5.8 Conclusions ..... 93
6 Conclusions and Future Work ..... 95
6.1 Conclusions ..... 95
6.2 Limitations and Future Work ..... 96

## LIST OF FIGURES

Fig. 1.1. A demonstration model of the T9000e eAxle. 6

Fig. 1.2. An alternative view of the T9000e eAxle. 7

Fig. 1.3: A high-level eAxle powertrain layout. 8

Fig. 1.4: A CAD rendering of the eDifferential. 9

Fig. 1.5: A CAD rendering of 4x4, 6x6 and 8x8 drivelines. 10

Fig. 2.1. Vehicle speed vs. gradient specification. 13

Fig. 2.2. Diesel vehicle speed vs. time during maximum acceleration. 14

Fig. 2.3. Peak and continuous vehicle motive torque vs. gradient. 15

Fig. 2.4. Peak and continuous vehicle motive power vs. gradient. 15

Fig. 2.5. Axle loading (MT = metric tonnes) vs. gradient for a 6x6 vehicle travelling at constant speed. 18

Fig. 2.6. Axle loading (MT = metric tonnes) vs. acceleration for a 6x6 vehicle on a 0 % grade. 19

Fig. 2.7. Available torque vs. gradient. 20

Fig. 2.8. Available torque vs. acceleration. 21

Fig. 2.9. Axle torque to meet vehicle requirements vectored in proportion to weight distribution vs. gradient. 22

Fig. 2.10. Peak axle torque to meet vehicle requirements vectored equally where possible vs. gradient. 23

Fig. 2.11. Case study vehicle axle 3 torque specification vs. axle angular speed. 23

Fig. 2.12. Case study vehicle axle 3 power specification vs. axle angular speed. 24

Fig. 2.13. eAxle torque specification vs axle angular speed. 25

Fig. 2.14. eAxle power specification vs. axle angular speed. 25

Fig. 2.15. eAxle torque curves at 650 $V_{DC}$ and a 65 °C coolant temperature. 26

Fig. 2.16. eAxle power curves at 650 $V_{DC}$ and a 65 °C coolant temperature. 27

Fig. 2.17. Combined eAxle torque curve and axle requirements at 650 $V_{DC}$ and a 65 °C coolant temperature. 28

Fig. 2.18. Combined eAxle power curve and axle requirements at 650 $V_{DC}$ and a 65 °C coolant temperature. 28

Fig. 2.19. Available torque vs. gradient. ..... 30

Fig. 2.20. Available torque vs. acceleration. ..... 30

Fig. 2.21. On-road 3D torque map. ..... 31

Fig. 2.22. On-road peak and continuous speed vs. grade. ..... 32

Fig. 2.23. Vehicle speed vs. time for maximum peak and continuous accelerations. ..... 33

Fig. 2.24. eDifferential test hardware without plumbing and instrumentation. ..... 34

Fig. 2.25. eDifferential dynamometer test setup. ..... 35

Fig. 2.26. Torque, speed and gear selection vs. time (hh:mm:ss) for the traction and regenerative braking cycle. ..... 37

Fig. 2.27. DC supply voltage and inverter current vs. time (hh:mm:ss) for a traction and regenerative braking cycle. ..... 37

Fig. 2.28. Component temperatures vs. time (hh:mm) for many traction and regenerative braking cycles. ..... 38

Fig. 2.29. Torque, speed and gear selection vs. time for a single grade climb. ..... 39

Fig. 2.30. DC supply voltage and inverter current vs. time for a single grade climb. ..... 40

Fig. 2.31. Component temperatures vs. time for five grade-climbs. ..... 40

Fig. 2.32. Torque, speed and gear selection vs. time for five maximum torque cycles. ..... 41

Fig. 2.33. DC supply voltage and inverter current vs. time for five maximum torque cycles. ..... 42

Fig. 3.1. A parallel one motor per-axle configuration. ..... 44

Fig. 3.2. A perpendicular one motor per-axle configuration. ..... 44

Fig. 3.3. A parallel one motor per-wheel configuration. ..... 45

Fig. 3.4. A perpendicular one motor per-wheel configuration. ..... 45

Fig. 3.5. An in-hub motor configuration. ..... 46

Fig. 3.6. eAxle features. ..... 47

Fig. 3.7. eAxle subassemblies. ..... 48

Fig. 3.8. eAxle power flow. ..... 50

Fig. 3.9. eAxle auxiliary kits and drives. ..... 51

Fig. 3.10. An eDifferential with the ground-driven emergency steering pump kit. ..... 52

Fig. 3.11. An eDifferential with the tandem spring-applied hydraulic-release inboard parking brake and ground-driven emergency steering pump kit. ..... 52

Fig. 3.12. Axle and vehicle parking brake torques vs. gradient. ..... 53

Fig. 3.13. Vehicle parking brake torque and hill hold requirement vs. gradient. ..... 54

Fig. 3.14. An 8x8 driveline layout with all eAxles orientated rearward. ..... 55

Fig. 3.15. An 8x8 driveline layout with two eAxles orientated forward and two eAxles oreintated rearward. ..... 55

Fig. 4.1. Inverter and motor system power loss map showing missing data. ..... 59

Fig. 4.2. Combined inverter and motor system power loss map. ..... 60

Fig. 4.3. Combined inverter and motor system efficiency map. ..... 60

Fig. 4.4. eAxle peak and continuous torque curves for individual gears. ..... 61

Fig. 4.5. Efficiency-optimized gear shift map (red - first gear, green - second gear, blue - third gear). ..... 62

Fig. 4.6. Efficiency-optimized eAxle power loss map. ..... 63

Fig. 4.7. Efficiency-optimized eAxle efficiency map. ..... 63

Fig. 4.8. Efficiency-optimized gear shift map with minimum gear speeds (red - first gear, green - second gear, blue - third gear). ..... 64

Fig. 4.9. Efficiency-optimized gear-shift curves with minimum gear speeds ..... 65

Fig. 4.10. Automatic gear-shifting curves ..... 65

Fig. 4.11. Automatic gear-shifting curves and boundary curves for traction for each gear. ..... 66

Fig. 4.12. Automatic gear-shifting curves and boundary curves for regenerative braking in each gear. ..... 67

Fig. 4.13. Automatic gear-shifting curves for the eAxle's transmission torque-speed map. ..... 68

Fig. 4.14. Vehicle speed, gear selection without hysteresis and gear selection with hysteresis vs. time. ..... 69

Fig. 4.15. Gear selection debounce filter input and output. ..... 70

Fig. 4.16. HS torques, HS speeds and gear selection vs. time (hh:mm:ss) for a traction and regenerative braking cycle. ..... 71

Fig. 4.17. Transmission torque, transmission speed and gear selection vs. time (hh:mm:ss) for a traction and regenerative braking cycle. ..... 72

Fig. 4.18. HS torques, HS speeds and gear selection vs. time (hh:mm:ss) for a peak acceleration cycle. ..... 73

Fig. 4.19. Transmission torque, transmission speed and gear selection vs. time (hh:mm:ss) for a peak acceleration cycle. ..... 73

Fig. 5.1. A CAD rendering of an 8x8 series-hybrid driveline. ..... 76

Fig. 5.2. High-level vehicle control architecture for an 8x8 vehicle. ..... 77

Fig. 5.3. Front axle back-lock angle. ..... 79

Fig. 5.4. A 6x6 vehicle with front twin-axle Ackermann steering completing a turn. ..... 80

Fig. 5.5. Notable turning radii vs. front axle back-lock for a 6x6 vehicle with FTAS. ..... 81

Fig. 5.6. Normalized wheel speeds vs. turning radius for a 6x6 vehicle with FTAS. ..... 82

Fig. 5.7. Normalized axle speeds vs. turning radius for a 6x6 vehicle with FTAS. ..... 82

Fig. 5.8. eAxle torques and chassis pitch of a 4x4 vehicle completing a grade climb. ..... 84

Fig. 5.9. Staggered gear shifts for an 8x8 vehicle. ..... 85

Fig. 5.10. Staggered gear selection on an 8x8 vehicle with 500 ms between shifts for an 8x8 vehicle. ..... 86

Fig. 5.11. Vehicle acceleration simulation without staggered gear-shifting for an 8x8 vehicle. ..... 87

Fig. 5.12. Vehicle accleration simulation with staggered gear shifting for an 8x8 vehicle. ..... 88

Fig. 5.13. DCU development and validation framework. ..... 89

Fig. 5.14. DCU development and validation Simulink model. ..... 90

Fig. 5.15: DCU acceleration test for an 8x8 vehicle. ..... 91

Fig. 5.16. DCU hardware-in-the-loop test setup. ..... 93

## LIST OF TABLES

Table 1-1. Nominal eAxle performance ratings. 7

Table 2-1: Nominal vehicle parameters and acceleration requirement. 12

Table 2-2: Grade, peak speed and continuous speed specifications. 12

Table 2-3. Nominal eAxle performance ratings. 29

## LIST OF ABBREVIATIONS

| | |
|---|---|
| AC | Alternating Current |
| ASIL | Automotive Safety Integrity Level |
| AWD | All-Wheel-Drive |
| AWS | All Wheel Steering |
| BMS | Battery Management System |
| CAD | Computer Aided Design |
| CAN | Controller Area Network |
| CBS | Crab Steering |
| CoG | Centre of Gravity |
| CTIS | Central Tyre Inflation System |
| DC | Direct Current |
| DCU | Driveline Control Unit |
| DTC | Diagnostic Trouble Code |
| EACU | eAxle Control Unit |
| E-STOP | Emergency-Stop |
| eAxle | Electrified Axle |
| eDifferential | Electrified Differential |
| EV | Electric Vehicle |
| FBD | Free-Body Diagram |
| FSAS | Front Single Axle Steering |
| FTAS | Front Twin Axle Steering |
| GVW | Gross Vehicle Weight |
| HEV | Hybrid Electric Vehicle |
| HS | Half-Shaft |
| HV | High Voltage |

| | |
|---|---|
| ICE | Internal Combustion Engine |
| IGBT | Insulated-Gate Bipolar Transistor |
| IMU | Inertial Measurement Unit |
| IPM | Interior Permanent Magnet |
| LV | Low Voltage |
| MCU | Motor Control Unit |
| PTO | Power Take-Off |
| PTS | Pivot Steering |
| SAE | Society of Automotive Engineers |
| V2L | Vehicle to Load |
| VCU | Vehicle Control Unit |

## LIST OF SCIENTIFIC SYMBOLS

| | |
|---|---|
| $F_a$ | The net acceleration force acting parallel to the slope. |
| $F_{N(net)}$ | The net force acting on the vehicle perpendicular to the slope. |
| $F_{P(net)}$ | The net force acting on the vehicle parallel to the slope. |
| $l_{s1}$ | The length of the suspension spring on axle 1. |
| $l_{s2}$ | The length of the suspension spring on axle 2. |
| $l_{s3}$ | The length of the suspension spring on axle 3. |
| $M_{(net)}$ | The net moment acting on the vehicle. |
| $N_1$ | The reaction force acting perpendicular to the slope at axle 1. |
| $N_2$ | The reaction force acting perpendicular to the slope at axle 2. |
| $N_3$ | The reaction force acting perpendicular to the slope at axle 3. |
| $W_{1-2}$ | The wheelbase from axle 1 to axle 2. |
| $W_{2-3}$ | The wheelbase from axle 2 to axle 3. |

# 1 INTRODUCTION

## 1.1 OVERVIEW

Electrification and, more specifically hybridization offer several universal advantages across vehicle sectors including energy recuperation through regenerative braking, elimination of internal combustion engine (ICE) idling losses, efficient and optimized energy management, increased low-speed torque, reduced acoustic noise and improved emissions [1], [2]. Where the battery pack is sufficiently sized, the vehicle can operate in electric vehicle (EV) mode with zero-tailpipe emissions. Other advantages of electrification include a reduction in the number of gear ratios required, improved acceleration due to the electric traction machine's ability to output maximum torque at zero and low speeds, vehicle-to-load (V2L) applications where electrical appliances can be powered from the electrified vehicle's battery pack or generator, and the potential to electrify auxiliary systems on the vehicle.

Distributed propulsion is a term used to describe multiple-motor powertrains. The benefits of distributed propulsion include independent torque vectoring, which can be used to minimise overall driveline power loss, and increased redundancy due to the presence of multiple propulsion sources. This is particularly useful when driving on rough off-road surfaces where the limiting slip of each wheel may vary significantly, and on steep gradient climbs, or during sharp accelerations, where torque can be distributed to maintain traction at all wheel stations [3], [4]. When the vehicle is equipped with a multiple-speed transmission, distributed propulsion allows the staggering of gearshifts and minimizes torque disruptions, thus improving ride and handling performance and increasing passenger comfort.

## 1.2 THESIS OBJECTIVES

The objective of this thesis is to develop a modular electrified axle (eAxle) that maintains compatibility with an existing mechanical axle for use with hybrid-electric technologies. Several objectives must be met to achieve this. First, powertrain sizing techniques must be developed that allow suitable inverters, motors and gear ratios to be selected. Packaging is of critical concern for eAxles, as many extra components must now be placed at axle level. These include motors, clutches, transmissions, oil pumps and heat exchangers. The second goal of this work is to develop an architecture to optimally position the eAxle components while maintaining compatibility with the mechanical axle's space claim. Optimization of the powertrain is the third goal of this project. Developing models for optimal gear selection to maximise the axle's efficiency is another project aim. Raw efficiency-optimized gear selection maps must be post-processed to make them practical for use on vehicles. Electrified drivelines require a substantially different control architecture to their mechanical counterparts. This is particularly true for drivelines with distributed propulsion, a term used to describe powertrains with multiple independent torque sources. Overcoming these control challenges is the fourth goal of this work [4].

## 1.3 THESIS STRUCTURE

This first chapter is intended as a broad introduction to the eAxle and driveline control spaces, providing some background and explaining the motivations for the research undertaken in the remainder of the thesis. There are four technical chapters and a conclusions chapter.

In Chapter 2, a novel gradient and acceleration weight transfer calculation is used to size the eAxle powertrain based on axle loading and the wheel-slip-limited available torque. This calculation is subsequently validated through a comprehensive dynamometer test with prototype eAxle hardware. The powertrain sizing methodology exercise is demonstrated by determining the eAxle's tractive effort requirements using a 27-tonne 6x6 vehicle as a case study. The novel weight transfer-based approach is used to identify the worst-case (most heavily loaded) axle operating conditions which in turn are used for sizing the powertrain. The eAxle requires a three-speed transmission to meet its key operating point requirements. The performance of the hybrid 6x6 vehicle is simulated at constant speed operating points and during acceleration runs. Dynamometer testing is used to validate the powertrain's performance.

Chapter 3 explores novel packaging concepts for eAxle powertrains. An over-the-shoulder concept, where the eAxle's differential pinion-gear is located on the opposite side of the differential to the motor and transmission is presented. Using an over-the-shoulder packaging concept enables a more symmetric distribution of the power train components about the eAxle's driveshafts. This novel packaging concept facilitates the installation of auxiliary kits and drives on the pinion-gear side of the differential. The auxiliary drives include inboard parking brakes and ground-driven steering pumps, both of which are essential to meet vehicle safety and redundancy requirements. Power Take-Off (PTO) shafts can also

be used with this system. The eAxle can be orientated with the motor facing the front or rear of the vehicle. This allows for greater flexibility when considering driveline layouts and meeting approach and departure angle requirements.

Efficiency-optimized gear selection curves are developed for the eAxle in Chapter 4. The eAxle's inverter and motor power loss data is analysed and post-processed to derive combined power loss and efficiency maps for the combined inverter and motor system. These maps are combined with power loss and efficiency data for the eAxle's drivetrain to produce efficiency maps for each of the eAxle's gears. The efficiency maps for each gear are mapped to a common set of lookup vectors before the most efficient gear for each operating point is selected. While this gear selection map is optimized from an efficiency perspective, there are practical considerations that prevent it from being directly applied to vehicle applications. Efficiency-derived upshift and downshift curves are developed for each gear transition to overcome these issues. The gear shift curves' performance is compared with the efficiency-optimized map in simulation. Dynamometer testing is used to validate the gear selection strategies.

Chapter 5 focuses on the development of driveline control algorithms for the coordination of multiple modular eAxles in a driveline. The algorithms are implemented on a Driveline Control Unit (DCU), a supervisory controller that acts as an interface between the Vehicle Control Unit (VCU) and the eAxle Control Units (EACUs). Some of the DCU's key features include measuring wheel speeds, wheel-slip calculation, available torque calculation, torque vectoring, wheel-slip limitation, driveline efficiency optimization, gear selection and staggered gear-shifting are explored throughout the chapter.

The thesis is summarized, and conclusions are drawn in Chapter 6. References are provided in Chapter 0.

## 1.4 GENERAL BACKGROUND

An eAxle is an integrated unit used in electric and hybrid vehicles that combines an electric motor, transmission, and power electronics into a single compact module. The primary function of the eAxle is to deliver power from the electric motor to the vehicle's wheels, thus propelling the vehicle. Unlike traditional ICE powertrains, which require a complex system including additional gears, a transfer case and through-drive differentials [5], the eAxle simplifies the drivetrain by integrating these components, and reducing the number of required gear ratios [3], [4]. This integration results in a more efficient, compact, and lighter system that is crucial for optimizing the performance and range of Electric Vehicles (EVs) and Hybrid Electric Vehicles (HEVs).

At the core of the eAxle is an electric motor, which converts electrical energy stored in the vehicle's battery into mechanical energy to drive the wheels. The electric motor's efficiency, high torque at zero and low speeds, and instant torque delivery make it ideal for vehicle propulsion [1]. The motor is typically connected to a transmission system that includes reduction gears to convert the high rotational

speed of the motor to a suitable speed for the wheels [3], [4]. This gearing ensures that the motor operates within its optimal efficiency range while providing the necessary torque at the wheels for various driving conditions, from urban driving to highway cruising and traversing off-road terrain [6], [7].

Power electronics play a crucial role in managing the flow of electricity in the powertrain [1]. These components, including inverters and controllers, convert direct current (DC) from the battery into alternating current (AC) required by the motor. They also handle the reverse process during regenerative braking, where the motor acts as a generator to convert kinetic energy back into electrical energy, recharging the battery. This regenerative braking capability enhances the vehicle's overall efficiency and extends its driving range by recovering energy that would otherwise be lost as heat during braking.

Another critical component of the eAxle is the differential, which allows the wheels to rotate at different speeds, especially important when the vehicle is turning. The differential ensures smooth and stable handling by compensating for the differences in wheel speed, thus enhancing the vehicle's stability and drivability. Some advanced eAxle drivelines incorporate torque vectoring, where the power sent to each wheel can be independently controlled, providing improved handling and traction control, especially in performance and All-Wheel-Drive (AWD) vehicles.

One of the main features of the eAxle is its compact and lightweight design, which integrates multiple functions into a single unit, saving space and reducing the vehicle's overall weight. This compactness allows for more flexible vehicle design and easier integration into different types of electric and hybrid vehicles. Additionally, the eAxle’s modularity means it can be adapted for various vehicle configurations, including front-wheel drive, rear-wheel drive, and all-wheel drive setups. This adaptability, combined with the efficiency and performance benefits, makes the eAxle a key technology in the advancement of electric mobility. In addition, the use of eAxles in an all-wheel-drive vehicle eliminates the need for a transfer case and the need for a mechanical connection between the axles, from the axles to a transfer case and from a transfer case to the powerpack. This reduces complexity of the vehicle design, increases the flexibility of the vehicle driveline layout, increases available space within the vehicle and lowers the centre of gravity, improving stability.

Several companies have developed their own eAxles for vehicle applications in the heavy-duty sector including Volvo [8], Meritor [9], ZF [10], Dana [11], Allison [12] and Kessler [13]. Others have developed electrical machines specifically for the heavy-duty market, amongst them ABB [14], Danfoss [15] and Borg Warner [16].

eAxle designs can be found in the literature, including eAxles to maximise fuel economy [17], the development of an all-terrain 8x8 vehicle with individual wheel drive [18], and the lightweight design and optimization of a three-speed electric drive axle [19]. Work has also been done on optimal torque distribution control of multi-axle electric vehicles [20] and integrated torque vectoring control for three-

axle electric buses [21]. Weight transfer while braking to determine maximum deceleration rates for two-axle vehicles was explored in [2] and [22].

While conventional ICE vehicles typically have 5 or 6 speed transmissions [1], passenger EVs typically feature single-speed transmissions, a feature enabled by the electric motor's ability to produce high torque at low speeds and provide useable torque across a wide speed range [1]. Heavy-duty vehicles are typically expected to reach maximum speeds close to those of passenger vehicles. However, their torque output is typically several times higher [4], [3]. Diesel equivalents to the electric powertrain discussed in this thesis typically feature a torque converter and 12 gears. It is usually not feasible to implement a heavy-duty electric powertrain with a single-speed transmission. Allison [12], Eaton [23], Cummins-Meritor [9] and ZF [10] have all developed multiple-speed transmissions for heavy-duty EVs.

The literature contains several publications focusing on gear-shift maps for conventional vehicles [24], [25], [26], [27], [28]. A comprehensive state-of-the-art review of multi-speed gearboxes for battery-electric vehicles was completed in [29]. The work in [30] looked at optimizing and coordinating gearshifts in a four-speed automated manual transmission with a dual-motor electric powertrain. In [31] the fuel economy of a single-speed EV powertrain was compared with that of a powertrain featuring an electric motor paired with a two-speed inverse automatic transmission. The work in [32] is focused on a loss-minimizing gear-selection algorithm for a commercial pick-up truck. There is a sparsity of publications relating specifically to efficiency-optimized gear-shifting and gear selection maps for heavy-duty eAxles.

Distributed propulsion electric vehicles have been around for many years in the passenger automotive space. Notable vehicles in today's market include the Tesla Cybertruck [33], Ford F-150 Lightning [34] and the Rivian R1T [35]. Distributed propulsion heavy-duty vehicles have more recently entered the market with examples including the Tesla Semi [36] and the Mercedes-Benz eActros 600 [37]. The literature contains several examples on powertrain control for vehicles with multiple electric motors. The authors in [38] focused on mitigating wheel-slip in multi-motor heavy-duty electric vehicles, and the researchers in [39] looked at controlling electric vehicles with multiple in-wheel motors.

Despite the advantages of eAxles, there continue to be challenges in incorporating eAxles into all vehicle types, particularly those that are intended for off-road or heavy-duty applications. The provision of the motor on the underside of the vehicle means that it may be exposed during usage, and this particularly becomes an issue in environments where vehicle clearance from the ground may vary. Therefore, there continues to exist a need for improved eAxles.

The advantages provided by electrification and particularly distributed propulsion come hand-in-hand with several challenges such as an increased control complexity along with a higher number of control loops on the vehicle, significantly more interfaces, communication channels, and all the safety considerations that accompany high voltage electrical products [40], [41]. These challenges pose a

barrier to entry into the electrification space for many legacy automakers and vehicle integrators who, despite their longstanding experience and established mechanical skillsets, are not equipped to tackle the new challenges posed by electrification. For this reason, it is in suppliers' best interests to offer solutions to these challenges and integration support in conjunction with new and innovative propulsion technologies.

## 1.5 eAxle Specifications

### 1.5.1 eAxle Hardware

The Timoney T9000e eAxle is designed for 4x4, 6x6 and 8x8 vehicle configurations but can also be used in drivelines where only some axles are powered, such as for 6x4 and 8x6 vehicles. The eAxle maintains compatibility with an existing 9-tonne independent suspension system and its associated reduction hubs. The eAxle is modular and can be used across a multitude of on-highway and off-highway vehicle sectors including agriculture, construction, fire trucks, forest machinery, mining and powered trailers. The eAxle is suitable for use in series-hybrid, battery-electric and hydrogen fuel cell vehicles. A demonstration model of the T9000e eAxle can be seen in Fig. 1.1 with an alternative view shown in Fig. 1.2 [5].

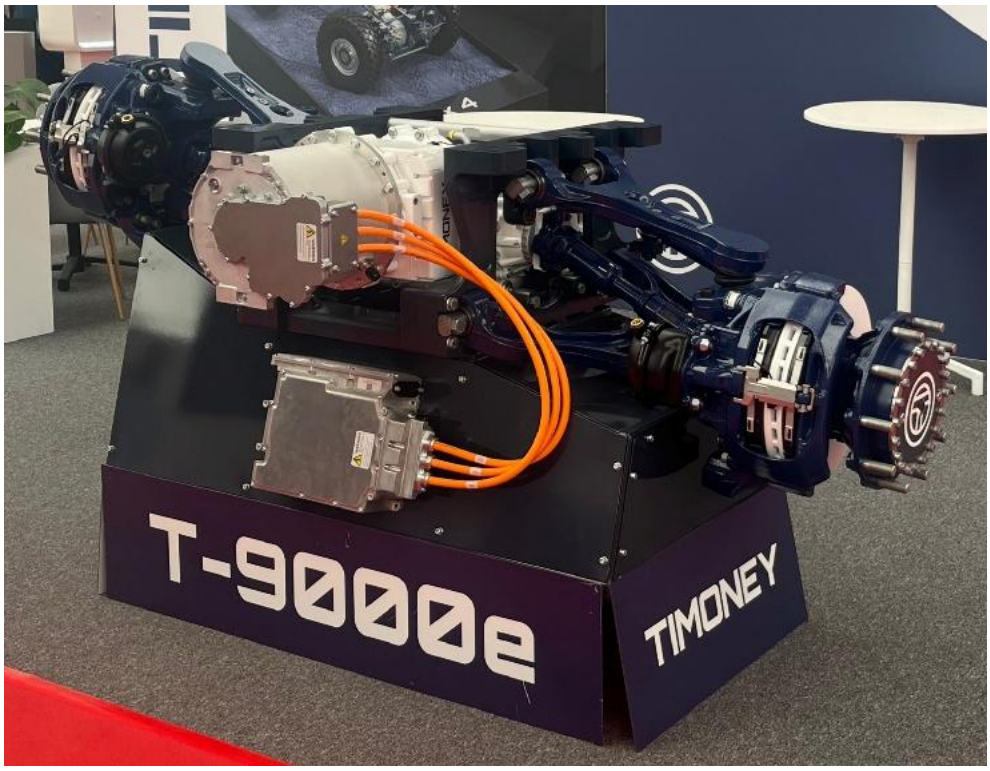



Fig. 1.1. A demonstration model of the T9000e eAxle.



Fig. 1.2. An alternative view of the T9000e eAxle.

The eAxle uses an insulated-gate bipolar transistor (IGBT) based inverter that is compatible with a DC link voltage range between 500 V to 800 V. The eAxle's motor is an interior permanent magnet (IPM) machine that has a 790 N m peak torque, 230 kW of peak power, and a 10,300 rpm maximum speed. The peak and continuous performance of the eAxle was developed in [3] (Chapter 2) and is summarized here in Table 1-1.

Table 1-1. Nominal eAxle performance ratings.

| **eAxle Parameter** | **Value** |
|---|---|
| Peak Torque | 54 kN m |
| Continuous Torque | 28 kN m |
| Peak Power | 208 kW |
| Continuous Power | 110 kW |

The eAxle includes an independent suspension system with 360 mm of wheel travel. The trackwidth is adjustable to meet vehicle integrator's requirements. The gear ratios in the hubs can be adjusted to accommodate different tyre sizes.

A high-level powertrain layout for the eAxle is shown in Fig. 1.3. The motor axis is orientated perpendicular to axle's axis of rotation and drives the input to a three-speed planetary transmission with

electrically actuated clutches that is force-lubricated via an integrated oil pump. The eAxle has two additional reduction gear stages, the differential's spiral bevel set and the planetary gearsets in the hubs. A patent has been filed for a novel packaging topology used on the T9000e [42], as will be discussed in Chapter 3).

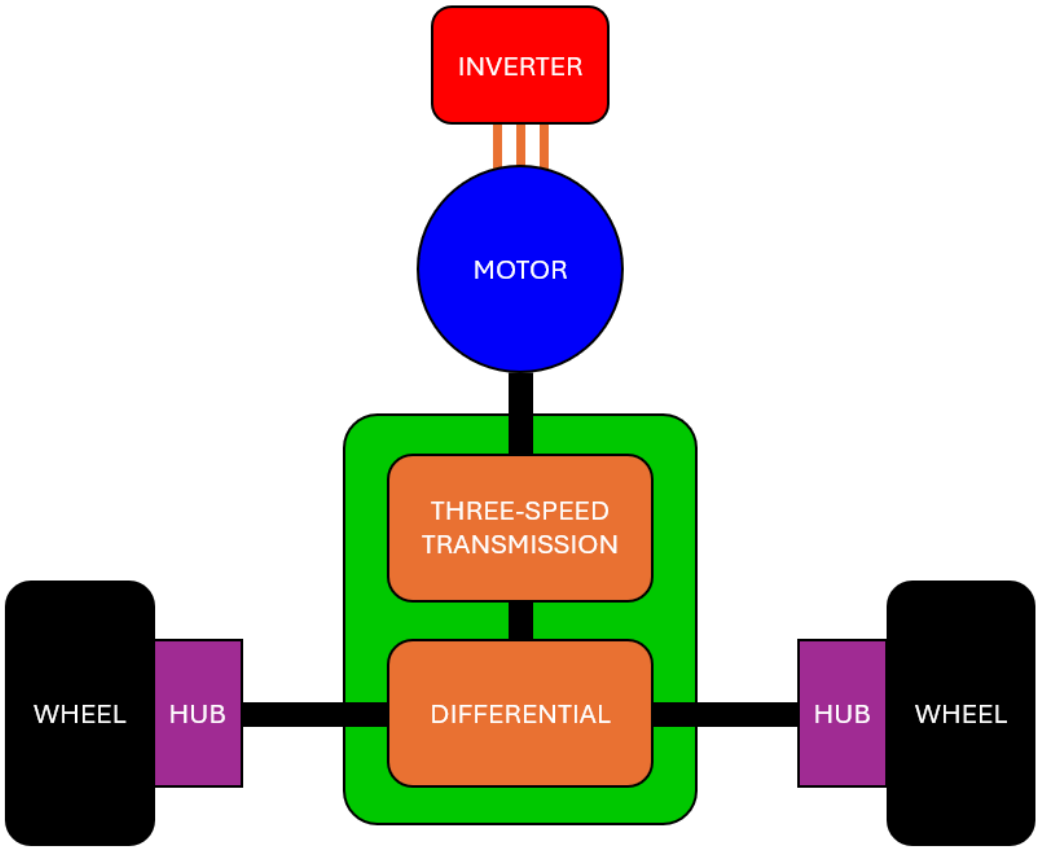



Fig. 1.3: A high-level eAxle powertrain layout.

While the term in Electrified Differential (eDifferential) can be used to describe a differential that is electronically controlled, *in this work, the term eDifferential refers to the portion of the eAxle including the motor, the three-speed transmission, and the mechanical differential*. The differential in this eAxle is pneumatically applied and spring released. A CAD rendering of the eDifferential is shown in Fig. 1.4 [5].

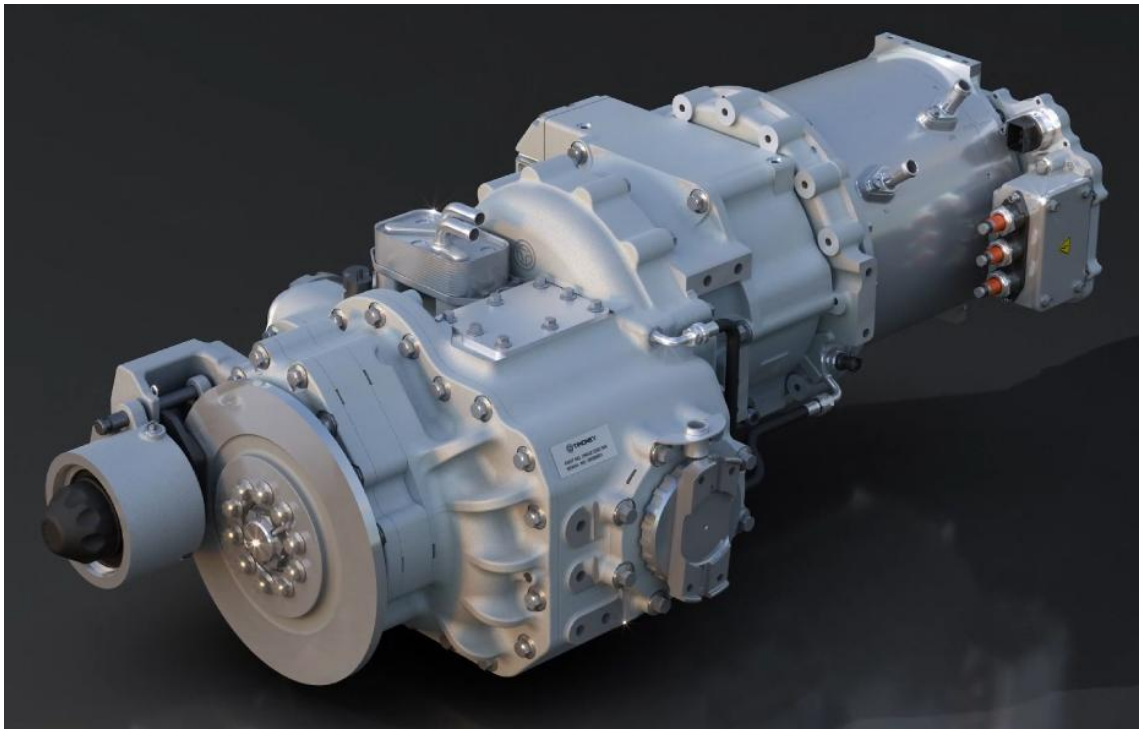


Fig. 1.4: A CAD rendering of the eDifferential.

In terms of cooling, the inverter, motor and Electrified Differential (eDifferential) require active cooling. Each component uses a 50 % deionized water, 50 % glycol coolant mix. The hubs do not require active cooling. The work by the authors in [3] (Chapter 2) explains the need for a three-speed transmission. First gear is constrained by the need to produce high torque at low speed. Third gear is constrained by the maximum speed requirements. An intermediate ratio (second gear) is required for medium torque, medium speed operating points that cannot be reached by first or third gears.

### 1.5.2 eAxle Control

The eAxle assembly includes an integrated eAxle Control Unit (EACU) that manages the control of the inverter, the traction machine, the clutch assembly, the integrated oil pump and the differential lock. The eAxle operates in torque-control mode and the EACU is controlled via CAN. The CAN control interface allows for both manual and automatic transmission modes. Each gear ratio and neutral can be requested along with automatic shifting options that use all three gears or second and third gear only. Using second and third gear only is advantageous for maximum accelerations on low grades as the number of gear changes is halved and the high reflected inertia seen on the motor shaft in first gear is avoided. These factors can outweigh the benefits of the higher torque produced by first gear. It should be noted that reflected inertia is proportional to the gear ratio squared [2]. For multi-axle vehicles the EACUs are controlled by a supervisory Driveline Control Unit (DCU). This allows for innovative

torque vectoring and staggered gear selection strategies. In such situations, the automatic gear selection maps are stored on the DCU, and the EACUs' manual transmission mode is used.

### 1.5.3 DRIVELINE INTEGRATION

The eAxle is designed for 4x4, 6x6 and 8x8 drivelines but can also be used in vehicles where only some axles are driven such as 4x2, 6x4 and 8x6 configurations. Fig. 1.5 shows a CAD rendering of 4x4, 6x6 and 8x8 eAxle drivelines. While the eAxle is compatible with multiple fuel sources, this thesis will focus on series-hybrid systems. Chapter 2 focuses on a 6x6 vehicle as the odd number of axles best demonstrates the impact of weight transfer. Chapters 3 and 4 focus on optimizations for a single eAxle. In chapter 5, 4x4, 6x6 and 8x8 drivelines are discussed at various stages. The vehicle configuration being considered is noted in the figure captions.

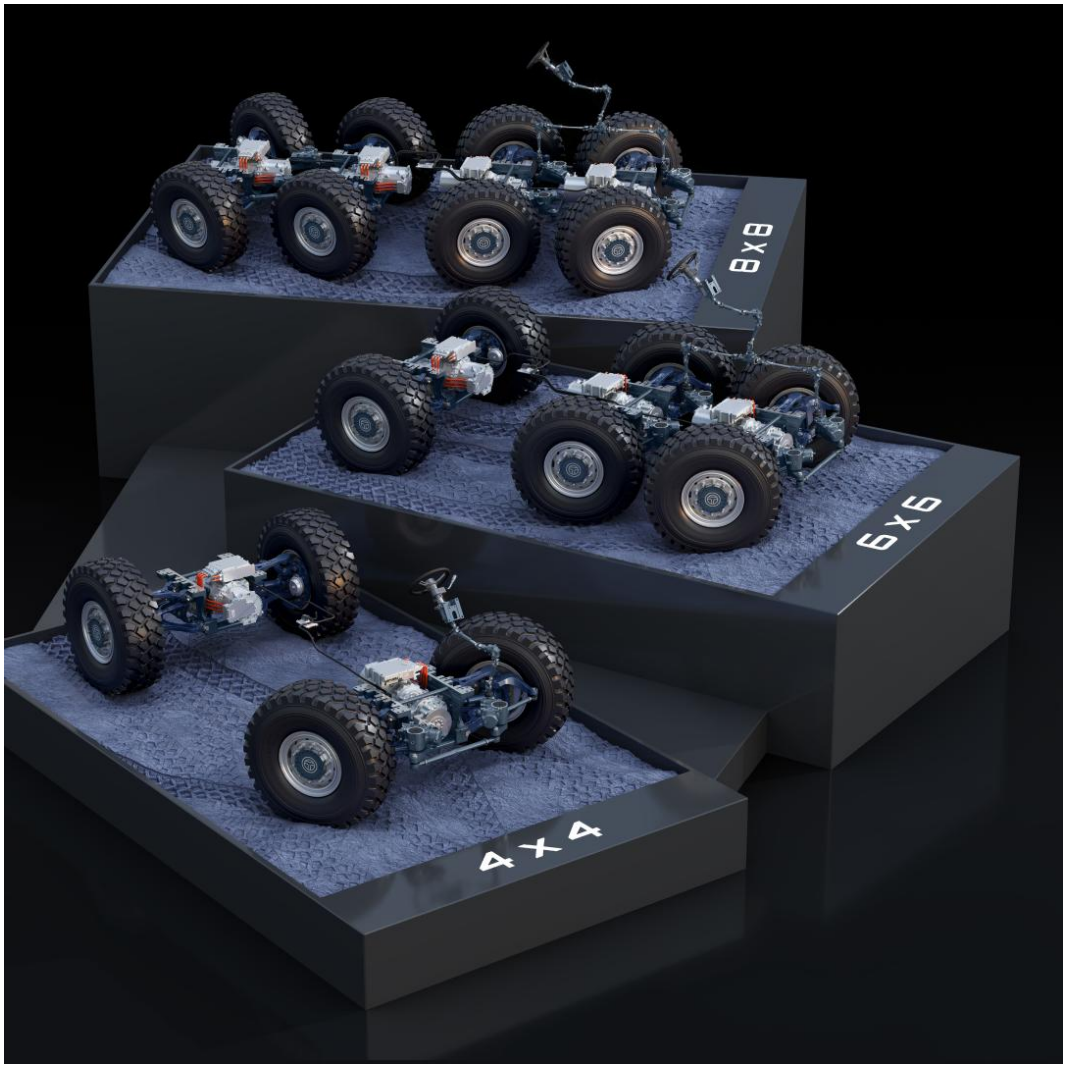



Fig. 1.5: A CAD rendering of 4x4, 6x6 and 8x8 drivelines.

# 2 DEVELOPMENT AND VALIDATION OF NOVEL DESIGN METHODOLOGIES FOR ELECTRIFIED AXLES

## 2.1 ABSTRACT

This chapter summarizes the design of a modular eAxle for all-terrain heavy-duty vehicle applications. A novel method based on axle loading and weight transfer for powertrain sizing is proposed and validated through dynamometer testing. This chapter focuses on a 27-tonne 6x6 vehicle as a case study to determine the eAxle's tractive effort requirements for one of the possible vehicle applications. A novel weight transfer-based approach is used for determining the worst-case (most heavily loaded) axle operating conditions which in turn are used for sizing the powertrain. A three-speed transmission is required to meet the vehicle performance requirements. The performance of the hybrid 6x6 vehicle is evaluated at steady-state operating points and during transient acceleration events. The powertrain sizing method is validated through a comprehensive dynamometer testing program.

The vehicle performance requirements for the 6x6 case study vehicle are presented in Section 2.2. The impact of weight transfer on axle loading is discussed in Section 2.3. The powertrain is then sized in Section 2.4. The transmission design and need for a three-speed transmission is discussed in Section 2.5. The 6x6 vehicle's performance is simulated in Section 2.6. A full-scale eAxle prototype is tested on a dynamometer across its torque-speed range in Section 2.7. The chapter is concluded in Section 2.8.

The work in this chapter has been published as follows:

- C. Healy and J. G. Hayes, "Design of a modular e-axle for all-terrain heavy-duty applications considering gradient weight transfer", *IEEE Transportation Electrification Conference and Expo (ITEC)*, 2023 [4].
- C. Healy and J. G. Hayes, "Design and test of a 200 kW modular eAxle for all-terrain heavy-duty vehicle applications", *IEEE Transactions on Transportation Electrification*, under review [3].

## 2.2 VEHICLE PERFORMANCE REQUIREMENTS

The eAxle is required to enable a 6x6 hybrid vehicle to match the performance of an existing 6x6 diesel vehicle. The design is to meet peak and continuous speed requirements on a selection of grades and to match the conventional vehicle's acceleration performance. The nominal vehicle parameters are presented in Table 2-1.

Table 2-1: Nominal vehicle parameters and acceleration requirement.

| Vehicle Parameter | Value |
|---|---|
| Gross Vehicle Weight (GVW) | 27,000 kg |
| Aerodynamic Drag Coefficient | 0.8 |
| On-Highway Rolling Resistance | 1.5 % |
| Tire Size | 16R20 |
| Acceleration Time (0 – 60 km/h) | 17 s |

Table 2-2 and Fig. 2.1 show the peak and continuous vehicle speed requirements vs. grade for an on-road application. The dashed curve shows the required peak vehicle speed vs. gradient as obtained from the conventional diesel vehicle's specification and the solid curve shows the continuous speed that must be reached on each gradient. Note that the hybrid vehicle must achieve a continuous cruising speed of 110 km/h on a 0 % grade. The additional power required for higher peak speeds can be supplied by running the engine at/near its maximum power while discharging the battery pack. The maximum speed decreases as the grade increases because more torque and power are required to overcome the climbing force. Note that the lines between the requirement points in Fig. 2.1 are for illustration only.

Table 2-2: Grade, peak speed and continuous speed specifications.

| Grade [%] | Required Peak Speed [km/h] | Available Continuous Speed [km/h] |
|---|---|---|
| 0 | 120 | 110 |
| 3 | 80 | 70 |
| 6 | 50 | 40 |
| 10 | 40 | 30 |
| 30 | 12 | 8 |
| 60 | 4 | N/A |

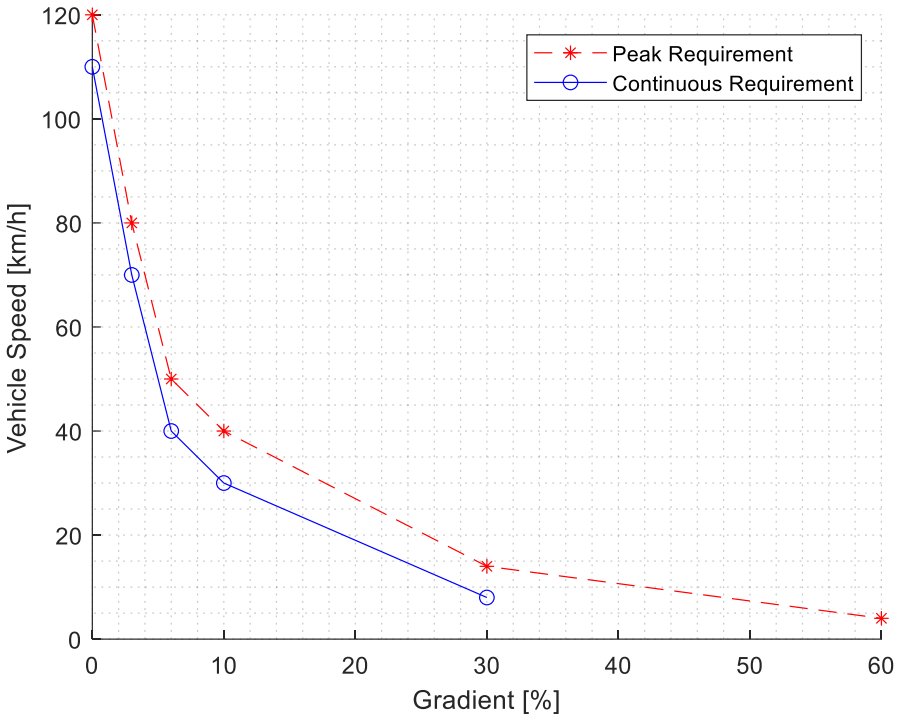



Fig. 2.1. Vehicle speed vs. gradient specification.

Fig. 2.2 shows the diesel vehicle's speed vs. time during a maximum acceleration run, where the points on the curve represent the requirements for the minimum speed the vehicle must achieve after a set time. Again, the dashed line has been added for illustration purposes only.

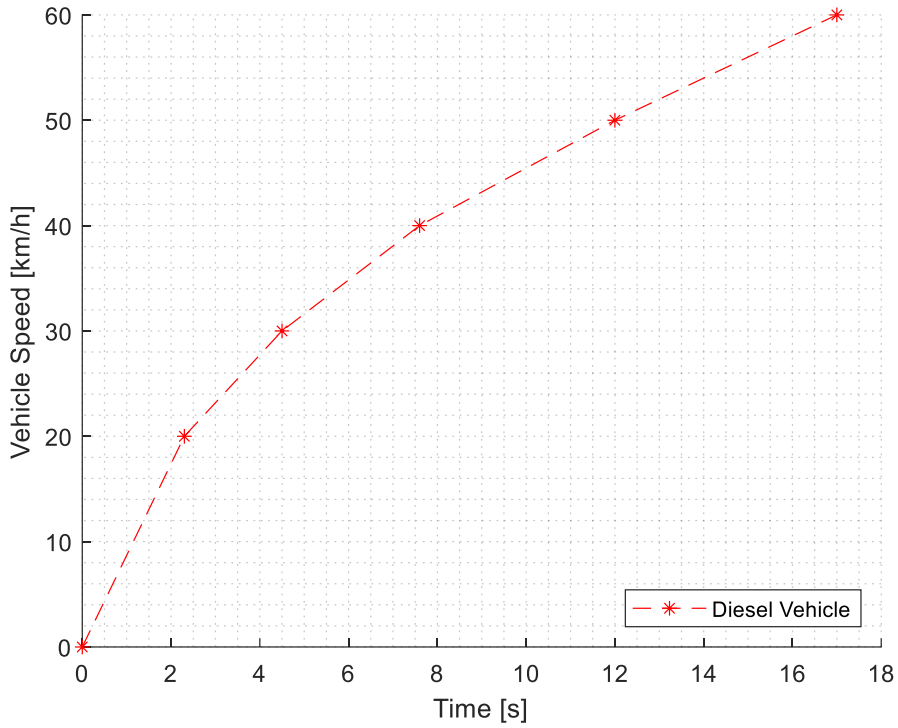



Fig. 2.2. Diesel vehicle speed vs. time during maximum acceleration.

Fig. 2.3 and Fig. 2.4 show the motive torque and motive power required to propel the vehicle to the peak and continuous steady-state speeds shown in Fig. 2.1. The total torque and power values were calculated by summing the contributions from aerodynamic, acceleration, rolling resistance and climbing loads. Looking at Fig. 2.3, the peak and continuous torques are similar for a given grade. This is mainly due to the road loads being dominated by rolling resistance and climbing loads as a result of the vehicle's heavy weight. Peak power is noticeably higher than continuous power in Fig. 2.4 for the same grade due to the higher peak speeds.

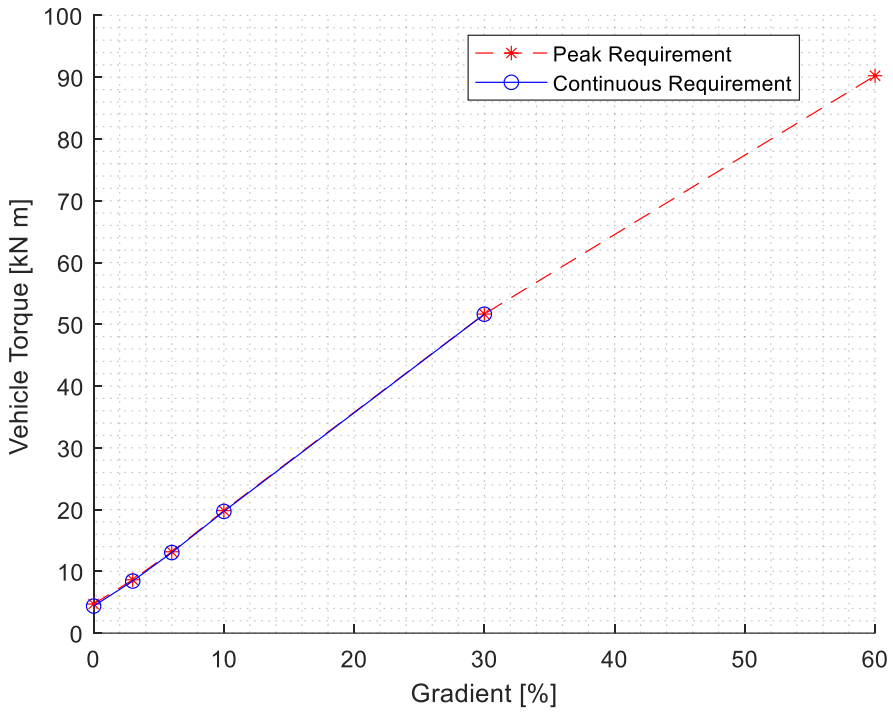



Fig. 2.3. Peak and continuous vehicle motive torque vs. gradient.

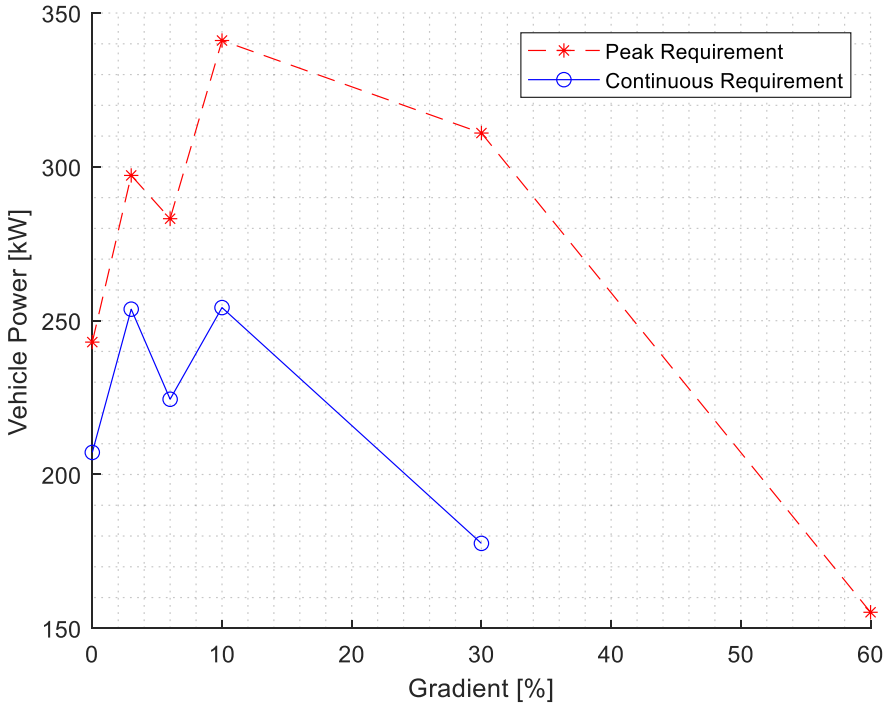



Fig. 2.4. Peak and continuous vehicle motive power vs. gradient.

## 2.3 WEIGHT TRANSFER

### 2.3.1 MODELLING WEIGHT TRANSFER

**Weight transfer** occurs when the distribution of load across a vehicle's axles varies. This is typically caused by changes in gradient or during acceleration and braking. The details of the weight transfer model used in this work are proprietary and cannot be presented in this thesis. However, this section aims to provide a high-level overview of the novelty associated with the model.

For any vehicle traversing a slope, the net forces and moments acting on the vehicle can be reduced to three parameters, $F_{N(net)}$ - the net force acting on the vehicle perpendicular to the slope, $F_{P(net)}$ - the net force acting on the vehicle parallel to the slope, $M_{(net)}$ - the net moment acting on the vehicle and $F_a$ - the net acceleration force acting parallel to the slope. For a 4x4 vehicle there are two axle normal reaction forces, $N_1$ and $N_2$ acting perpendicular to the slope. This presents a statics problem that can be solved by setting the sum of forces and moments acting on the vehicle equal to zero. This gives a unique solution for $N_1$ and $N_2$ and is described in multiple texts including [2], [22]. A free-body diagram (FBD) of the 6x6 vehicle discussed in this chapter is shown in Fig. 2.5. For the 6x6 configuration, there is an additional normal reaction force $N_3$ for the third axle. Note that $W_{1\text{-}2}$ and $W_{2\text{-}3}$ represent the wheelbases from axle 1 to axle 2 and axle 2 to axle 3, respectively.

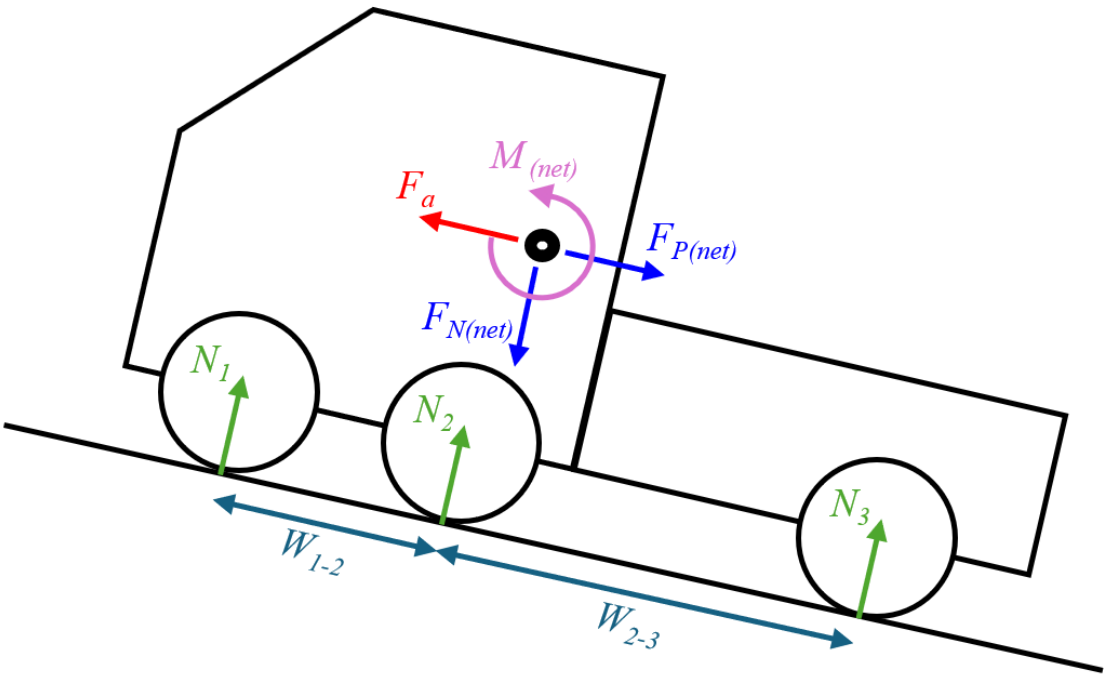



Fig. 2.5: A free-body diagram of a 6x6 vehicle traversing a slope.

The addition of the third axle's normal reaction force in Fig. 2.5 results in the FBD becoming statically indeterminate. This means that when the sum of the forces and moments acting on the vehicle are set equal to zero there is an infinite number of combinations of $N_1$, $N_2$ and $N_3$ that can satisfy the equations. An additional constraint must be added to the model to arrive at a unique solution.

This model uses a novel similar-triangles-based approach which results in a constant weight transfer gradient along the chassis. This concept is illustrated in Fig. 2.6 where $l_{s1}$, $l_{s2}$ and $l_{s3}$ are the lengths of the suspension springs on axles 1, 2 and 3, respectively. The basis of the model is that all three upper spring mounting points are coincident on the same line on the vehicle's hull and all three lower spring mounting points are coincident on the same line on each axle's lower wishbones. If linear-elastic springs are assumed, then the normal reaction force at each axle will be proportional to the compression of its spring. For any non-zero angle between the line intersecting the upper spring mounting pints and the line intersection the lower spring mounting points, the relationship between each of axle's spring compression and weight distribution can be solved using similar triangles. If the two above-mentioned lines are parallel, then all springs are the same length and the normal reaction forces are equal at all three axles.

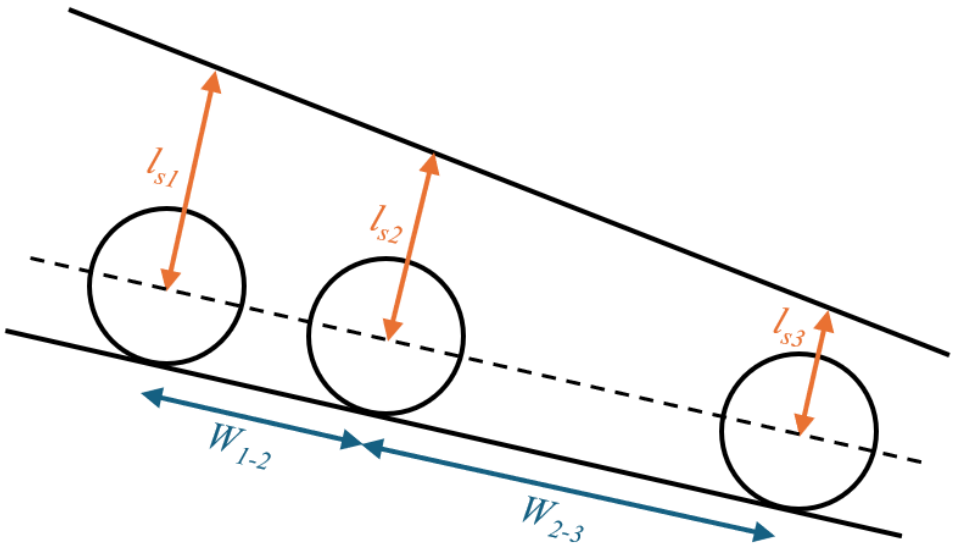



Fig. 2.6: Constraining the normal reaction forces using similar triangles.

Note that the same method as one applied to the 6x6 vehicle above can also be used to derive a unique solution for the weight distribution of an 8x8 vehicle.

### 2.3.2 CASE-STUDY VEHICLE WEIGHT TRANSFER

Fig. 2.7 shows how the loading on each axle varies with gradient for the 6x6 vehicle, where axle 1 is the front axle, axle 2 is the middle axle and axle 3 is the rear axle. Note that all weight transfer plots in this chapter are calculated not measured. For forward grade climbs, axle 3 has the highest loading. For reverse grade climbs, axle 1 has the highest load but the magnitude of the load acting on axle 3 when moving forward is greater than the load on axle 1 when reversing. This is due to the vehicle's wheelbases and the position of each axle relative to the vehicle's centre of mass. For this reason, axle 3 is used as the worst-case axle for sizing the tractive requirements of the electrified powertrain. The reason the powertrain should be sized based on axle 3 is that as the weight is transferred to the rear of the vehicle while climbing, the wheels on the front axles (especially axle 1) will lose traction and slip if too much torque is applied to them. For this reason, a higher percentage of torque must be distributed to axle 3 during gradient climbs. This is known as **torque vectoring**, where the torque directed to each axle is varied. In this application, the torque vectoring algorithm is implemented by a supervisory Driveline Control Unit (DCU) that communicates with each eAxle.

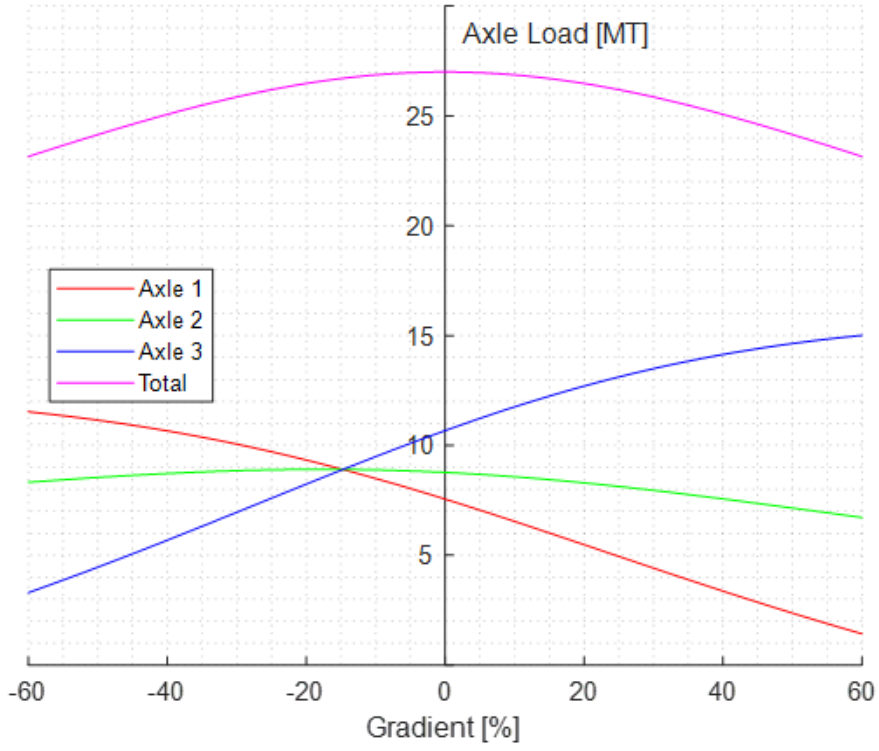



Fig. 2.7. Axle loading (MT = metric tonnes) vs. gradient for a 6x6 vehicle travelling at constant speed.

Fig. 2.8 shows how the vehicle's weight distribution varies for the same vehicle at different acceleration rates on a 0 % grade. When accelerating, weight is transferred from the front of the vehicle to the rear. The opposite is true for deceleration where extra weight is carried by the front axles.

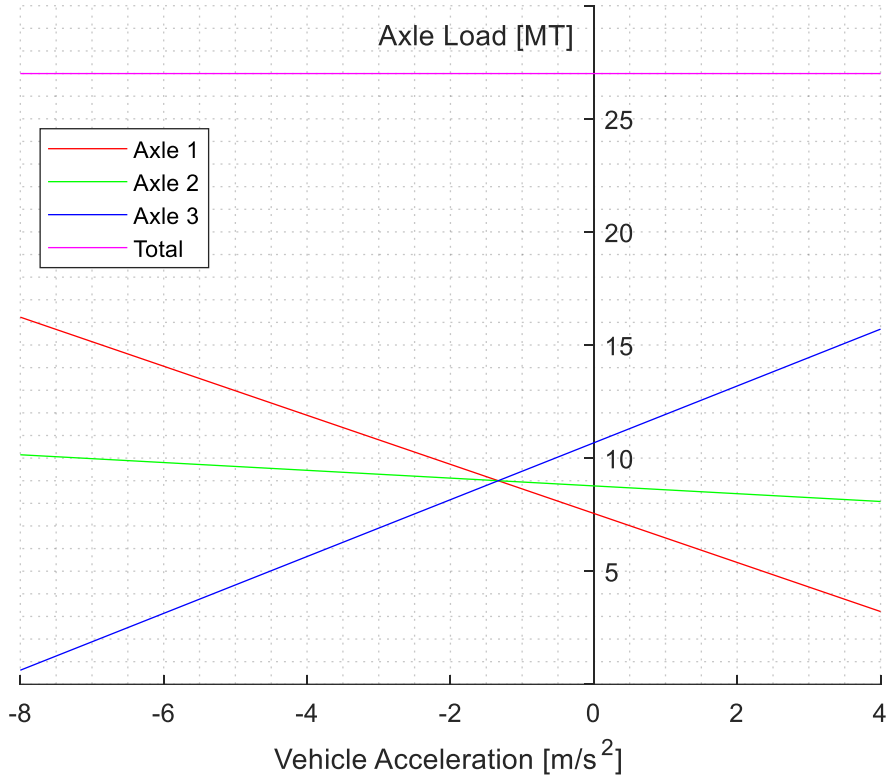



Fig. 2.8. Axle loading (MT = metric tonnes) vs. acceleration for a 6x6 vehicle on a 0 % grade.

## 2.4 POWERTRAIN SIZING

The next design phase is to determine the worst-case per-axle torque-speed requirements. Reverting to Fig. 2.7, the loading is highest on axle 3, especially on steep forward gradients. The maximum motive torque that can be applied to a wheel before it starts slipping is basically proportional to the normal force acting on the wheel perpendicular to the ground. This relationship is governed by the coefficient of friction between the tire and the road and the tire radius. The available torque is the maximum torque that can be produced without inducing wheel-slip or exceeding the powertrain limits. Fig. 2.9 shows the available torque from each eAxle and the total from the vehicle plotted against gradient. Fig. 2.10 shows a similar plot, but in this case the available torque is plotted against the vehicle's acceleration.

Note that the horizontal sections of the axle available torque curves correspond to the axle being maximum torque limited rather than traction limited. This is most noted on the axle 3 curve in Fig. 2.9 and the axle 1 and 3 curves in Fig. 2.10 As the powertrain's maximum torque capability is not known

at this stage of the analysis, the torque limit is set by the driveshafts at this stage. The maximum axle torque on available torque plots shown in Fig. 2.9 and Fig. 2.10 will be updated in Fig. 2.21 and Fig. 2.22 after the powertrain performance has been determined.

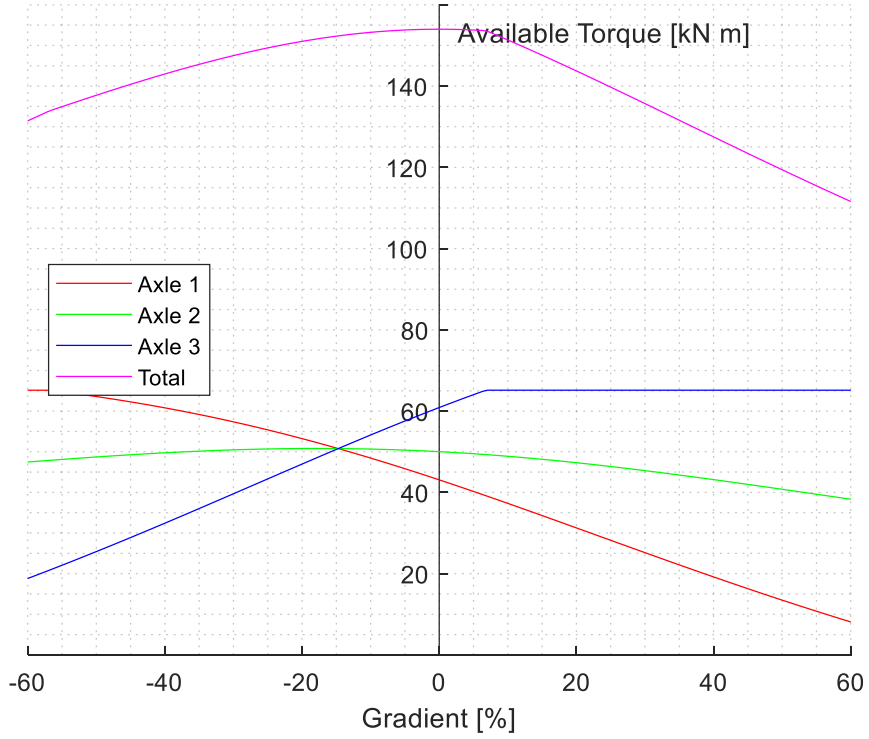



Fig. 2.9. Available torque vs. gradient.

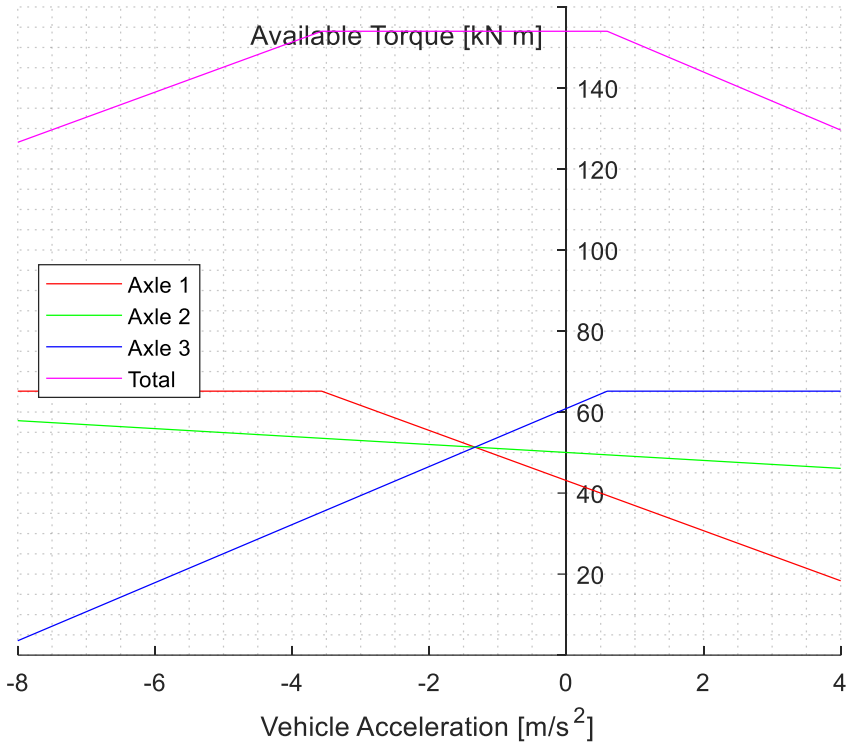



Fig. 2.10. Available torque vs. acceleration.

While acceleration weight transfer is also important and warrants consideration, it should be noted that for most of an acceleration run the vehicle's eAxles will be limited by the eAxle's maximum motor torque rather than the wheel-slip. However, at steady-state speeds on steep grades where accelerations are low, but gradient weight transfer is significant, the eAxle is expected to operate near its maximum torque capability. For this reason, gradient weight transfer is most significant when sizing the low-end torque capability of the powertrain.

Maximum motive torque without inducing wheel-slip can be achieved by vectoring the torque to each axle in proportion to the weight that they are bearing. Fig. 2.11 shows this torque vectoring strategy. Gradient has the greatest impact on axle torque vectoring, and so it is plotted on the x-axis. While this control strategy minimizes the chances of wheels slipping, it places excessive requirements on axle 3. This excessive torque requirement may cause the powertrain to be unnecessarily overrated.

In a conventional driveline all differentials are locked during steep grade climbs. This causes the torque to be distributed to each axle according to its loading. For a vehicle with eAxles, this must be implemented via electronic control. A novel torque vectoring strategy is proposed in [4] to equally distribute the torque between the axles where possible and to only vector extra torque to the rear axles when necessary. This strategy is shown in Fig. 2.12. The revized algorithm reduced the 30 % grade axle 3 torque from 27.0 kN m per Fig. 2.11 to 17.2 kN m per Fig. 2.12 and similarly, the 60 % grade axle 3 torque from 58.5 kN m in Fig. 2.11 to 46.0 kN m in Fig. 2.12 The new required torque and power plots

are shown in Fig. 2.13 and Fig. 2.14. It should be noted that the independent suspension ensures that all axles are loaded appropriately and maintain contact with the ground.

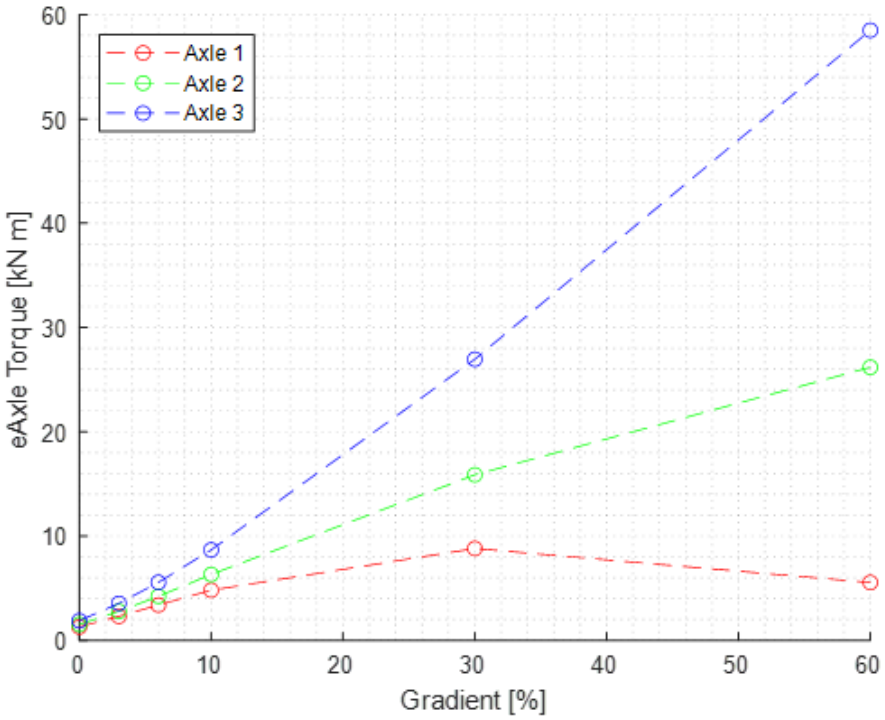



Fig. 2.11. Axle torque to meet vehicle requirements vectored in proportion to weight distribution vs. gradient.

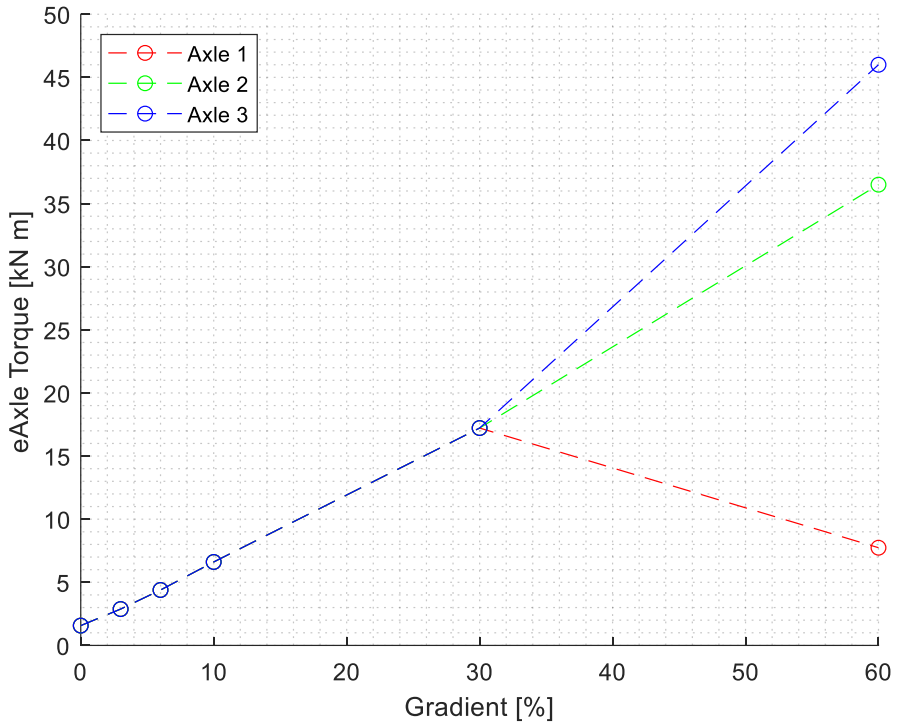



Fig. 2.12. Peak axle torque to meet vehicle requirements vectored equally where possible vs. gradient.

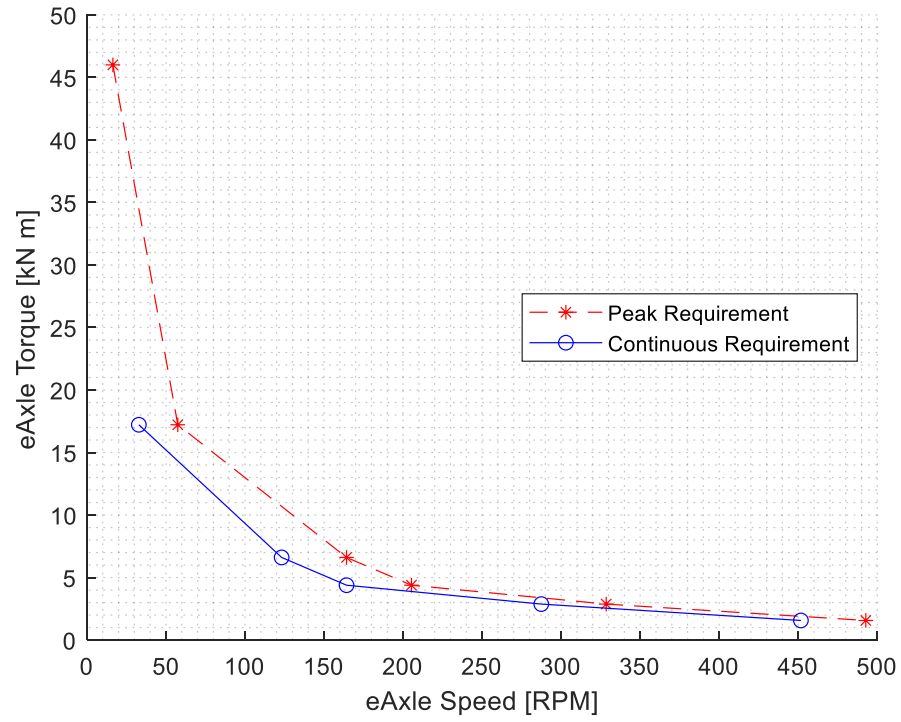



Fig. 2.13. Case study vehicle axle 3 torque specification vs. axle angular speed.

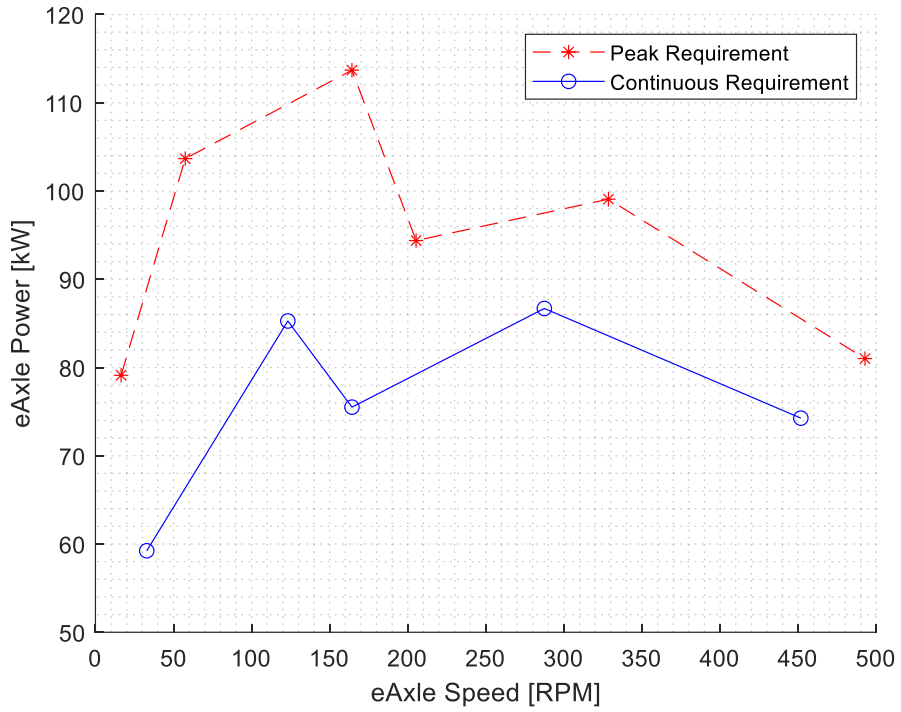



Fig. 2.14. Case study vehicle axle 3 power specification vs. axle angular speed.

The above analysis to determine the eAxle requirements for the 27 tonne 6x6 vehicle is completed for several varying vehicle platforms to determine the overall design specification for the eAxle. The vehicle platforms include 4x4, 6x6, 8x8, 6x4 and 8x6 vehicles with weights ranging from 16 tonnes to 36 tonnes. The vehicles operate on a multitude of terrains including paved roads, unpaved roads, cross-country trails and sand. Some vehicles were required to tow trailers with weights up to 15 tonnes. The resulting eAxle torque and power requirements are shown in Fig. 2.15 and Fig. 2.16, respectively. The peak torque requirement is 46 kN m and the peak output power requirement is 150 kW.

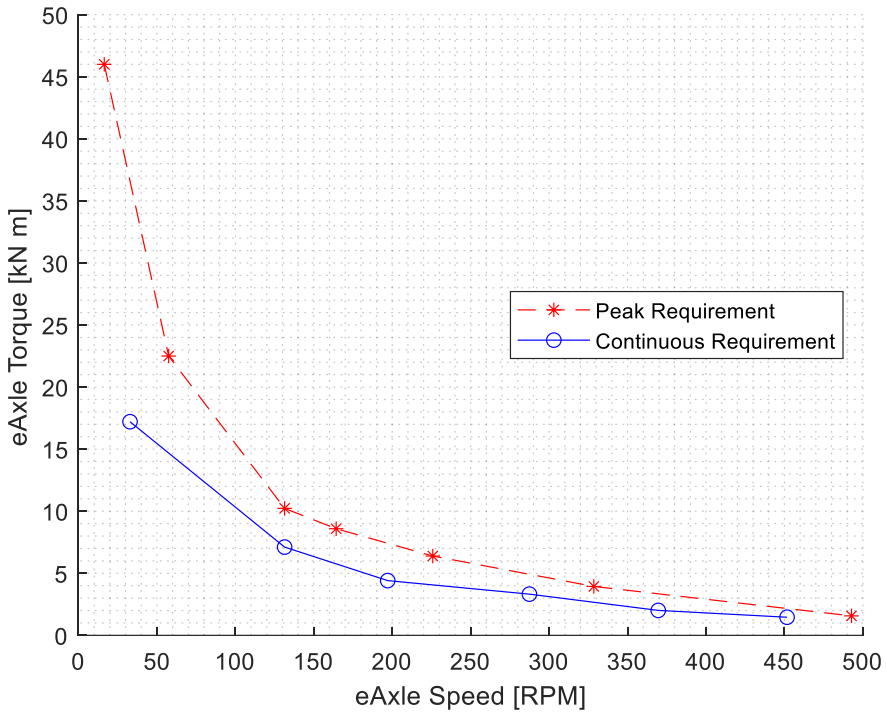



Fig. 2.15. eAxle torque specification vs axle angular speed.

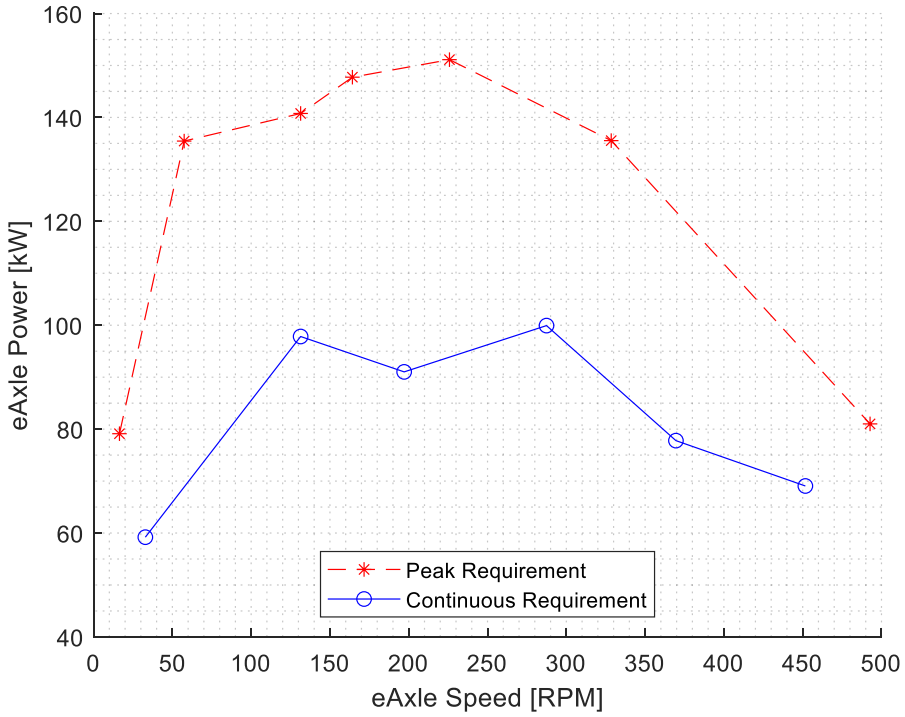



Fig. 2.16. eAxle power specification vs. axle angular speed.

## 2.5 TRANSMISSION DESIGN

The design brief for the 6x6 required the eAxle to be connected to a nominal 650 V DC link, and the selected traction machine's torque and power curves were specified at a 65 °C coolant temperature. These are typical worst-case operating points. Increasing the DC link voltage (the eAxle is compatible with DC link voltages as high as 800 V) and lowering the coolant temperature would increase the eAxle's performance. It is imperative that worst-case conditions are used for powertrain sizing to ensure that the eAxle's traction machine is not undersized. The motor's tractive effort curves were then scaled using the driveline ratios and efficiencies to give the torque and power plots shown in Fig. 2.17 and Fig. 2.18 respectively, with vehicle speed on the *x*-axis. Note from Table 2-1 that the case study 6x6 vehicle uses 16R20 tires. The need for a three-speed transmission is discussed later in this section when the eAxle's performance is compared with its peak and continuous requirements in Fig. 2.19 and Fig. 2.20.

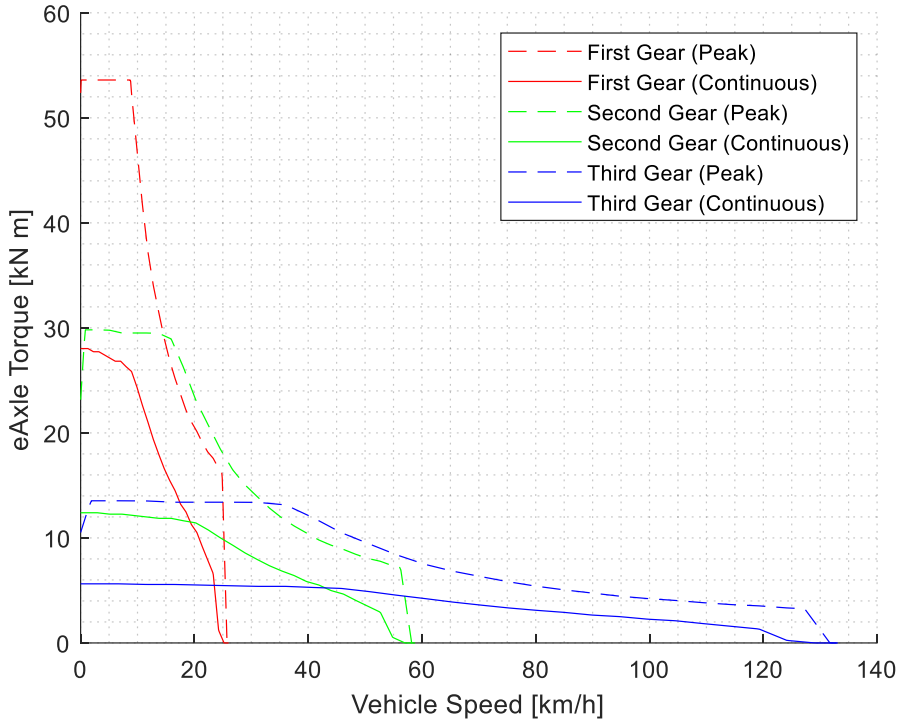



Fig. 2.17. eAxle torque curves at 650 $V_{DC}$ and a 65 °C coolant temperature.

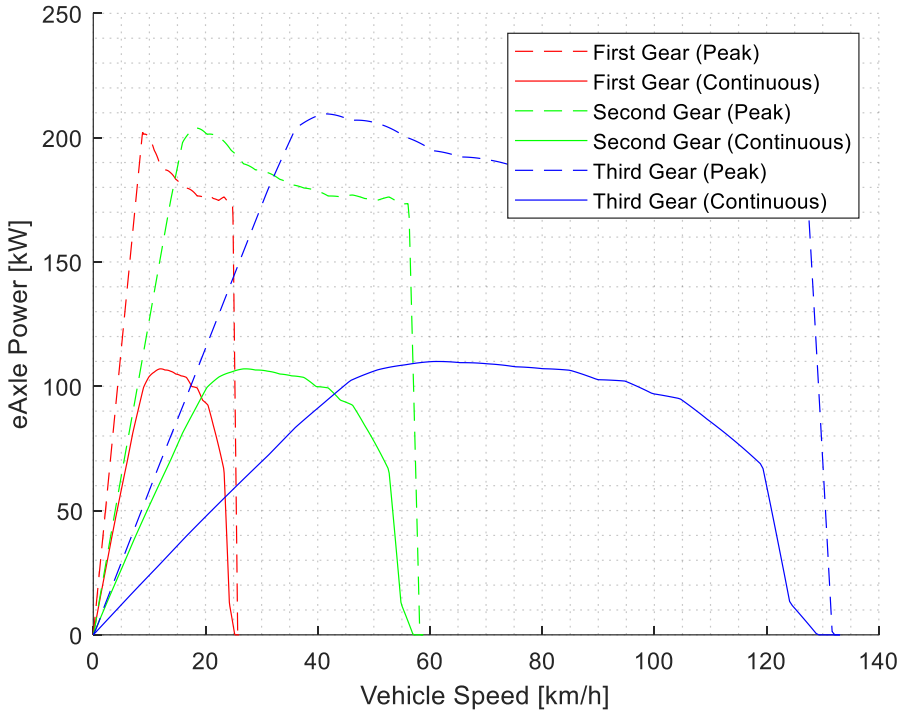



Fig. 2.18. eAxle power curves at 650 $V_{DC}$ and a 65 °C coolant temperature.

The resulting curves from the three-speed transmission were combined to give a single curve across the eAxle's speed range. The new curves were overlayed on the axle requirement plots from Fig. 2.15 and Fig. 2.16 to give the tractive effort plots shown in Fig. 2.19 and Fig. 2.20. All performance requirement points were met with this design. Note that it is important to maintain significant headroom from operating at the peak torque boundary as any variations in ambient temperature or the performance of the vehicle's cooling system can significantly impact the duration that the traction machine can operate at its peak torque boundary without overheating. Thus, the powertrain's maximum torque output has been increased from the 46 kN m requirement to 54 kN m and the peak power capability has been increased from the 150 kW requirement to 208 kW. It should be noted that the eAxle's torque limit is set by the crownwheel gear that drives the eAxle's differential. Otherwise, the traction system can reach the driveshafts' 65 kN m torque limit in first gear. Also note that the high peak power relative to the requirement is a consequence of needing to meet continuous power requirements at similar speeds. In other words, the high continuous power pushes up the peak power. The electric motor is an interior permanent magnet (IPM) machine that has a peak torque of 790 N m, a peak power of 230 kW, and a nominal maximum speed of 10,300 rpm.

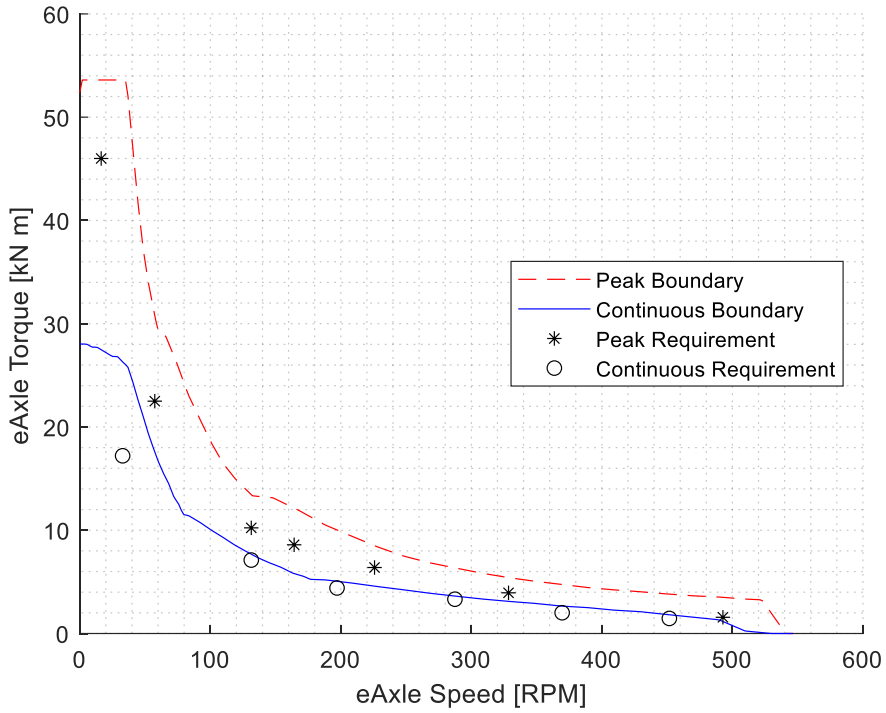



Fig. 2.19. Combined eAxle torque curve and axle requirements at 650 $V_{DC}$ and a 65 °C coolant temperature.

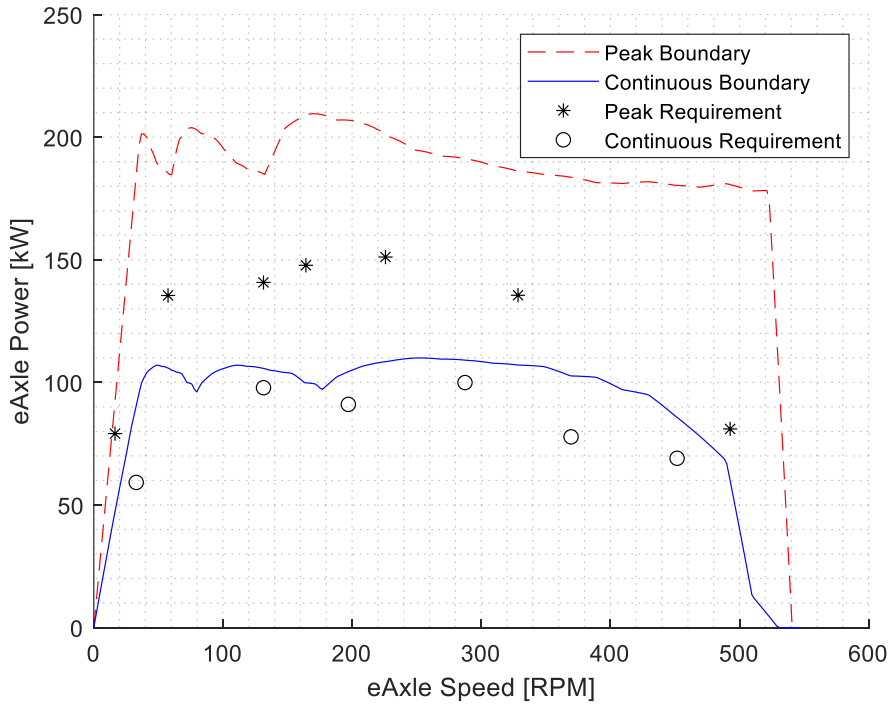



Fig. 2.20. Combined eAxle power curve and axle requirements at 650 $V_{DC}$ and a 65 °C coolant temperature.

The eAxle requires a three-speed transmission to meet all its required operating points. The first gear ratio is constrained by the maximum torque requirements at low speeds. Reducing this ratio would result in insufficient torque for grade climbs. The third gear ratio is constrained by the maximum speed requirements. Increasing this ratio would result in insufficient top speed performance. An intermediate ratio (second gear) is required to meet medium speed points that are above the maximum motor speed in first gear and above the available torque in third gear. Second gear also allows the eAxle to operate at or near its maximum power capability across most of its speed range. This is illustrated by the relatively flat power curves in Fig. 2.20. The intermediate ratio also reduces the speed-matching required as the step between consecutive gear ratios is approximately halved, resulting in faster, smoother gear shifts. While most EVs in the automotive space typically use single-speed transmissions [1], the requirements of all-terrain heavy-duty vehicles mean that this is not a feasible approach. It should be noted that the conventional mechanical driveline has a twelve-speed transmission, so electrification still provides a significant reduction in the number of gear ratios required. The benefits of this include reduced transmission cost, complexity, size and weight, along with less torque reductions due to gear changes. The eAxle's performance is is summarized in Table 2-3.

Table 2-3. Nominal eAxle performance ratings.

| eAxle Parameter | Value |
|---|---|
| Peak Torque | 54 kN m |
| Continuous Torque | 28 kN m |
| Peak Power | 208 kW |
| Continuous Power | 110 kW |

## 2.6 VEHICLE PERFORMANCE

### 2.6.1 CONSTANT-SPEED PERFORMANCE

Now that the powertrain performance is known, it is possible to revise the available torque plots from Fig. 2.9 and Fig. 2.10. The 65 kN m mechanical torque limit set by the driveshafts is replaced by the powertrain's 54 kN m torque limit as shown in Fig. 2.21 and Fig. 2.22. As discussed in the commentary on Fig. 2.19 and Fig. 2.20, the 54 kN m torque limit is set by the crownwheel gear that drives the eAxle's differential. The traction system can reach the driveshafts' 65 kN m torque limit in first gear. Again, it is important to maintain significant headroom from the traction machine's peak performance. This is particularly important for first-gear grade climbs where the traction machine is drawing large currents to produce high torque at low speed. It is wise to limit the eAxle's maximum torque in first gear to be lower than what the traction machine can achieve, so that the lower crownwheel torque limit does not negatively impact the powertrain's performance.

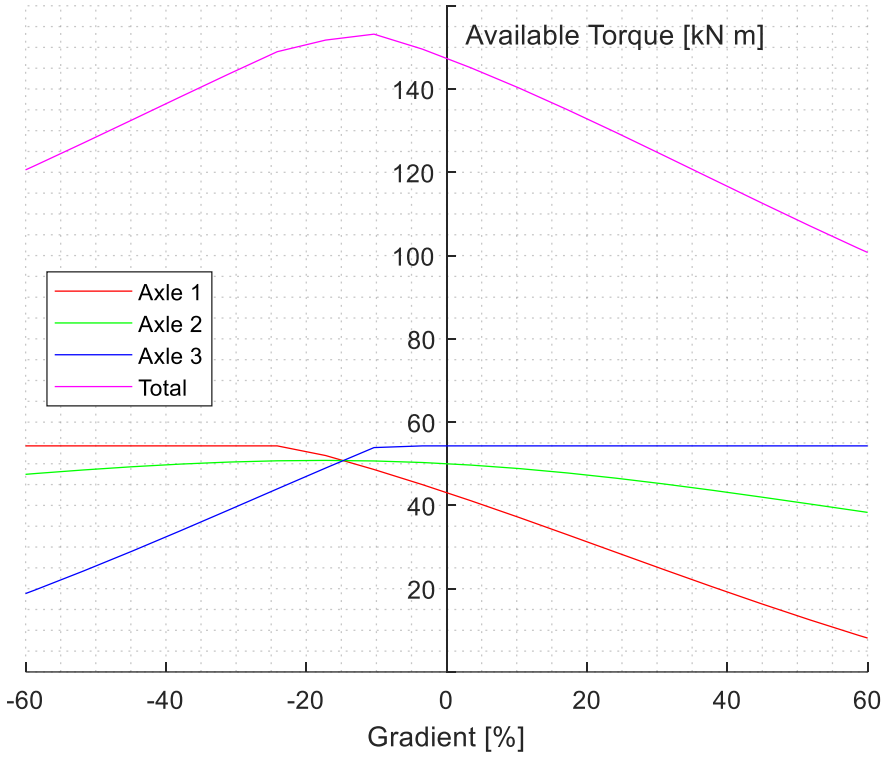



Fig. 2.21. Available torque vs. gradient.

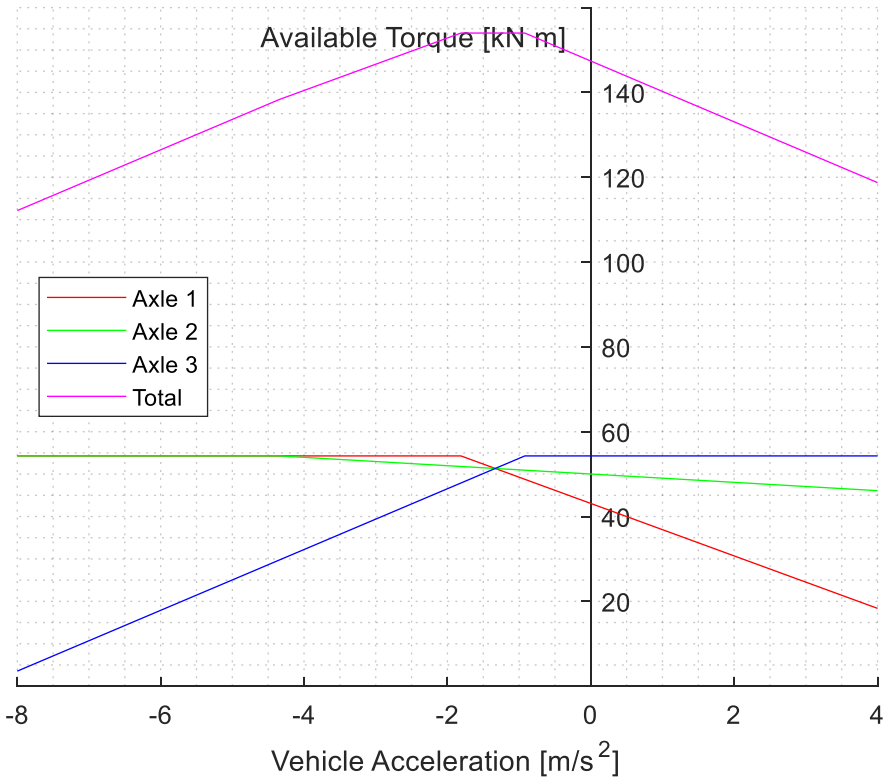



Fig. 2.22. Available torque vs. acceleration.

The 6x6 case study vehicle has three eAxles, so the total vehicle torque is three times the value shown in Fig. 2.19. Taking the minimum value of the available vehicle torque from Fig. 2.21 and the vehicle's torque-speed plot from Fig. 2.17 across the speed range gives the 3D torque map shown in Fig. 2.23 where the red surface represents the vehicle's peak available torque, the blue surface represents the vehicle's maximum continuous torque and the green surface represents the road-load torque acting on the vehicle. Note that the road-loads are calculated not measured.

By solving for the intersection between the road load surface and the tractive effort (TE) surfaces, it is possible to calculate the vehicle's maximum peak and continuous speeds on a given grade. This information is plotted in Fig. 2.24. The vehicle can meet all the required peak and continuous operating points.

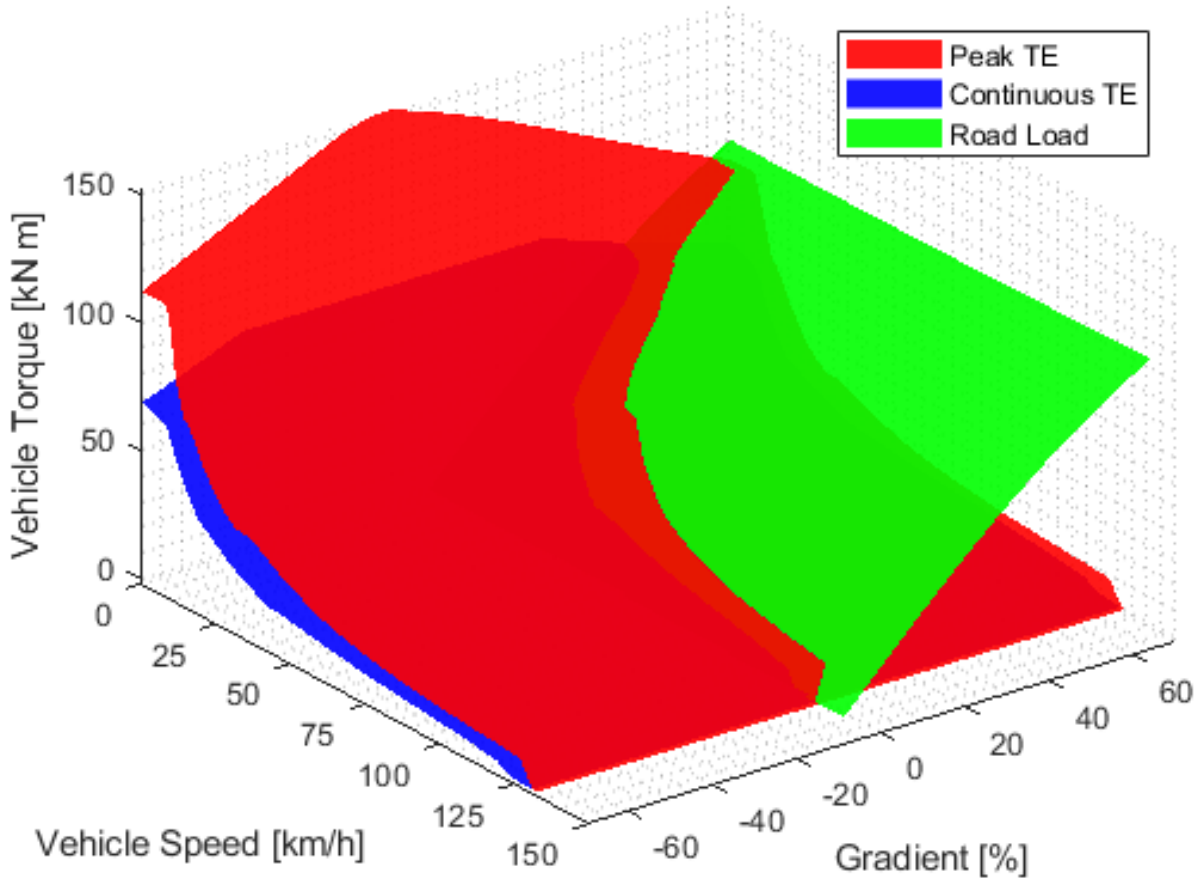



Fig. 2.23. On-road 3D torque map.

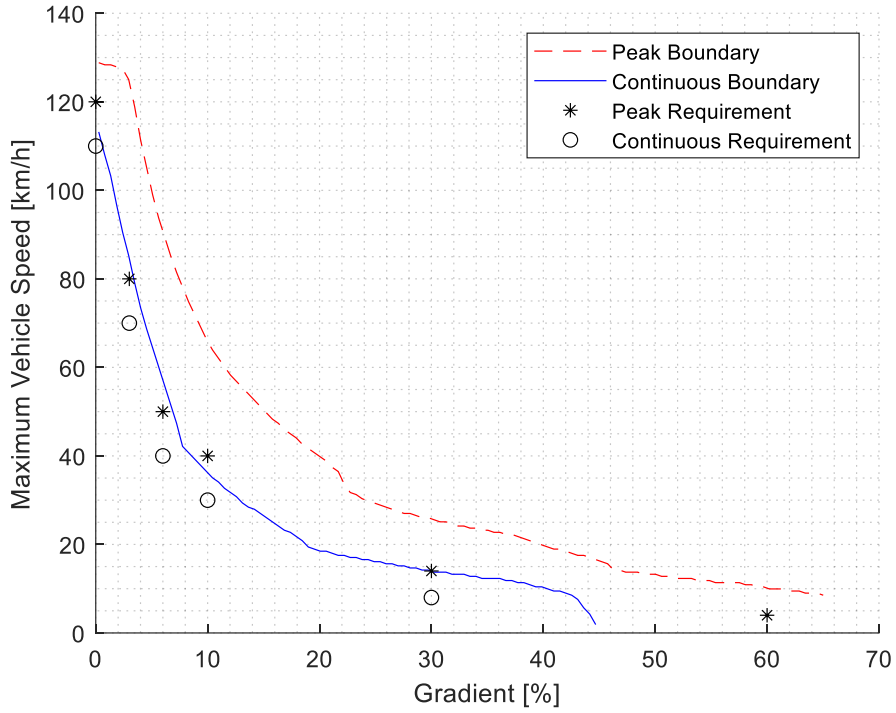



Fig. 2.24. On-road peak and continuous speed vs. grade.

### 2.6.2 ACCELERATION PERFORMANCE

The same mathematical model that is used for constant speed calculations can be used to calculate the vehicle's maximum peak and continuous acceleration performance. The resulting curves are plotted in Fig. 2.25 along with the maximum acceleration performance of the equivalent diesel vehicle. The electrified vehicle's maximum acceleration using the traction machine's continuous output is quite close to that of the diesel vehicle, but its peak performance is significantly quicker. It should be noted that the gear shifts on the electrified driveline can be staggered, changing gear on only one eAxle at a time to minimize torque disruption and maintain continuous traction. This functionality is provided by the distributed propulsion architecture of the multi-eAxle driveline. This is known as staggered gear-shifting. The simulated 8 s peak acceleration of the hybrid powertrain significantly improves on the 17 s acceleration of the diesel vehicle.

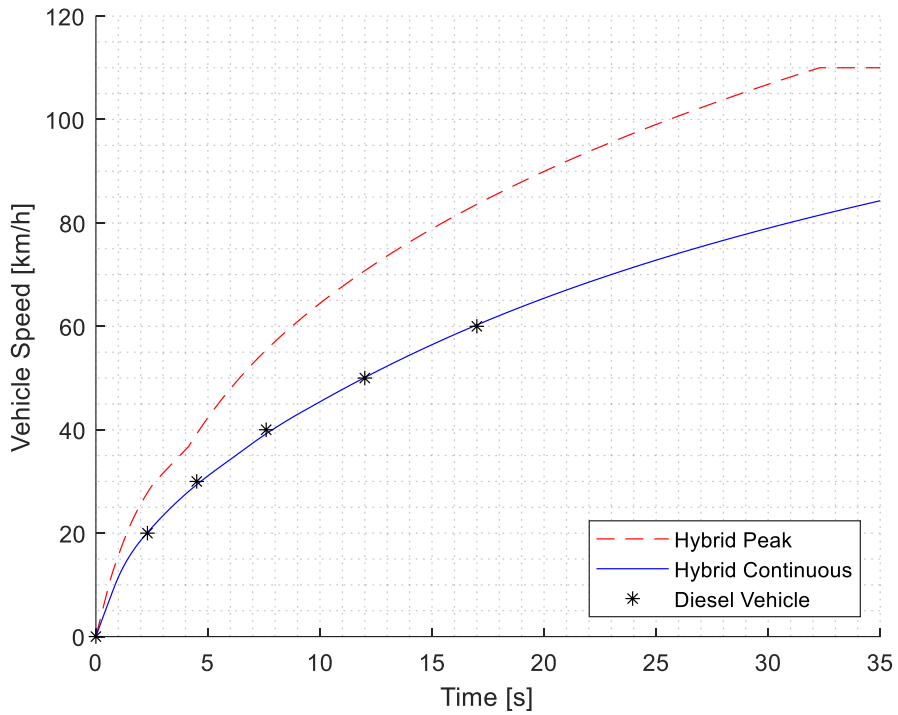



Fig. 2.25. Vehicle speed vs. time for maximum peak and continuous accelerations.

## 2.7 EAXLE TESTING

### 2.7.1 EAXLE TEST SETUP

The key objectives of the eAxle dynamometer testing program were to verify that the powertrain sizing was sufficient and to evaluate the durability of the mechanical components in the drivetrain over a duty-cycle representing the eAxle's design life. The reduction hubs were tested when the mechanical axle was developed, so this test focused on the central portion of the eAxle, known as the eDifferential, which includes the traction machine, three-speed transmission, additional reduction gearing and the differential. Fig. 2.26 shows the eDifferential before the plumbing and instrumentation were installed.

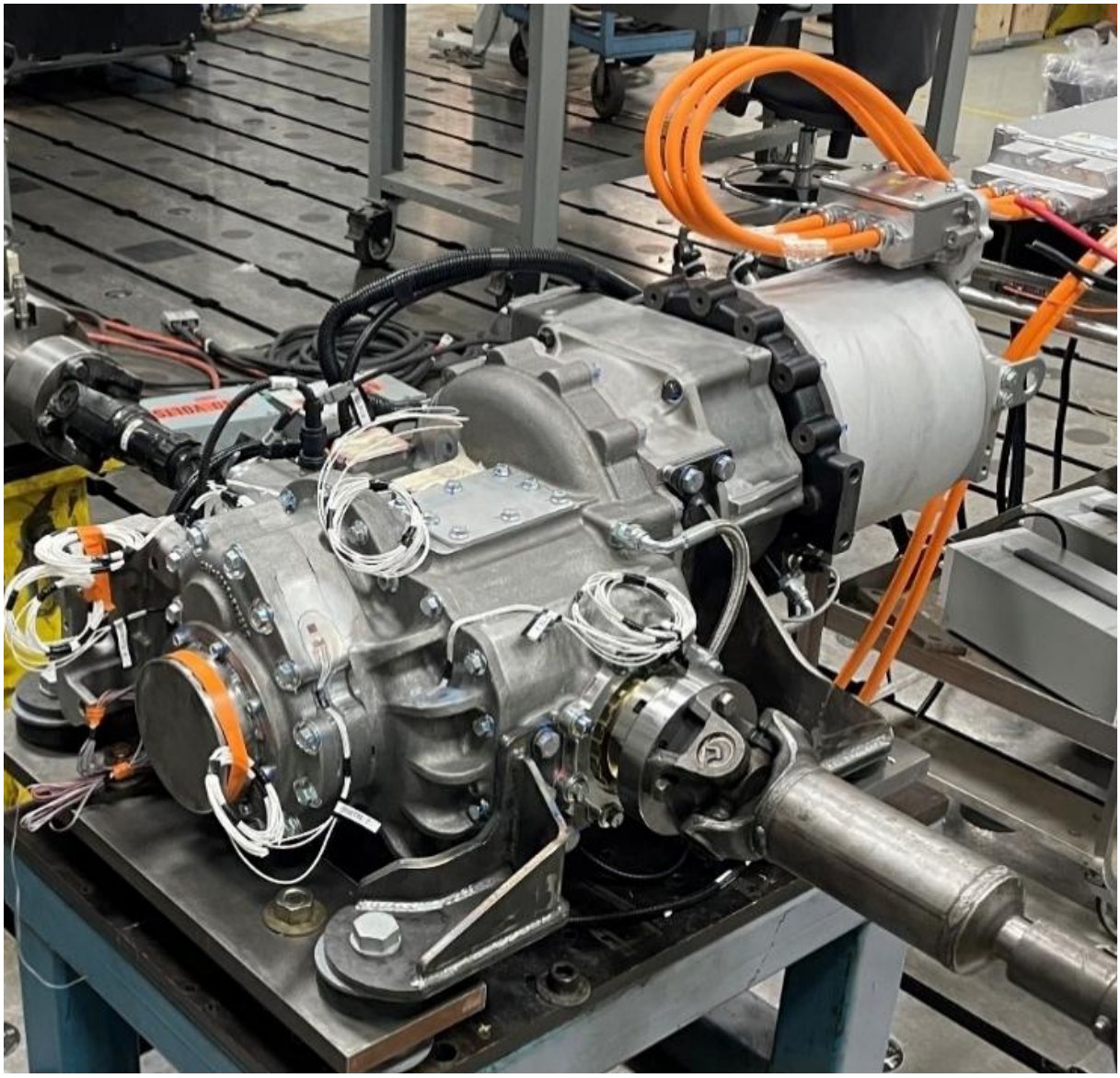


Fig. 2.26. eDifferential test hardware without plumbing and instrumentation.

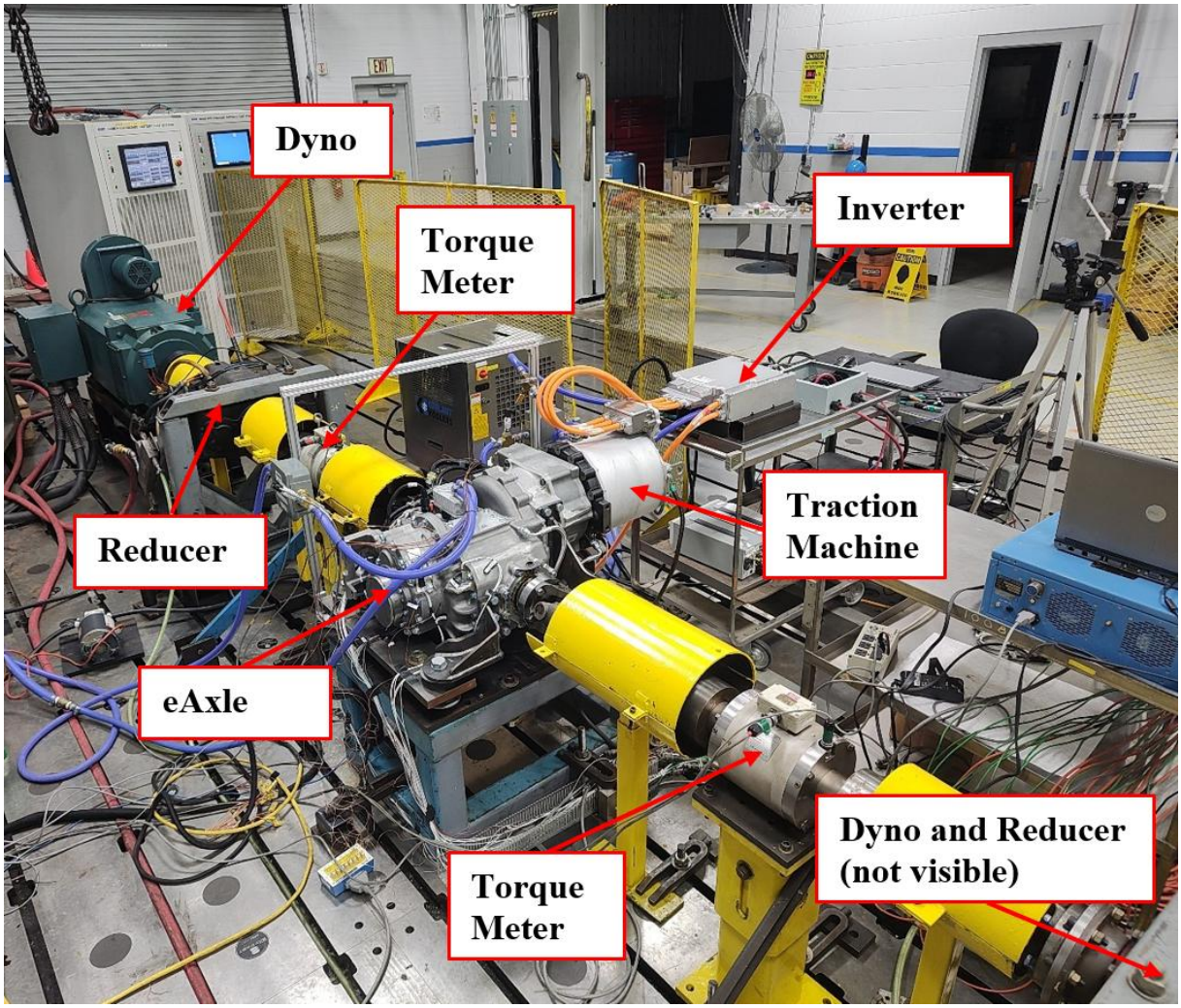



Fig. 2.27. eDifferential dynamometer test setup.

The final test setup can be seen in Fig. 2.27. The high voltage (HV) is supplied to the traction and dynamometer inverters by three parallel battery emulators. All testing was conducted at 650 V. The auxiliary low voltage (LV) is supplied by a lead-acid battery that is maintained by a DC power supply. An eAxle wiring harness, designed as part of this work is used for LV connections. The eAxle Control Unit (EACU) receives commands from the dynamometer control system using the same CAN communication interface that is implemented on vehicles. Each half-shaft (HS) is connected to its own individual torque meter, reduction gearbox and dynamometer. A glycol-water coolant mix is used to cool the inverter, motor and drivetrain. The eAxle is mounted on the same isolator mounts used in vehicles.

The following equipment is included in the test setup:

- Timoney T9000e eAxle and wiring harness (x 1).
- NHR 9300 high-voltage battery test systems (x 3).
- S Himmelstein MCRT 28007T torque meters (x 2).
- Koolant Kooler J-Series chillers (x 2).
- Spicer reduction gearboxes (x 2).
- TF100 isolator mounts (x 4).

### 2.7.2 ACCELERATED LIFE CYCLE TESTING

The accelerated life cycle testing conducted on the eAxle consisted of a series of traction and regenerative braking cycles. Two profiles were combined into a unit-cycle as shown in Fig. 2.28. Tens of thousands of these cycles were run repeatedly until the cumulative work done by the eDifferential was equivalent to its design life. The first cycle was designed using on-highway requirements and utilized all three of the eAxle's gears (denoted by 1000, 2000 and 3000 on the plot's y-axis). The second cycle represented an off-highway use case where top-speeds are lower, but higher rolling resistances result in a higher torque requirement for a given speed when compared to on-highway driving. As a result, the off-highway cycle does not utilize third gear. It should be noted that a slight speed ripple was added to the half-shaft speeds to ensure that the spider gears within the differential were rotating. This is the cause of the ripple that can be seen in the half-shaft torque curves.

Changing gear requires a temporary disconnection of the traction motor from the drivetrain so its speed can be matched to the required speed in the new gear. This is the reason for the torque reductions that can be seen in Fig. 2.28. These torque reductions in turn result in a temporary reduction in inverter current as shown in Fig. 2.29, where positive currents indicate that the eDifferential in traction and negative currents correspond to regenerative braking. The changes in polarity of torque and current during gear shifts are a consequence of the motor's speed-matching and the inertia of the eAxle loading the dynamometer after the motor torque has been removed.

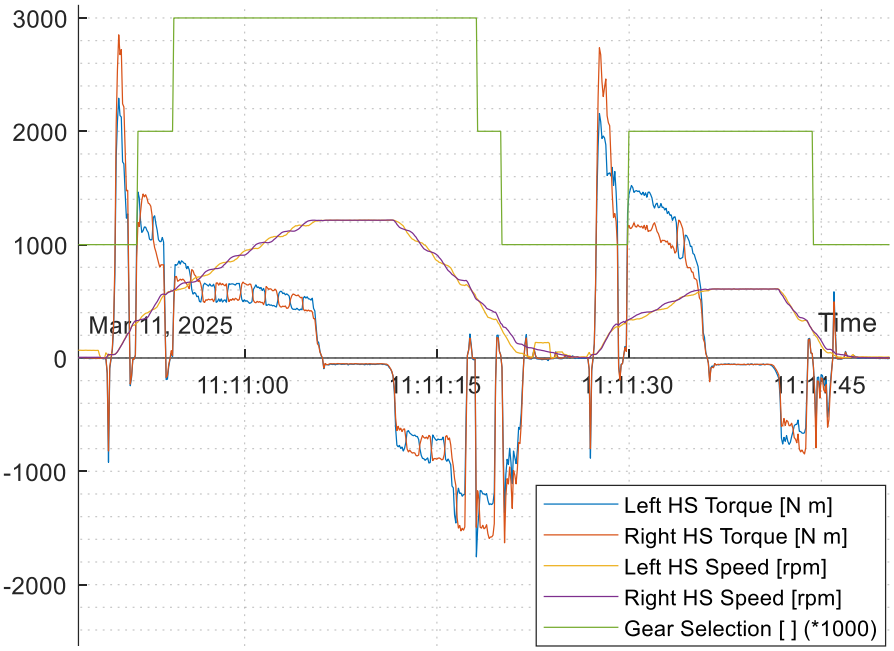



Fig. 2.28. Torque, speed and gear selection vs. time (hh:mm:ss) for the traction and regenerative braking cycle.




Fig. 2.29. DC supply voltage and inverter current vs. time (hh:mm:ss) for a traction and regenerative braking cycle.

Repeated traction and regenerative braking cycles place a higher thermal requirement on the axle compared to cruising at steady speeds. As a result, the accelerated life cycle test also served as an

evaluation of the eDifferential's cooling capability. Fig. 2.30 shows the temperatures of several components plotted over many cycles. All temperatures were well within their nominal operating ranges.

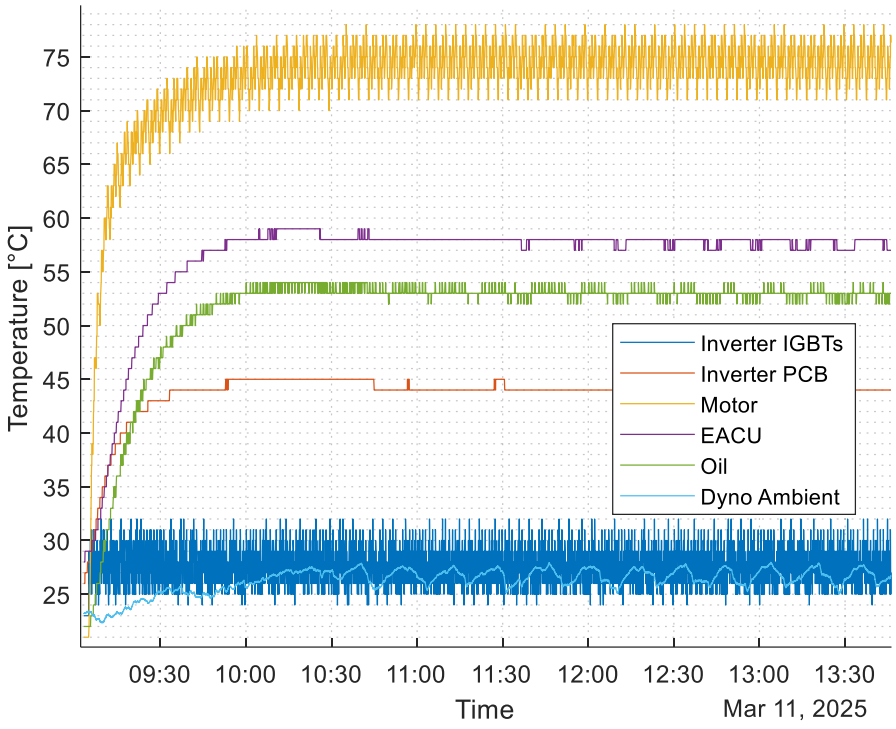



Fig. 2.30. Component temperatures vs. time (hh:mm) for many traction and regenerative braking cycles.

### 2.7.3 GRADE CLIMB TESTING

The grade-climb test is arguably the most significant test from a powertrain sizing verification standpoint. The maximum torque portion of a grade-climb typically lasts for 40 seconds and requires the traction machine to maintain a low-speed, high-torque operating point without excessive temperature rises. It should be noted that the grade-climb is a short-term event and eAxle is not expected to maintain this operating point continuously. The **crownwheel** torque is the sum of the two half-shaft torques and was specified based on the worst-case axle loading seen under gradient weight-transfer. Fig. 2.31 shows the crownwheel torque, half-shaft speeds and gear selection plotted for a single grade-climb.

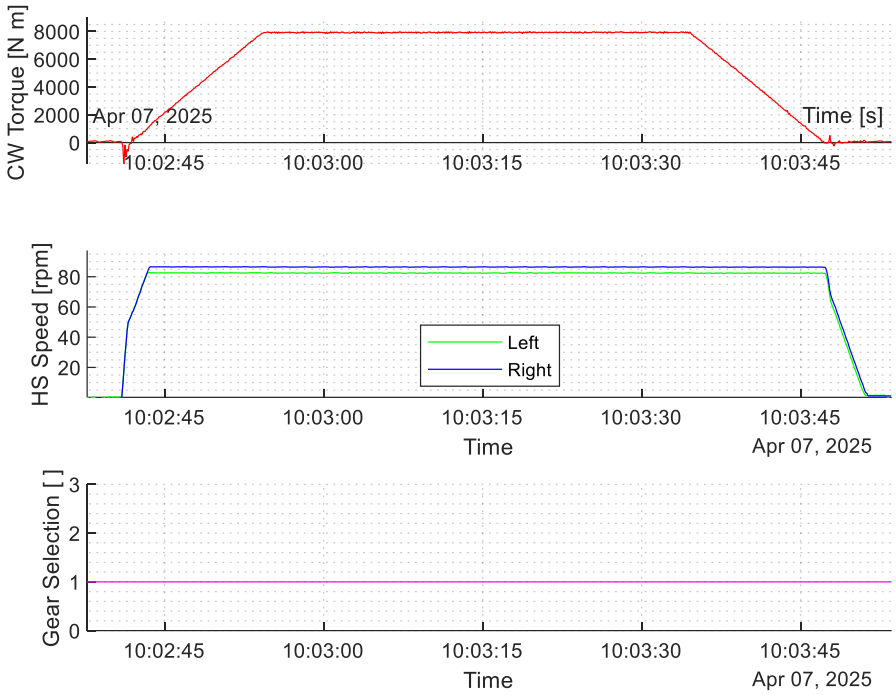



Fig. 2.31. Torque, speed and gear selection vs. time for a single grade climb.

The HV supply voltage and current for the grade-climb test are shown in Fig. 2.32. The interior permanent magnet (IPM) traction motor's speed is low enough that it stays below its base speed for the duration of the test. As a result, the inverter current draw is basically proportional to torque. Five grade-climb tests were performed in succession with some time allowed between the tests for components to cool. This is common practice in vehicle testing. Fig. 2.33 shows the temperatures of several eDifferential components over the five successive grade-climbs. While the inverter IGBT and motor winding temperatures increased during the tests, they stayed well below their operational limit for the duration of each grade climb. This verified that the powertrain components are sufficiently sized.

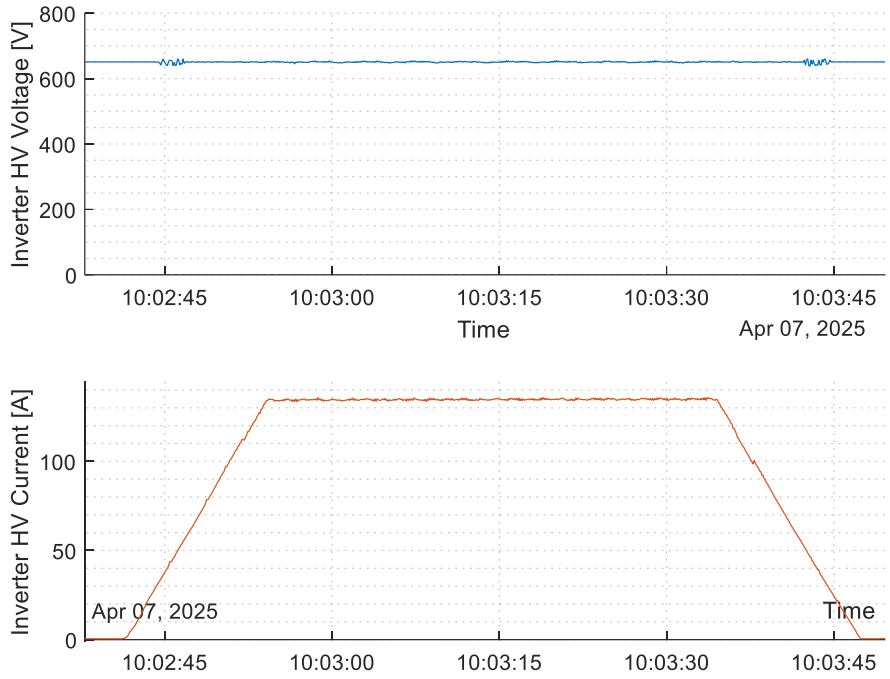



Fig. 2.32. DC supply voltage and inverter current vs. time for a single grade climb.

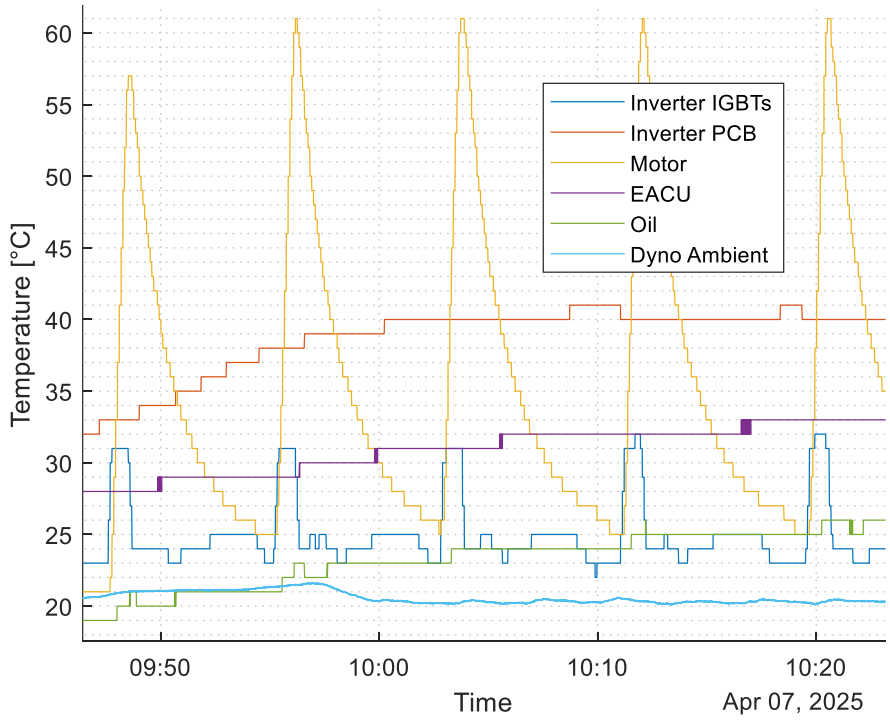



Fig. 2.33. Component temperatures vs. time for five grade-climbs.

### 2.7.4 MAXIMUM TORQUE TESTING

The purpose of the maximum torque tests was to verify that the eDifferential was able to produce its maximum output without damaging any powertrain components. Fig. 2.34 shows crownwheel torque, half-shaft speeds and gear selection for the maximum torque test. Again, the crownwheel torque is the sum of the readings from the two half-shaft torque meters. The supply voltage and inverter currents for these cycles are shown in Fig. 2.35. As was the case for the grade-climb test, the inverter's current draw is basically proportional to the eDifferential torque because the IPM traction machine remains in its constant torque region for the entirety of the test. Few conclusions can be drawn from component temperatures from cycles as short as these, so the temperature plot for this test has been omitted. All components performed as expected.

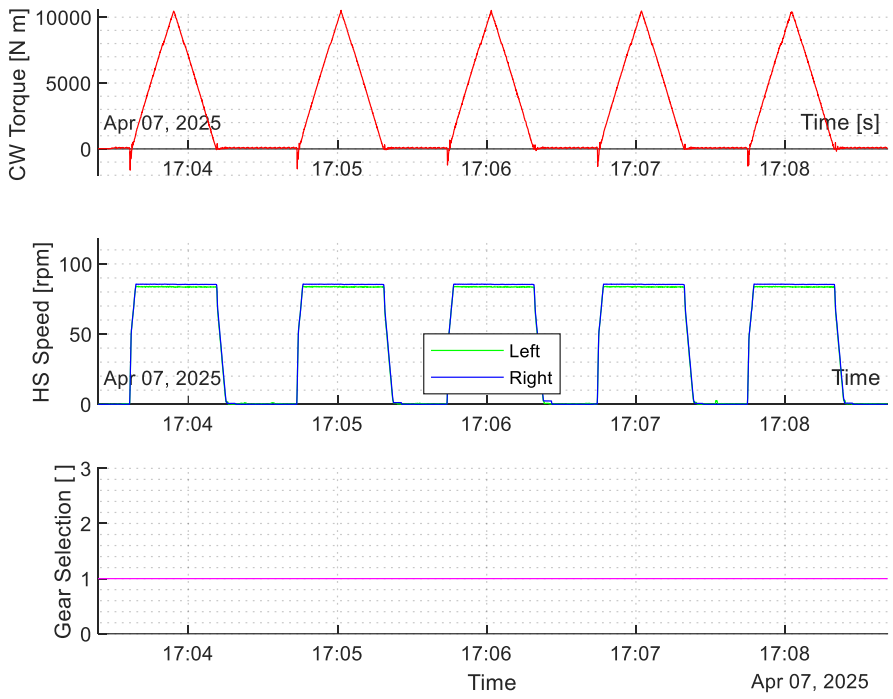



Fig. 2.34. Torque, speed and gear selection vs. time for five maximum torque cycles.

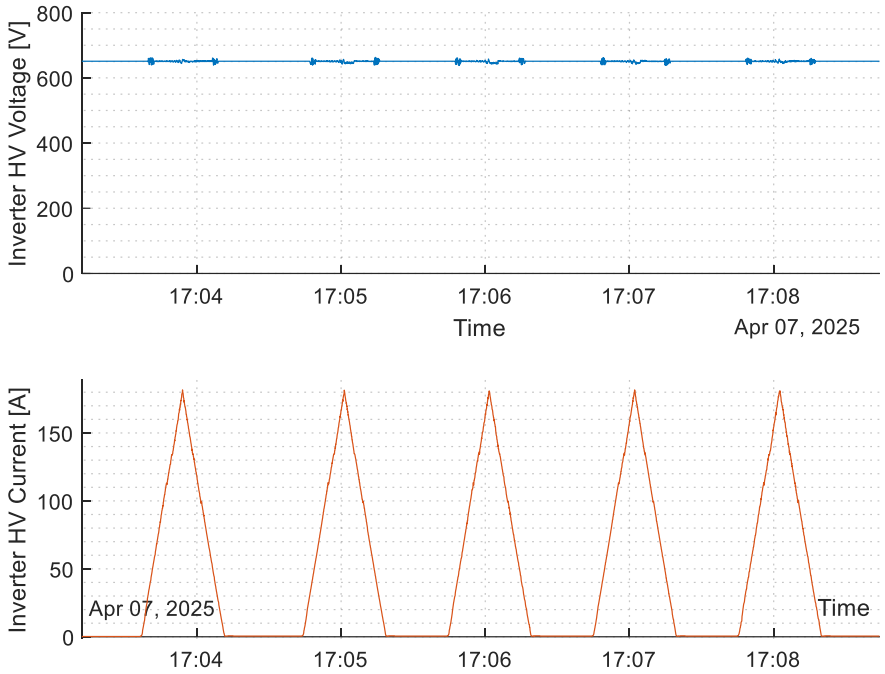



Fig. 2.35. DC supply voltage and inverter current vs. time for five maximum torque cycles.

## 2.8 CONCLUSIONS

The design and test of a modular 200 kW eAxle for all-terrain heavy-duty vehicles is discussed in this chapter. The eAxle is compatible with 4x4, 6x6 and 8x8 drivelines and maintains compatibility with the same independent suspension as its mechanically driven counterpart. The eAxle features one traction machine aligned perpendicular to the axle and can be used across multiple sectors including construction vehicles, forest machinery, fire trucks and off-highway vehicles. It is also compatible with series-hybrid, battery-electric and hydrogen fuel cell powertrains, thus ensuring compatibility with a variety of future energy sources. The powertrain was sized based on the tractive effort requirements of a 27-tonne 6x6 vehicle. A novel method considering weight transfer on gradients and wheel-slip limitations was developed for sizing the powertrain. This ensured that the powertrain was not undersized for grade-climbing. The performance of a 6x6 vehicle is evaluated for constant-speed operating points and transient accelerations. The powertrain sizing methodology is verified through an extensive dynamometer testing program of a prototype eAxle.

The eAxle is now running on several prototype vehicles at different customer locations. Future work will include further evaluation of the powertrain performance using results from in-field testing. The performance of the eAxle in various ambient operating conditions is of particular interest. The powertrain sizing methodologies that were developed for this 9 tonne eAxle will be applied to eAxles in other weight classes.

# 3 OPTIMIZED PACKAGING OF ELECTRIFIED AXLES

## 3.1 ABSTRACT

In this chapter, novel packaging concepts are developed for an eAxle for a multi-axle vehicle. The eAxle is configured in a novel "over-the-shoulder" arrangement where its motor and transmission are positioned to one side of the differential, with power to the differential being delivered by a pinion-gear that is coupled to the differential from the opposite side to the motor and transmission. The over-the-shoulder concept allows the eAxle to be packaged more symmetrically on each side of the driveshafts. This is crucial for meeting tight vehicle wheelbase requirements. The over-the-shoulder concept also facilitates the installation of auxiliary drives on the pinion-gear side of the differential. The auxiliary drives include inboard parking brakes and ground-driven steering pumps, both of which are essential to meet vehicle safety and redundancy requirements. The eAxle can be mounted with the motor facing the front or rear of the vehicle. Changing the axle's orientation is helpful for packaging other driveline components and meeting approach angle requirements. A patent application for the eAxle's novel packaging concept [42] was submitted on June 5th, 2024, and is due for publication on December 5th, 2025, 18 months after the original submission date.

Section 3.2 gives a general background on eAxle packaging. The main eAxle features and subassemblies are presented in Section 3.3. Section 3.4 describes the eAxle's auxiliary kits and drives. Integration of the eAxle into vehicles is discussed in Section 3.5. Conclusions are drawn in Section 3.6.

The work in this chapter has been published as follows:

- C. Healy, D. McCarry, M. Doody and G. Fitzpatrick, "An eAxle", United Kingdom Patent GB2408020.2, Jun. 5, 2024, to be published [42].

## 3.2 EAXLE PACKAGING BACKGROUND

eAxles typically comprise of the traction machine, transmission, differential, propulsion shafts and reduction hubs. The inverter can be mounted remotely or on the axle itself. eAxles can be configured with either one motor per-axle or one motor per-wheel. Both configurations can have their motors orientated either parallel or perpendicular to the axle's axis of rotation. This gives four main configurations of eAxle. Fig. 3.1 shows a parallel one motor per-axle configuration. A perpendicular one motor per-axle configuration can be seen in Fig. 3.2. Fig. 3.3 depicts a parallel one motor per-wheel configuration. A perpendicular one motor per-wheel configuration is shown in Fig. 3.4. For all four configurations, it is typical to include variable-speed transmission (one for each motor) in the central portion of the eAxle and a reduction gearset in the hubs.

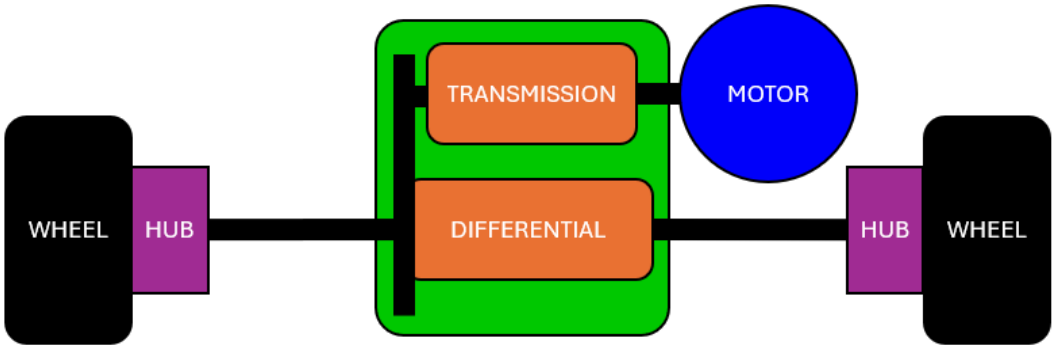



Fig. 3.1. A parallel one motor per-axle configuration.

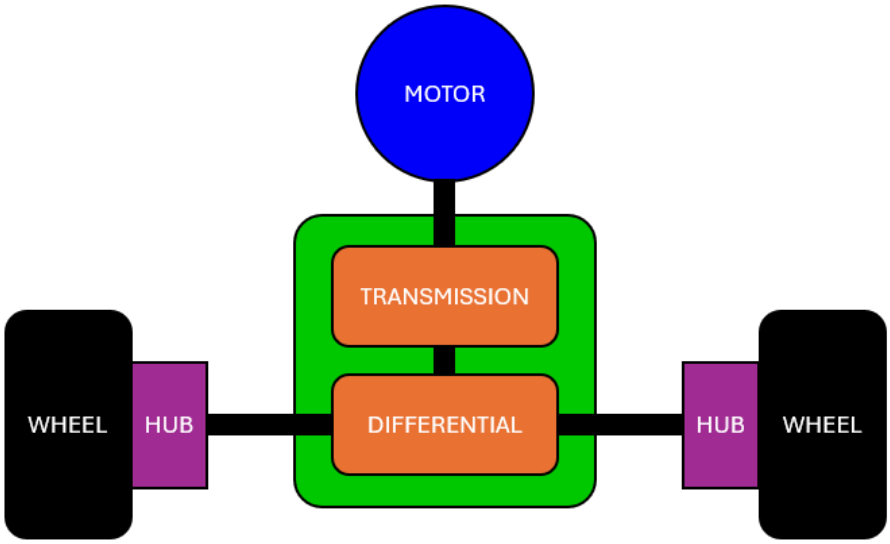



Fig. 3.2. A perpendicular one motor per-axle configuration.

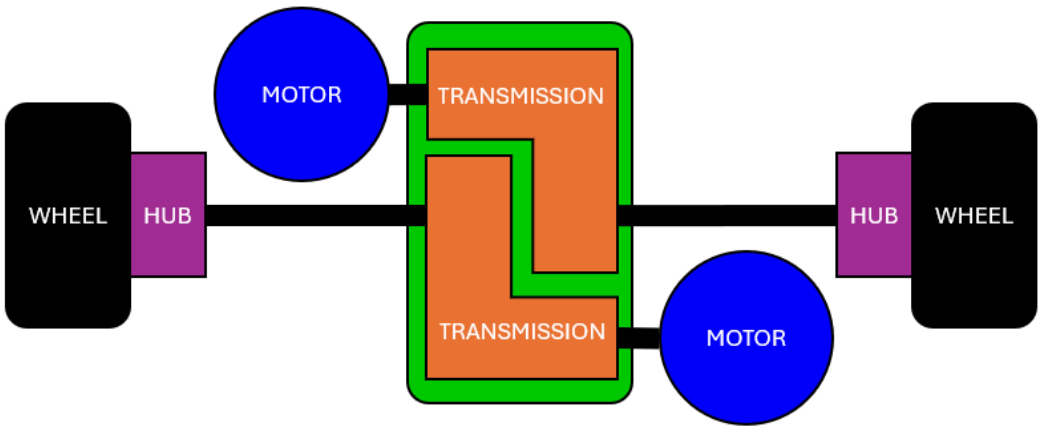



Fig. 3.3. A parallel one motor per-wheel configuration.

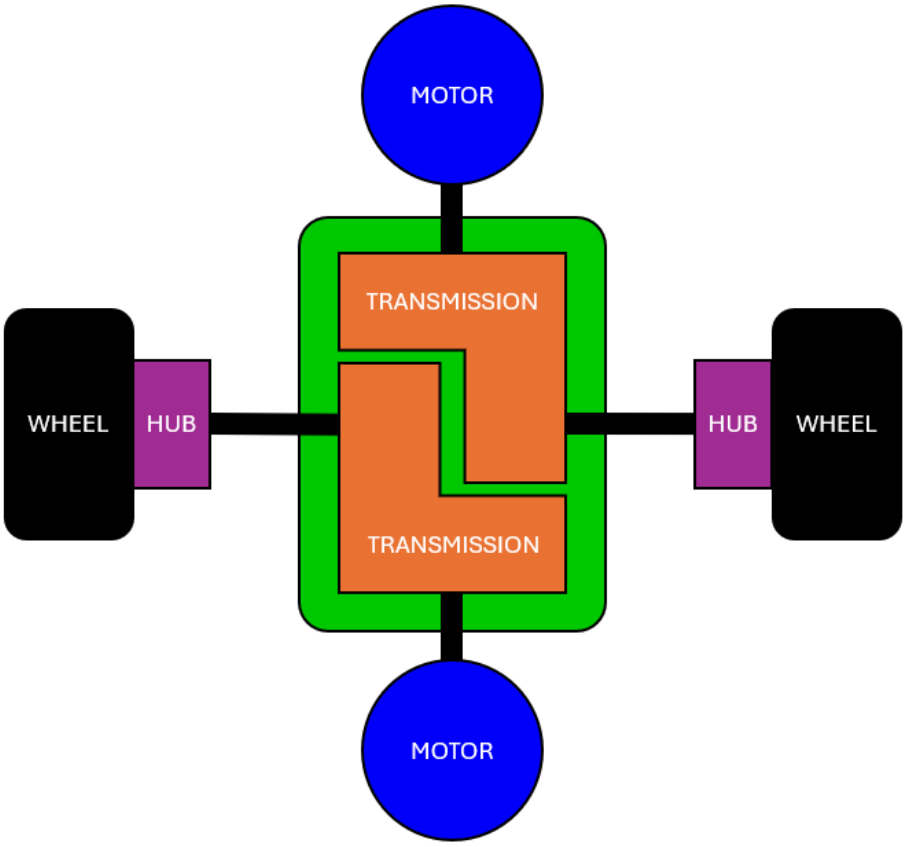



Fig. 3.4. A perpendicular one motor per-wheel configuration.

One motor per-axle configurations require a mechanical differential to split the motive torque between the wheels and to allow for variations in wheel speeds while the vehicle is cornering. The one motor per-wheel configuration allows the torque sent to each wheel station to be individually controlled. This configuration also eliminates the mechanical differential at the cost of increased component count,

higher weight, greater packaging challenges, increased control complexity. The number of motive torque sources on the vehicle is doubled, requiring a more sophisticated electronic control system and a significantly more expensive product due to the additional inverter, motor and transmission. Due to its lower cost and more favourable packaging, the one motor per-axle configuration is preferred for the modular eAxle designed for multiple applications. They may be of use cases where the advantages provided by increased controllability warrant the use of a one motor per-wheel configuration, but for most applications this is not the case.

Parallel configurations have the advantages of enabling the eAxle to package into vehicles with shorter wheelbases and removes the need for a bevel or hypoid gearset to rotate the power flow by 90 °. The latter can provide improvements in drivetrain efficiency. However, at the power scale of interest in this work, it is not possible to package an independent suspension parallel configuration within road-legal vehicle width requirements. The perpendicular configuration overcomes the trackwidth limitation by orientating the motor and transmission along the central axis of the vehicle at the expense of increased axle length. This can limit the minimum achievable wheelbase and cause cantilever loads due to the relatively large overhang of the motor and transmission to one side of the eAxle's driveshafts. A novel one motor per-axle perpendicular packaging concept that overcomes these issues is introduced in Section 3.3.

It is also possible to position the motor, transmission and reduction gearing in the hub. However, there are several issues that prevent this concept being implemented in this application. These include packaging limitations imposed by insufficient power density from commercially available motors, issues with suspension and steering articulation. There are increased survivability concerns as the motors and transmissions are in the unsprung portion of the vehicle and not protected from shock loads and vibration by the vehicle's suspension system. Even if such a concept was feasible, component cost and weight would have to increase to meet the increased packaging and durability requirements. An in-hub topology is shown in Fig. 3.5.

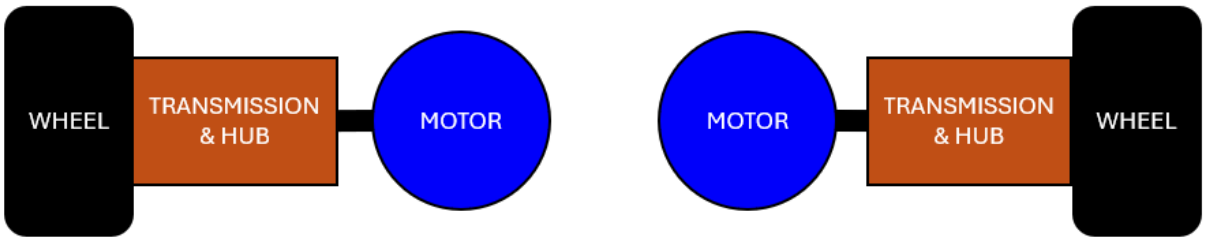



Fig. 3.5. An in-hub motor configuration.

### 3.3 eAxle Features and Packaging

Fig. 3.6 [5] shows a Computer-Aided Design (CAD) rendering of the eAxle, annotated with descriptions of its key features. The main subassemblies of the eAxle are exploded and labelled in Fig. 3.7 [5].

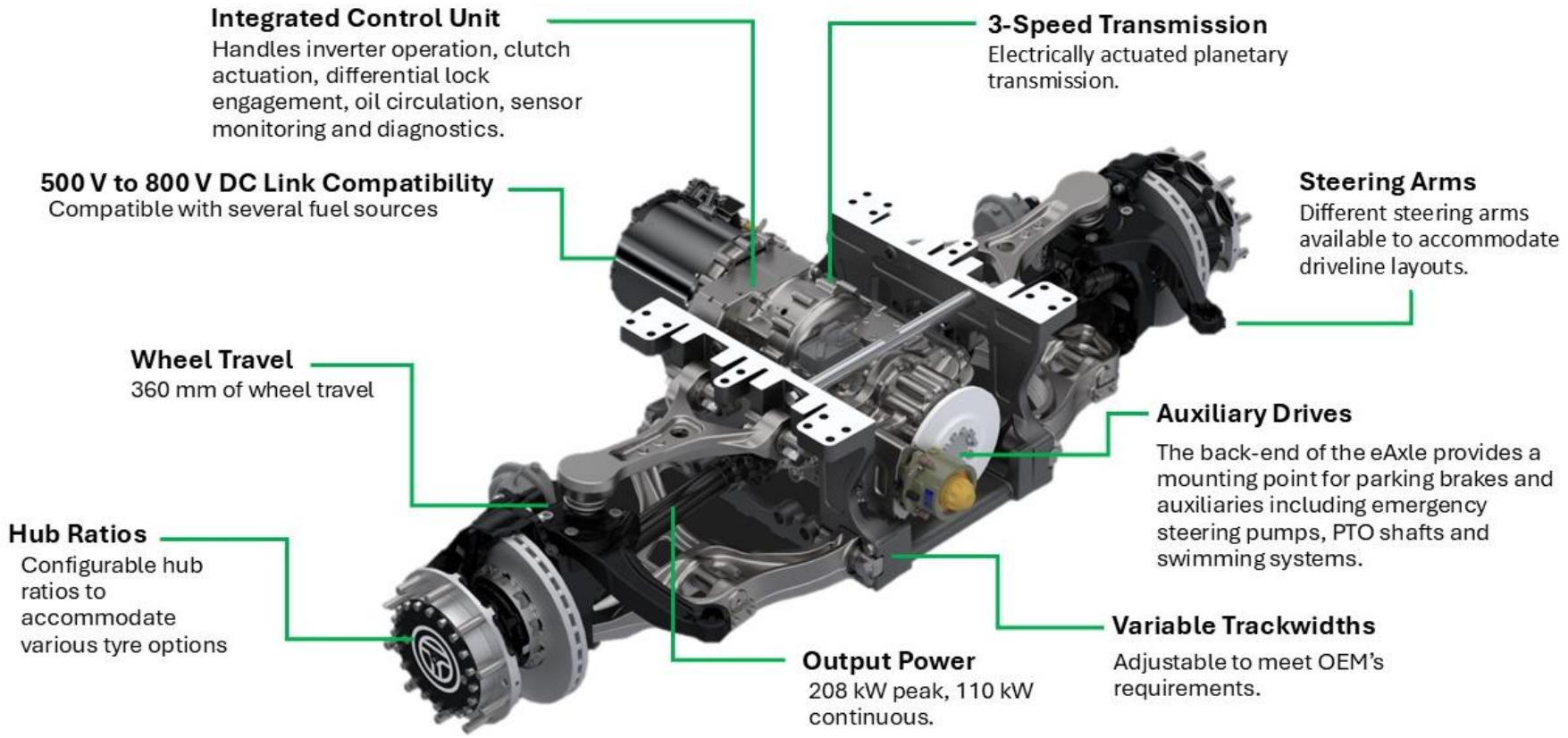



Fig. 3.6. eAxle features.

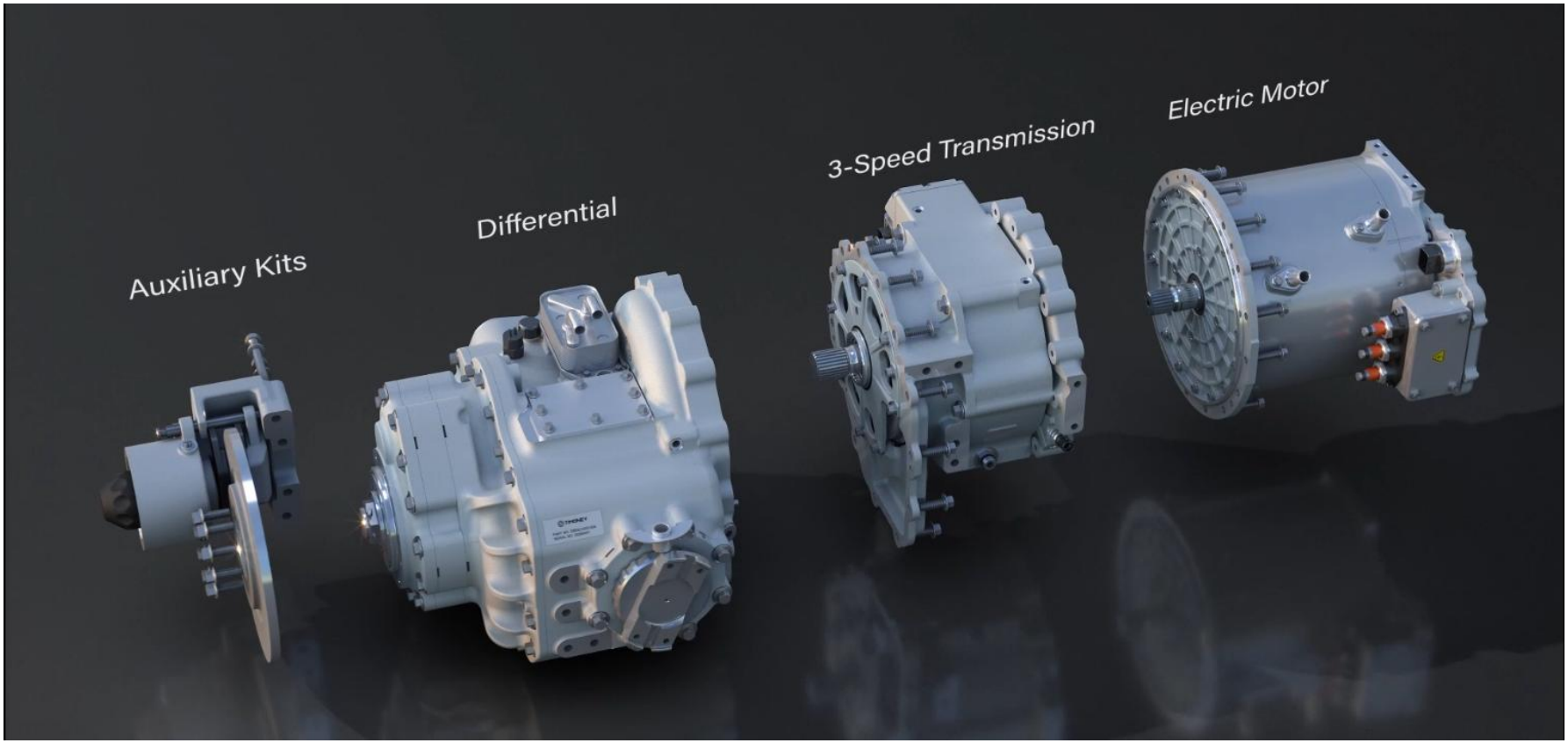



Fig. 3.7. eAxle subassemblies.

The eAxle's inverter and motor system is compatible with DC link voltages between 500 V and 800 V. The axle's three-speed transmission is required to meet the vehicle performance requirements from its intended applications as discussed in Section 2.5. The transmission uses planetary gears and electrically actuated clutches to maximise power density. The eAxle is designed to be as modular. Multiple steering arm geometries are available, the axle's trackwidth is variable, and the gear ratios in the reduction hubs can be configured based on tire size and the intended vehicle application. Several auxiliary kits and drives can be mounted on the differential portion of the eAxle. These are discussed in detail in Section 3.4. The independent suspension system allows 360 mm of wheel travel.

The eAxle's power flow is depicted in Fig. 3.8. Note that this is a schematic and is not to scale. The electric motor drives through a three-speed planetary transmission into the differential portion of the eAxle. Planetary transmissions are highly efficient, versatile, and compact gear systems capable of providing multiple gear ratios and distributing loads effectively. Their design allows for high torque transmission with both smooth shifting and efficient operation in a variety of applications. It should be noted that the electric motor's ability to rotate in both directions eliminates the need for a reverse gear.

The routing of power through the differential portion of the eAxle is where the novelty in this packaging concept lies. Traditional layouts place the pinion gear that drives the differential on the same side of the differential as the motor and transmission: this results in excessive eAxle length. In this eAxle, an over-the-shoulder concept is used. In this novel concept the transmission output shaft passes over the differential (over-the-shoulder) and drives a set of drop gears, drop gear 1 and drop gear 2 in Fig. 3.8. Drop gear 1 is higher than drop gear 2. Drop gear 2 drives the differential's pinion gear and its central axis is located at the same height as the central axis of the differential. Placing the central axes of the pinion and differential at the same height reduces friction which improves efficiency relative to offset hypoid gears and allows power to be transferred through the differential in both directions, thus, enabling regenerative braking.

This novel over-the-shoulder concept allows the powertrain to be distributed more symmetrically about the eAxles drive shafts, allowing for shorter vehicle wheelbases and reducing cantilever loads imposed on the assembly by the overhang of the motor and transmission. In addition to the advantages that are attributed to the compact nature of the assembly, the location of the pinion in a different plane to that of the output shaft allows for auxiliary kits and drives to be coupled to the eAxle assembly. The importance of these auxiliary kits is discussed in the next section.

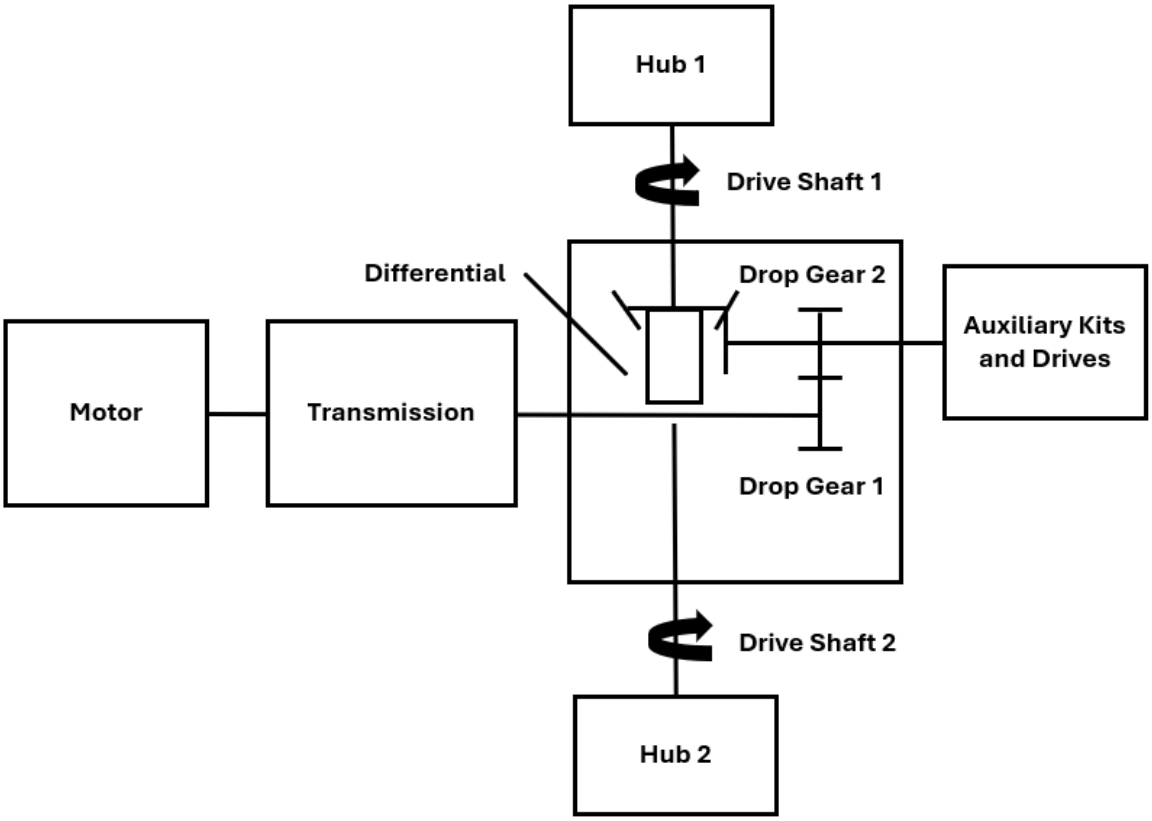



Fig. 3.8. eAxle power flow.

### 3.4 AUXILIARY KITS AND DRIVES

Fig. 3.9 [5] shows the differential portion of the eAxle along with the four auxiliary drive kits. The numbered auxiliary drive kits shown are 1. a cover (i.e. no kit), 2. a spring-applied hydraulic-release inboard parking brake, 3. a ground-driven emergency steering pump, and 4. a tandem spring-applied hydraulic-release inboard parking brake and ground-driven emergency steering pump.

The parking brake is engaged by default due to the application of a force through a spring engaging the calliper onto the disc. A hydraulic feed is used to release the calliper. The parking brake disc is directly coupled to the differential's pinion shaft. Thus, when engaged, the parking brake will restrict the rotation of the drivetrain.

The purpose of the ground-driven emergency steering pump is to assist in scenarios where vehicle hydraulic system failures are encountered. This can be particularly problematic in the context of hydraulically-power-assisted steering. In the event of failure of the primary hydraulic systems, a backup pump is used to provide an alternative or secondary source of hydraulic fluid, powered from the rotation of the wheels. In the event of vehicle breakdown, towing the vehicle will cause rotation of the wheels

which will provide power for the pump. The pump can then provide a source of pressurized hydraulic fluid that can be coupled into other vehicle modules such as the hydraulic steering system.

There are also options for auxiliary drives including power take-off (PTO) shafts that can be used to drive loads external to the axle.

The eAxle shown in Fig. 3.6 is equipped with the spring-applied hydraulic-release inboard parking brake kit. An eDifferential with the ground-driven emergency steering pump kit can be seen in Fig. 3.10 [5] and an eDifferential with the tandem spring-applied hydraulic-release inboard parking brake and ground-driven emergency steering pump kit is shown in Fig. 3.11 [5].

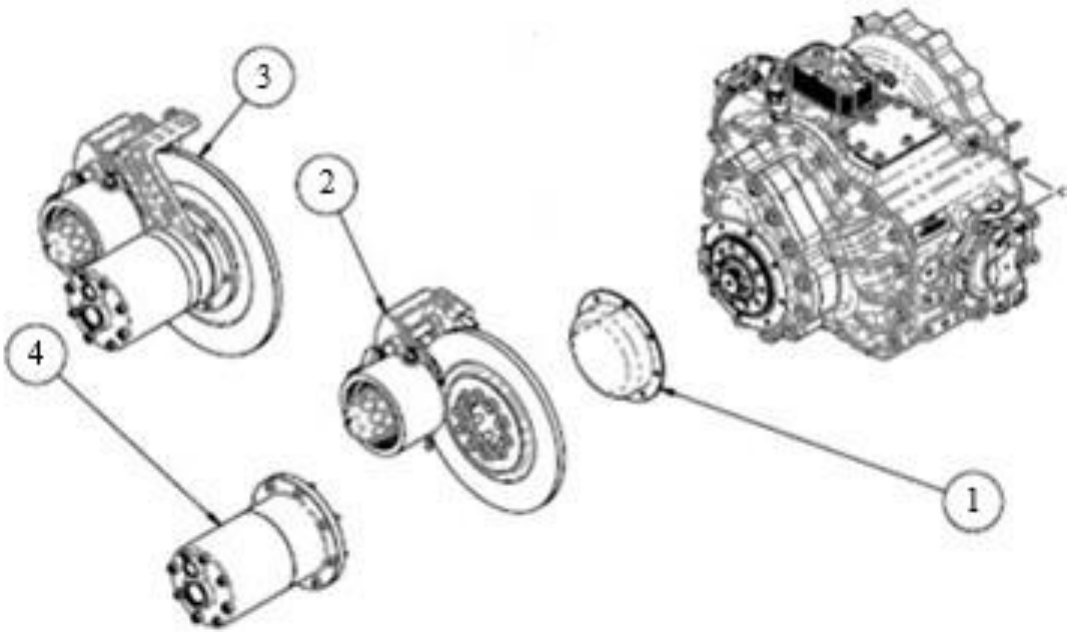



Fig. 3.9. eAxle auxiliary kits and drives.

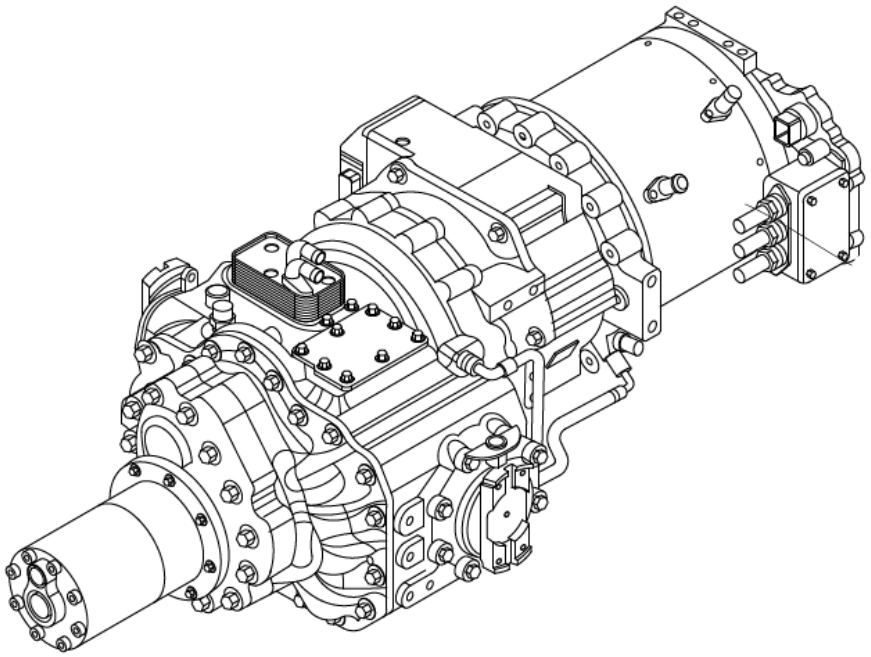


Fig. 3.10. An eDifferential with the ground-driven emergency steering pump kit.

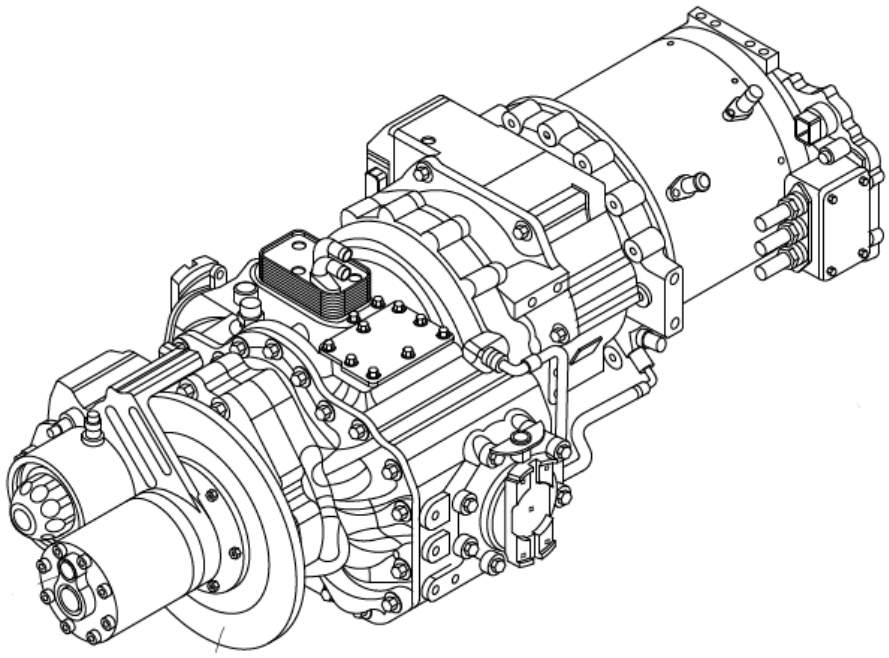


Fig. 3.11. An eDifferential with the tandem spring-applied hydraulic-release inboard parking brake and ground-driven emergency steering pump kit.

It should be noted that the auxiliary kits feature allows for parking brakes to be positioned at the individual eAxle level. Since there is no mechanical connection between eAxles, it is not possible to

implement parking braking on the transfer case as with a conventional mechanical driveline. The weight-transfer-based wheel-slip limitations on available torque, discussed in Section 2.3, also apply to the available torque from parking brakes meaning that a distributed parking brake layout is required to meet vehicle hill-hold requirements.

Per axle and vehicle total parking brake torques for a 36,000 kg 8x8 vehicle, plotted against gradient are shown in Fig. 3.12. The vehicle has an inboard parking brake on each axle. Axle 4 uses a tandem parking brake and emergency steering pump kit. The horizontal portions of the per-axle parking brake torque curves correspond to the axles being parking brake torque limited rather than wheel-slip limited. Axle 4 has a higher parking-brake torque limit due to the larger disc diameter on the tandem parking brake emergency steering pump kit used on this axle compared to the standard parking brake kit used on axles 1-3. The available vehicle parking brake torque and the vehicle's hill hold requirement are plotted against grade in Fig. 3.13. The parking brake configuration is sufficient to meet the 60 % grade hill-hold requirements in both directions.

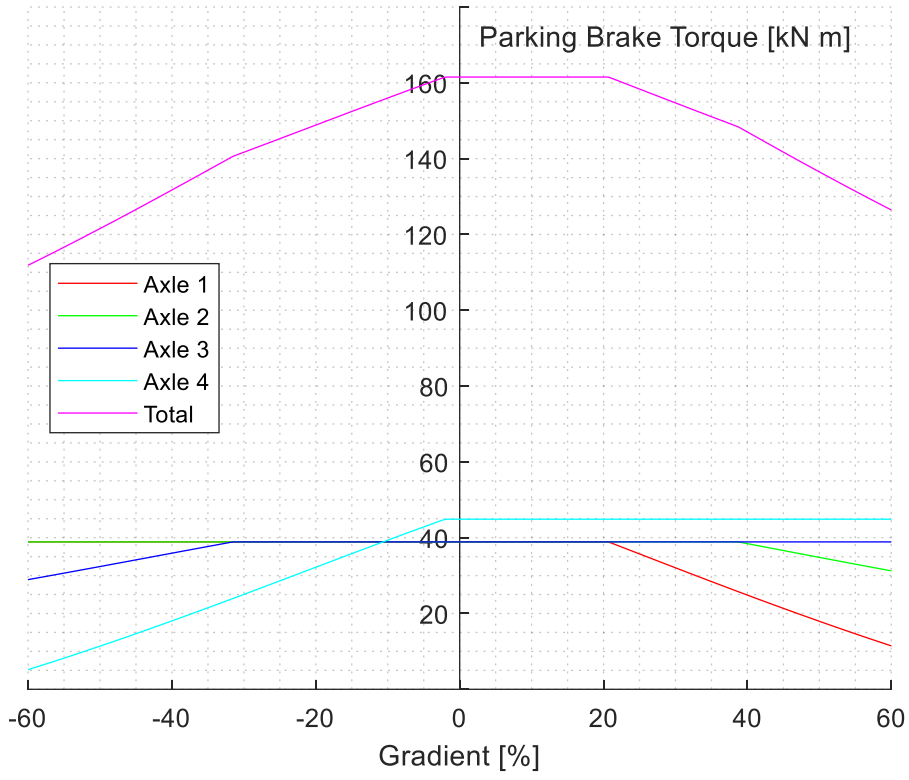



Fig. 3.12. Axle and vehicle parking brake torques vs. gradient.

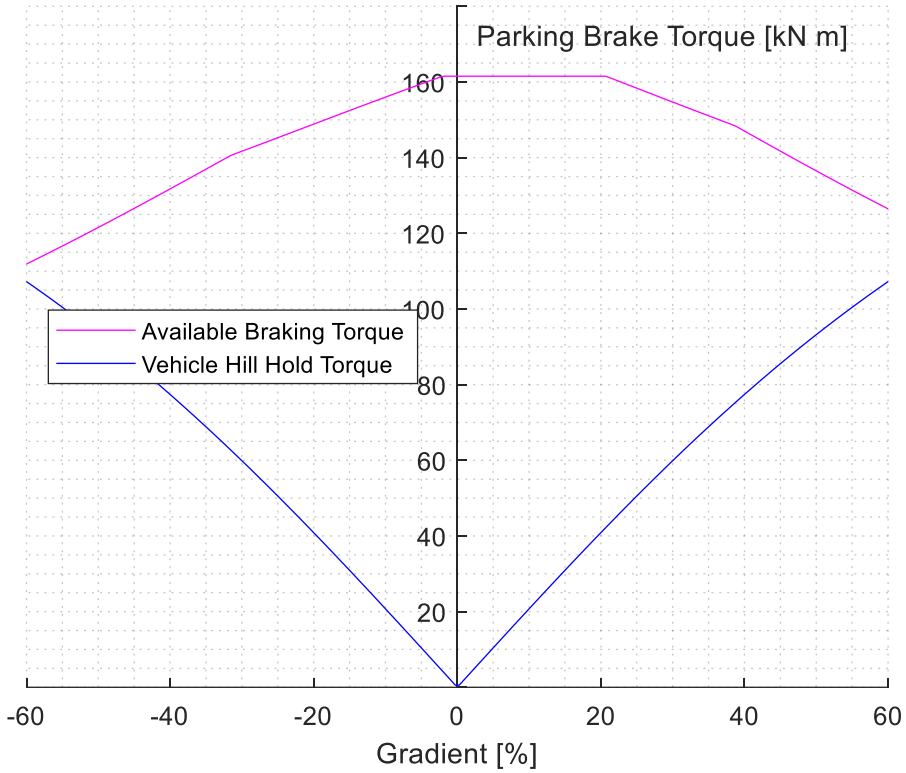



Fig. 3.13. Vehicle parking brake torque and hill hold requirement vs. gradient.

### 3.5 VEHICLE INTEGRATION

Another key feature of the eAxle is that it can be mounted with the motor facing the front or rear of the vehicle. Depending on the eAxle orientation, the direction of the helix on the differential's crownwheel and pinion gears along with the two drop gears is reversed. This ensures that the contact forces between the gears cause separation rather than attraction when positive torque is applied. Changing the eAxle's orientation allows for greater flexibility in driveline packaging and is particularly useful when routing steering arms and linkages. Fig. 3.14 [5] shows an 8x8 driveline with the motors on all four eAxles facing rearward, while an 8x8 layout with two eAxles facing forward and two eAxles facing rearward is shown in Fig. 3.15 [5].

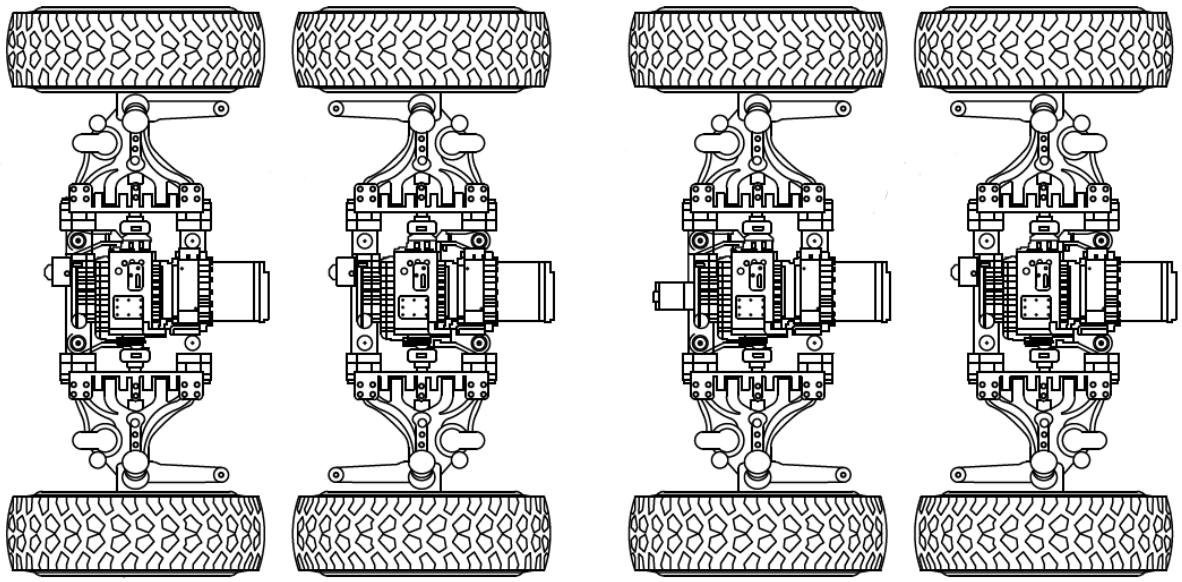


Fig. 3.14. An 8x8 driveline layout with all eAxles orientated rearward.

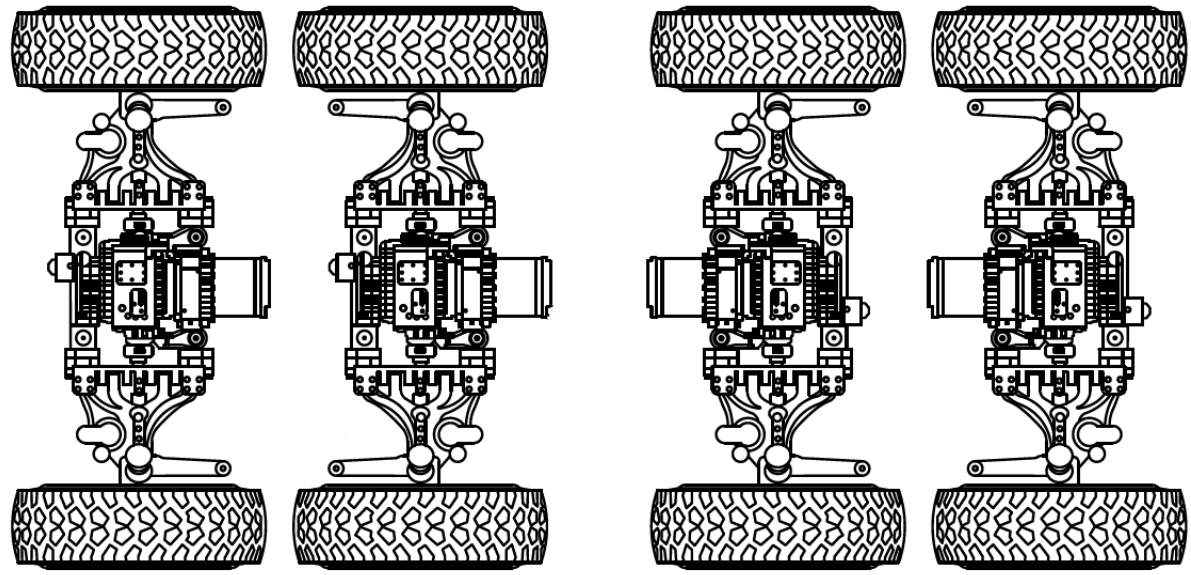


Fig. 3.15. An 8x8 driveline layout with two eAxles orientated forward and two eAxles oreintated rearward.

Orienting the motor away from the ends of the vehicles (i.e. orientating the motor rearward on the front axle and orientating the motor forward of the rear most axle) allows for increased vehicle approach and departure angles. The maximum approach angle is the steepest incline that a vehicle can transition onto from a level grade without colliding with the incline. The maximum departure angle is the steepest incline that the vehicle can transition from onto a level grade without colliding with the incline.

## 3.6 CONCLUSIONS

This chapter describes the packaging of a modular eAxle. A novel over-the-shoulder arrangement is created where the motor and transmission are placed to one side of the differential with power to the differential being delivered by a pinion-gear from the opposite side to the motor and transmission. The over-the-shoulder concept allows for more symmetric packaging eAxle relative to its driveshafts. This is critical for meeting tight vehicle wheelbase requirements. The over-the-shoulder concept allows auxiliary kits and drives to be installed on the pinion-gear side of the differential. The auxiliaries include inboard parking brakes and ground-driven steering pumps, both of which are required for vehicle safety and redundancy. The eAxle can be mounted with the motor facing towards the front or rear of the vehicle. Varying the orientation of eAxles in a driveline is helpful for packaging other driveline components around the eAxles and meeting approach and departure angle requirements. A patent application for the novel over-the-shoulder packaging concept [42] was submitted on June 5th, 2024. Publication is expected on December 5th, 2025, 18 months after the original submission date.

Future work will include a continuous evaluation of the latest state-of-the-art powertrain components and their introduction into the eAxle package. This continued innovation will bring new features and benefits, further advancing the technology demonstrated in this chapter.

# 4 GEAR SELECTION ALGORITHMS FOR MULTIPLE SPEED ELECTRIFIED AXLES

## 4.1 ABSTRACT

This chapter describes the development of an efficiency-optimized automatic gear selection map to maximize the performance of a 9-tonne modular eAxle for all-terrain heavy-duty vehicle applications. Raw power loss data for the eAxle's inverter and motor system is analysed and processed allowing power loss and efficiency maps for each component along with combined inverter and motor system to be developed. The resulting efficiency maps for each of the eAxle's gears are calculated and mapped to a common set of lookup vectors before the most efficient gear for each operating point is selected. While this gear selection map is optimal from an efficiency perspective, practical considerations prevent it from being directly implemented on vehicles. These issues are resolved by developing efficiency-derived upshift and downshift curves for each gear transition. The performance of these gear shift curves is compared with the efficiency-optimized map in simulation. The gear selection strategies are verified via an extensive dynamometer testing program with eAxle hardware.

The inverter and motor power loss and efficiency maps are analysed and post-processed in Section 4.2. The eAxle's efficiency-optimized gear selection map is produced in Section 4.3. Practical gear selection curves for the eAxle are developed in Section 4.4. An overview on dynamometer testing of a full-scale eAxle with a focus on gear selection is provided in Section 4.5. Conclusions are drawn in Section 4.6.

The work in this chapter has been published as follows:

- C. Healy and J. G. Hayes, "An efficiency-optimized gear-shift map to maximise the performance of a modular e-axle", *International Scientific Conference on Electric Power Engineering (EPE)*, 2024 [7].
- C. Healy and J. G. Hayes, "An efficiency-optimized automatic gear-selection map for a 200 kW modular eAxle", *IEEE Transactions on Transportation Electrification*, under review [6].

## 4.2 INVERTER AND MOTOR POWER LOSS AND EFFICIENCY MAPS

The analysis in this paper uses industry-representative power loss maps for the inverter and motor. The system is analysed at a 650 V DC link voltage, a typical value for heavy-duty vehicles, along with worst-case values for the traction machine's copper winding temperature and the inlet coolant temperature to the inverter and motor system. Using the highest winding and coolant temperatures gives the most pessimistic estimate of eAxle performance. This ensures that vehicle performance will not be overestimated, and cooling systems will not be undersized. The control algorithms used on the eAxle can respond to changes in voltage and component temperatures.

The power loss data for the forward traction and regenerative braking quadrants of the machine's operation was indexed to the 30 speed points and the 61 torque points provided by the supplier. There were some issues with the raw data. First, the low resolution of the data points gave rise to potentially poor accuracy when taking data from the nearest data point during a drive-cycle analysis for fuel economy, and second, there was data missing in the operating regions near the peak traction boundary.

It is essential to have accurate power loss and efficiency data available along the peak torque boundary curve as this is the region where the maximum performance of the vehicle is characterized. The first step in creating a more useable set of power loss maps is to extrapolate this data based on the available data. Reference [1] provides a detailed overview on calculating semiconductor and traction machine power losses, but many of the required parameters for these calculations are not available from the suppliers. However, torque in an electric machine is basically proportional to current. At the peak boundary curve, maximum current is being injected into the machine, meaning that it is reasonable to assume that the inverter and motor are conduction-loss dominant at their peak operating points [1], [43], [44]. For this reason, in this study, power loss was extrapolated in proportion to the ratio of the torque increase squared.

Fig. 4.1 shows the data points that were provided along with the additional data points that were added to allow the peak traction performance to be characterized.

Once the extrapolation was completed, the nest step was to increase the resolution of the data by interpolating the power loss points onto lookup vectors with a finer step size. The resolution of each array was increased by a factor of 10 giving 610 torque points and 300 speed points.

While the above resolution increase may seem excessive at this stage, it is important to note that this number of torque and speed data points will need to cover the eAxle's entire torque-speed range once the transmission is considered. It is essential to map the power loss and efficiency maps in each gear to a common set of eAxle lookup vectors for the combined transmission output so that the eAxle's performance can be characterized in a single lookup table. The resolution of this single lookup table will be the resolution of the inverter and motor system maps divided by the maximum gear ratio used in the eAxle's transmission. This means that the resolution of the inverter and motor maps at this point

must be high enough to allow adequate resolution to be maintained in each individual gear once they are mapped on to a common set of eAxle torque and speed lookup vectors.

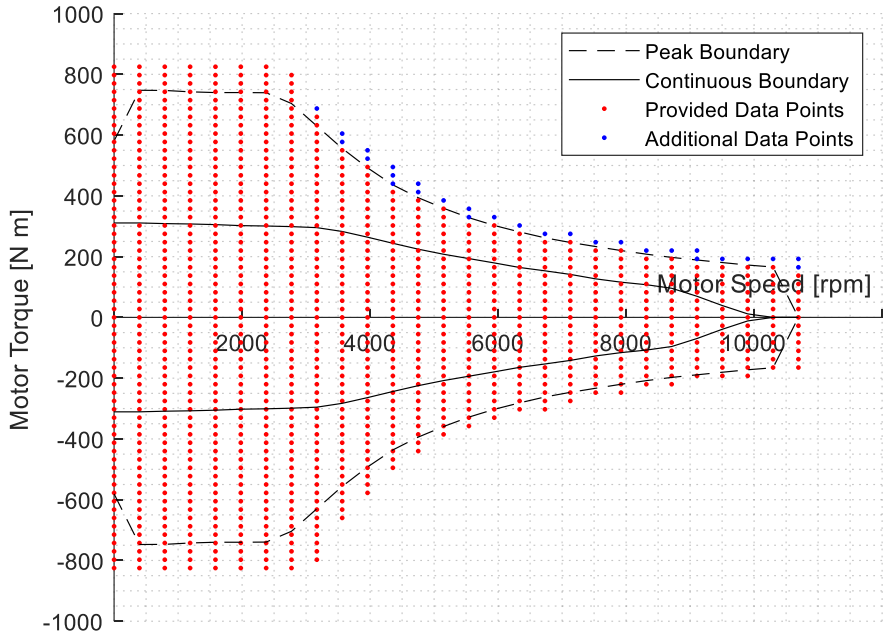



Fig. 4.1. Inverter and motor system power loss map showing missing data.

The inverter and motor system's power loss map must be calculated for each operating point. The combined inverter and motor system power loss and efficiency maps produced from the industry supplied data are shown in Fig. 4.2 and Fig. 4.3.

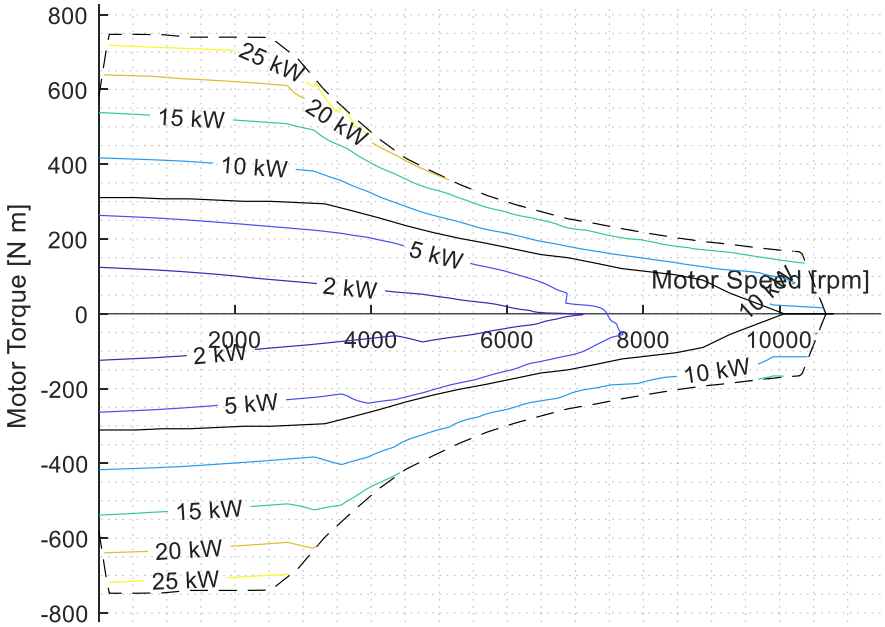



Fig. 4.2. Combined inverter and motor system power loss map.

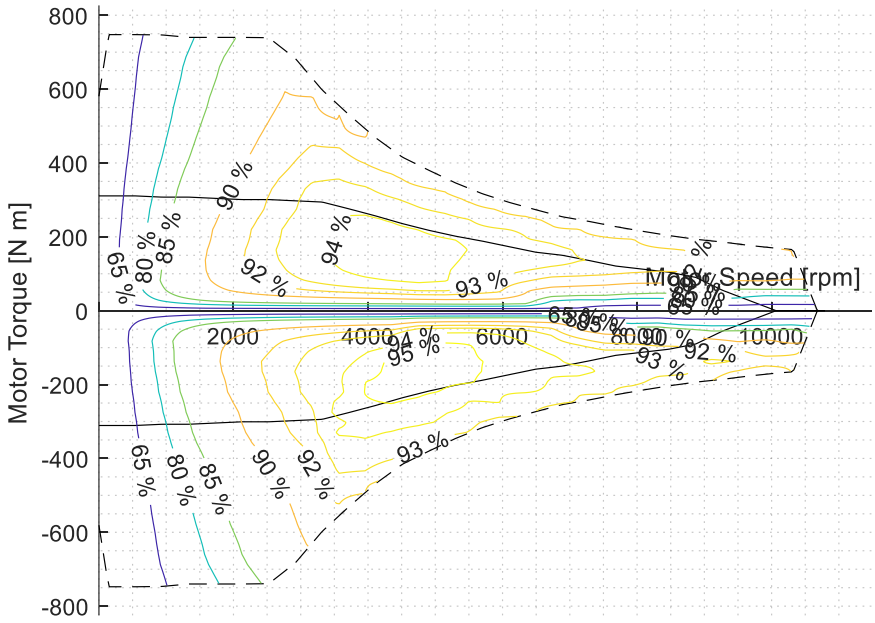



Fig. 4.3. Combined inverter and motor system efficiency map.

## 4.3 eAxle Power Loss and Efficiency Maps

In this section, the inverter and motor system power loss and efficiency maps are cascaded with industry representative drivetrain power loss and efficiency maps to produce overall power loss and efficiency maps for the eAxle system.

It is necessary to define the eAxle's boundary curves for each gear in order to facilitate the calculation of the efficiency-optimized eAxle gear selection map. This is done by multiplying the motor's peak and continuous boundary curves by each gear's ratio and efficiency. It is also useful to convert from rotational speed to vehicle speed at this stage, which is done using the tire's rolling radius. This produces the plot of the peak and continuous torque vs. speed for each of the three gears as shown in Fig. 4.4.

Note that some torque-speed operating points in Fig. 4.4 are only attainable with one gear ratio meaning that there is only available gear ratio for the efficiency-optimized gear selection map. For operating points where either two or three gear ratios are available optimized gear selection becomes an option.

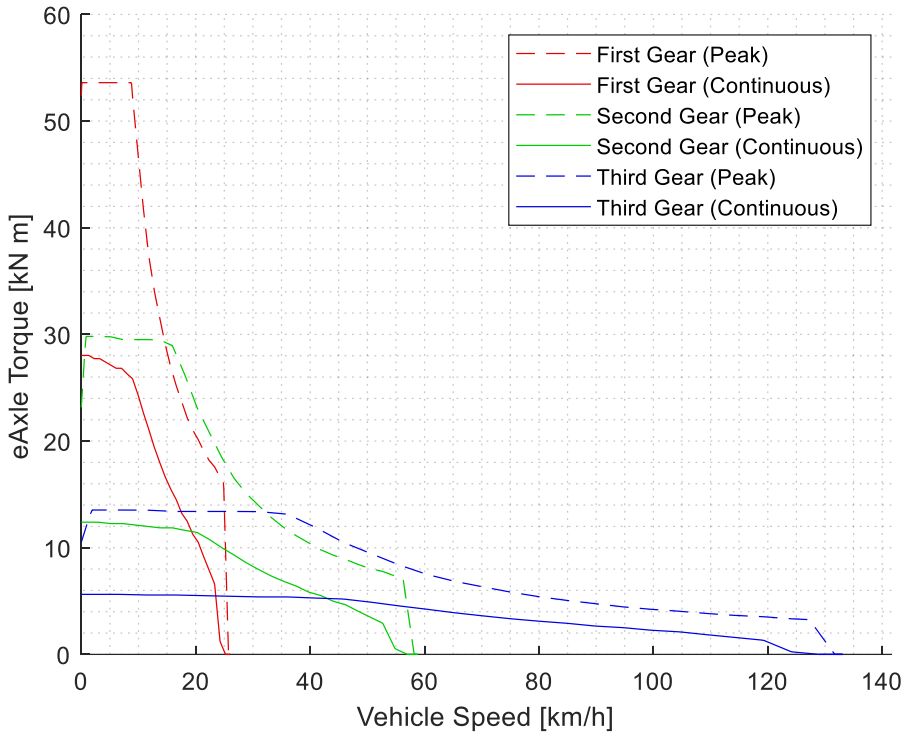



Fig. 4.4. eAxle peak and continuous torque curves for individual gears.

The eAxle efficiency maps for each gear are calculated by multiplying the combined inverter and motor efficiency map by each gear's ratio and drivetrain efficiency map. It should be noted that the drivetrain losses in this eAxle are dominated by the final drive portion of the axle which is common to all three gears. The efficiency variation between each of the three gears in the transmission is relatively small compared to the efficiency variation at different traction machine operating points, so from an efficiency optimization perspective, the traction system is of most interest. The first and second gears drive through planetary gearsets that have an average efficiency of approximately 97 % across their operating range. Third gear bypasses the planetary gears and goes straight from the traction machine to the final drive, so the nominal transmission efficiency can be taken as 100 % in this case. Thus, while gear efficiencies

are considered, the eAxle's efficiency map is largely a function of the inverter and motor system efficiency maps which were discussed in the previous section.

The efficiency maps for all three gear ratios were interpolated onto a common set of eAxle torque and speed lookup vectors enabling the most efficient gear for each operating point to be selected. The power loss maps were obtained by summing the inverter and motor power losses with the drivetrain power losses.

The eAxle's efficiency-optimized gear selection map is shown in Fig. 4.5. The power loss and efficiency maps for this gear selection can be seen in Fig. 4.6 and Fig. 4.7. While the gear selection map in Fig. 4.5 is optimal for eAxle efficiency, there are several practical issues that prevent it from being implemented on a vehicle. These include intersections of the gear selection curves at low speeds and portions of the gear shift curves that cannot be expressed as a function of torque. The latter is due to multiple speed values on the same gear change curve mapping to the same torque value. For any curve to be expressed as a mathematical function, each input (torque in this case) must map to a unique output (speed in this case). Finally, there is no gear shift hysteresis in the gear selection map. A lack of hysteresis results in excessively frequent gear change requests at operating points near the gear shift curves. This is demonstrated at the end of Section 4.4.

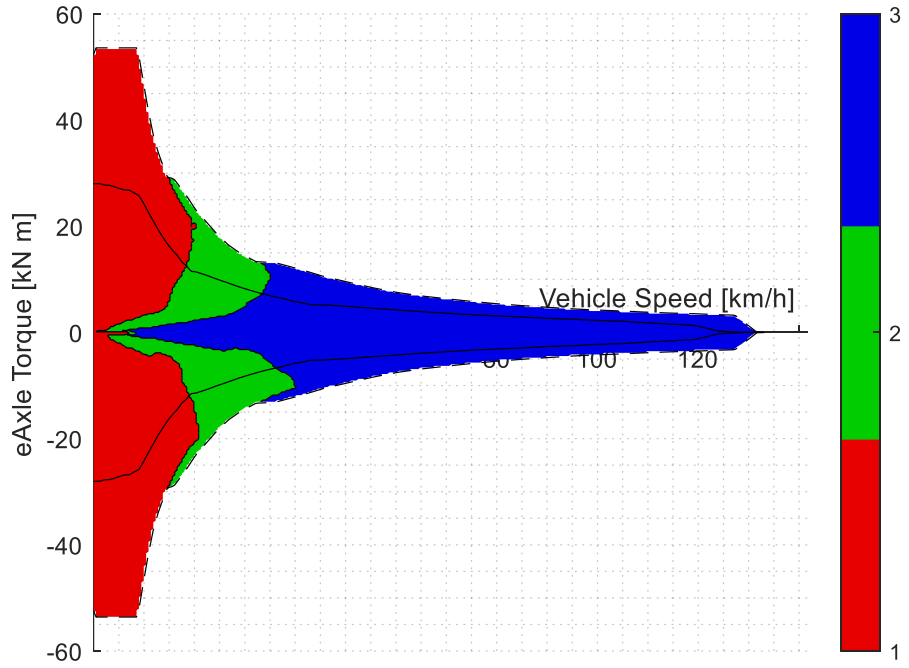



Fig. 4.5. Efficiency-optimized gear shift map (red - first gear, green - second gear, blue - third gear).

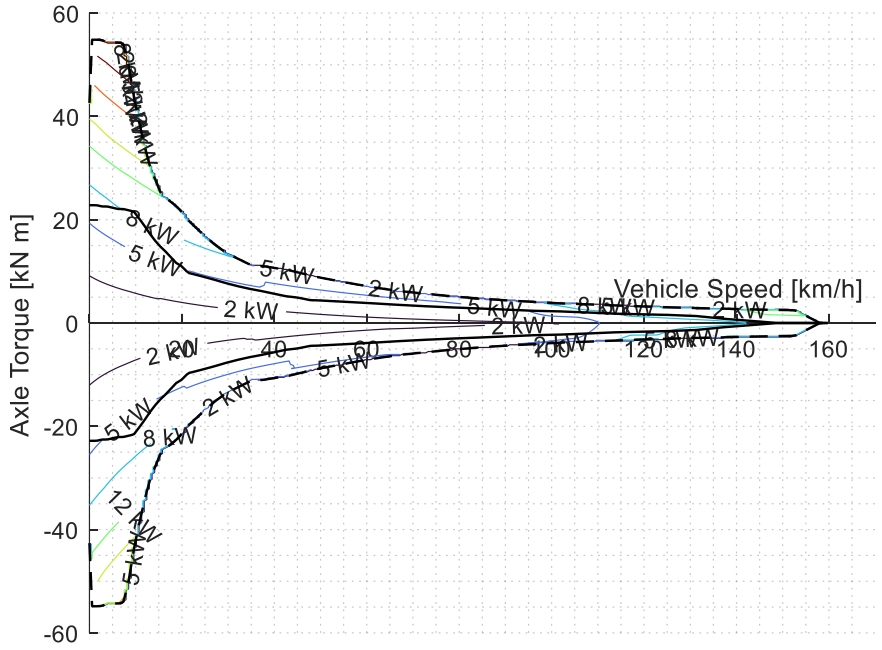



Fig. 4.6. Efficiency-optimized eAxle power loss map.

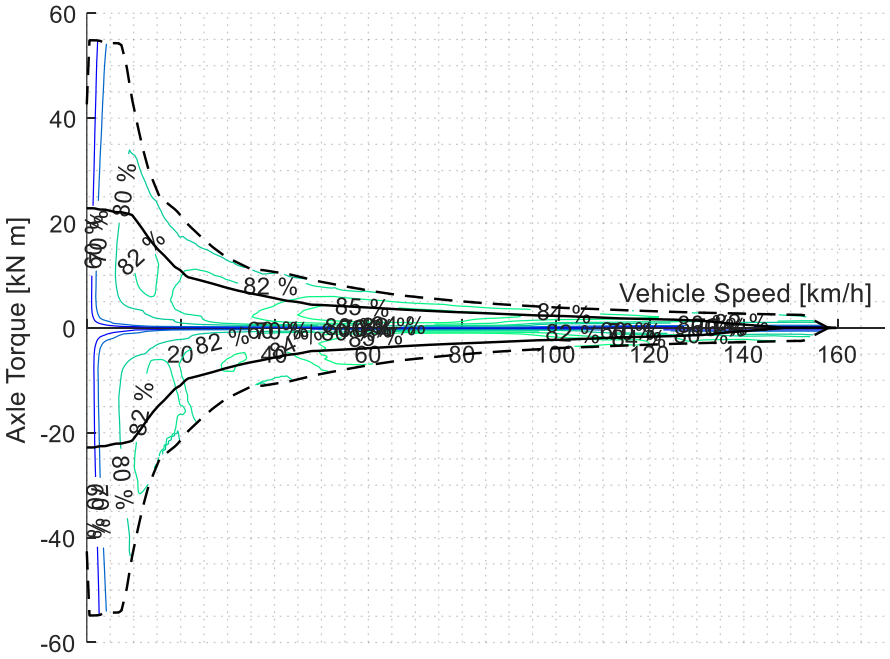



Fig. 4.7. Efficiency-optimized eAxle efficiency map.

### 4.4 eAxle Gear Selection Curves

The first step in creating refined gear selection curves is to specify minimum speeds for engaging second gear and third gear. This prevents higher gears being selected when maximum torque is required. The resulting map is shown in Fig. 4.8.

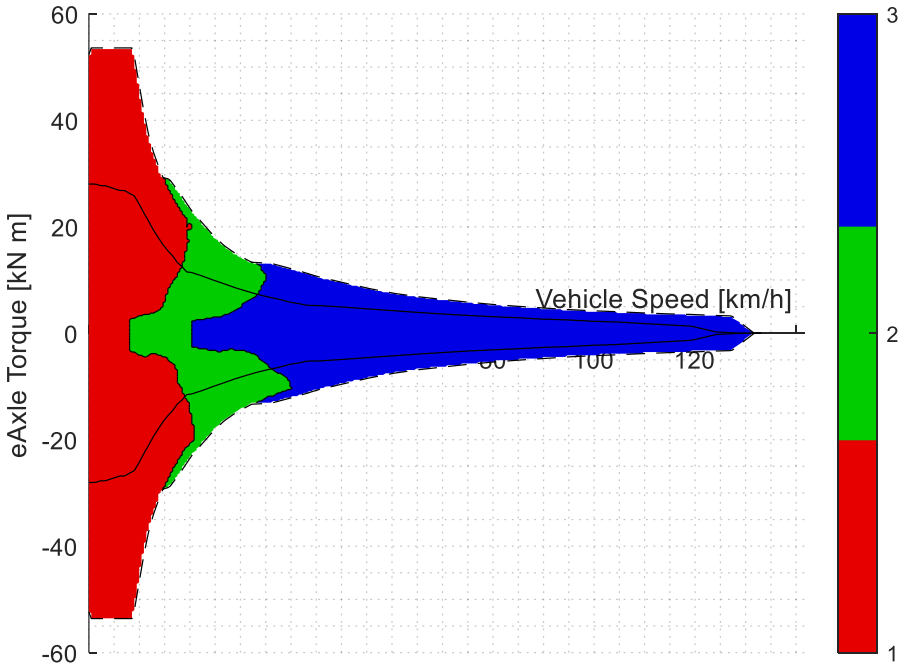



Fig. 4.8. Efficiency-optimized gear shift map with minimum gear speeds (red - first gear, green - second gear, blue - third gear).

Next, the efficiency-optimized gear selection curves were extracted from the map in Fig. 4.8 and modified so that they could be expressed as a function of torque. In Fig. 4.9, each torque value now maps to a unique speed value on each gear change curve. These are shown in Fig. 4.9 along with the eAxle's peak and continuous torque boundary curves for traction and regenerative braking. These curves were used as a basis for designing the efficiency-derived upshift and downshift shown in Fig. 4.10. It should be noted that the upshift and downshift curves and the amount of hysteresis between the curves can be configured based on vehicle requirements and driver preferences.

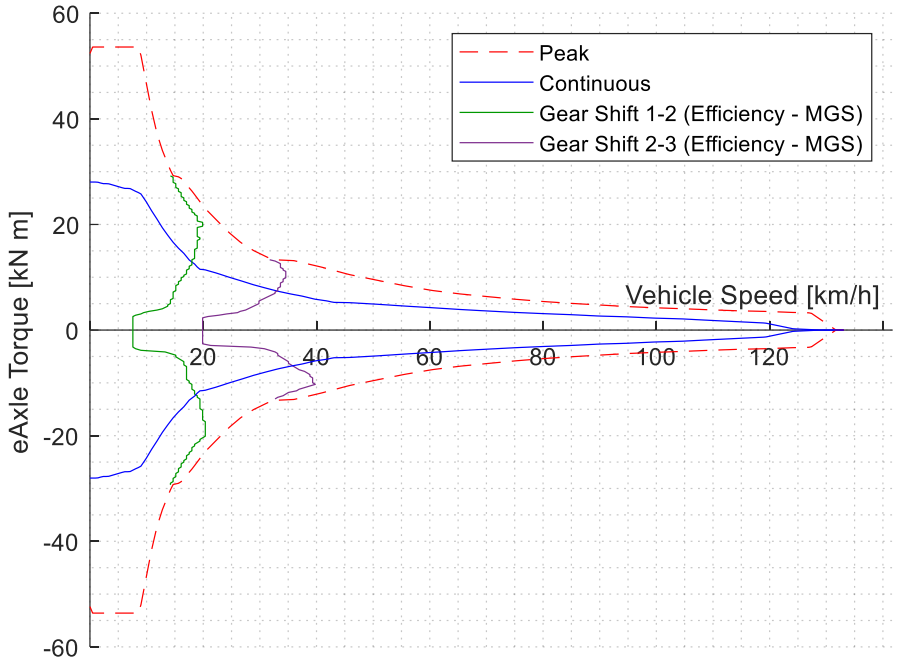



Fig. 4.9. Efficiency-optimized gear-shift curves with minimum gear speeds.

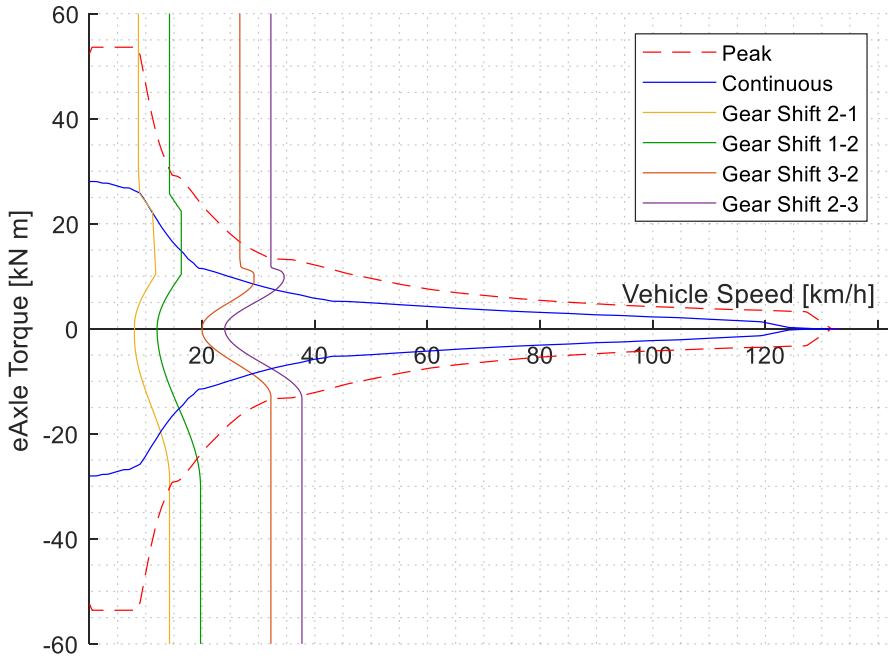



Fig. 4.10. Automatic gear-shifting curves.

The gearshift curves in traction are designed to follow the eAxle's peak torque boundary while accelerating. This is shown in Fig. 4.11 where the upshift curves meet the intersection point between the peak torque boundaries of the two adjacent gears. In other words, the gear shift 1-2 curve, first gear

(peak) curve and second gear (peak) curve in Fig. 4.11 all intersect at the same point. The regen downshift curves are tuned to allow the eAxle follow its peak torque boundary while decelerating. Similarly, the downshift curves intersect the point where the peak torque boundaries of the two adjacent gears they are shifting between meet as shown in Fig. 4.12. In this case, the gear shift 2-1 curve, first gear (peak) curve and second gear (peak) curve share a common intersection point. The maximum upshift speed for each gear change was limited to avoid over speeding the motor and producing excessive back emf. This is particularly important while accelerating in traction.

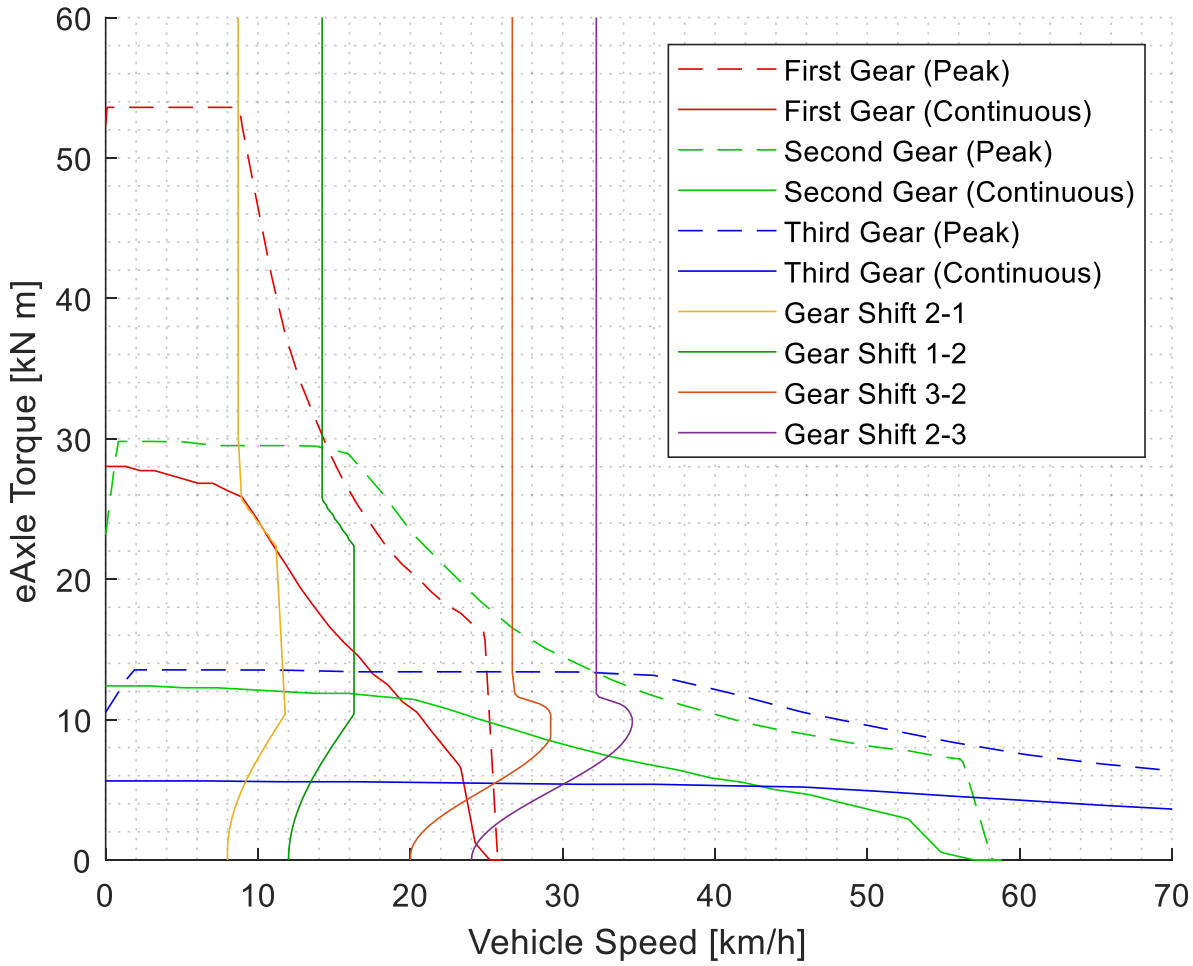



Fig. 4.11. Automatic gear-shifting curves and boundary curves for traction for each gear.

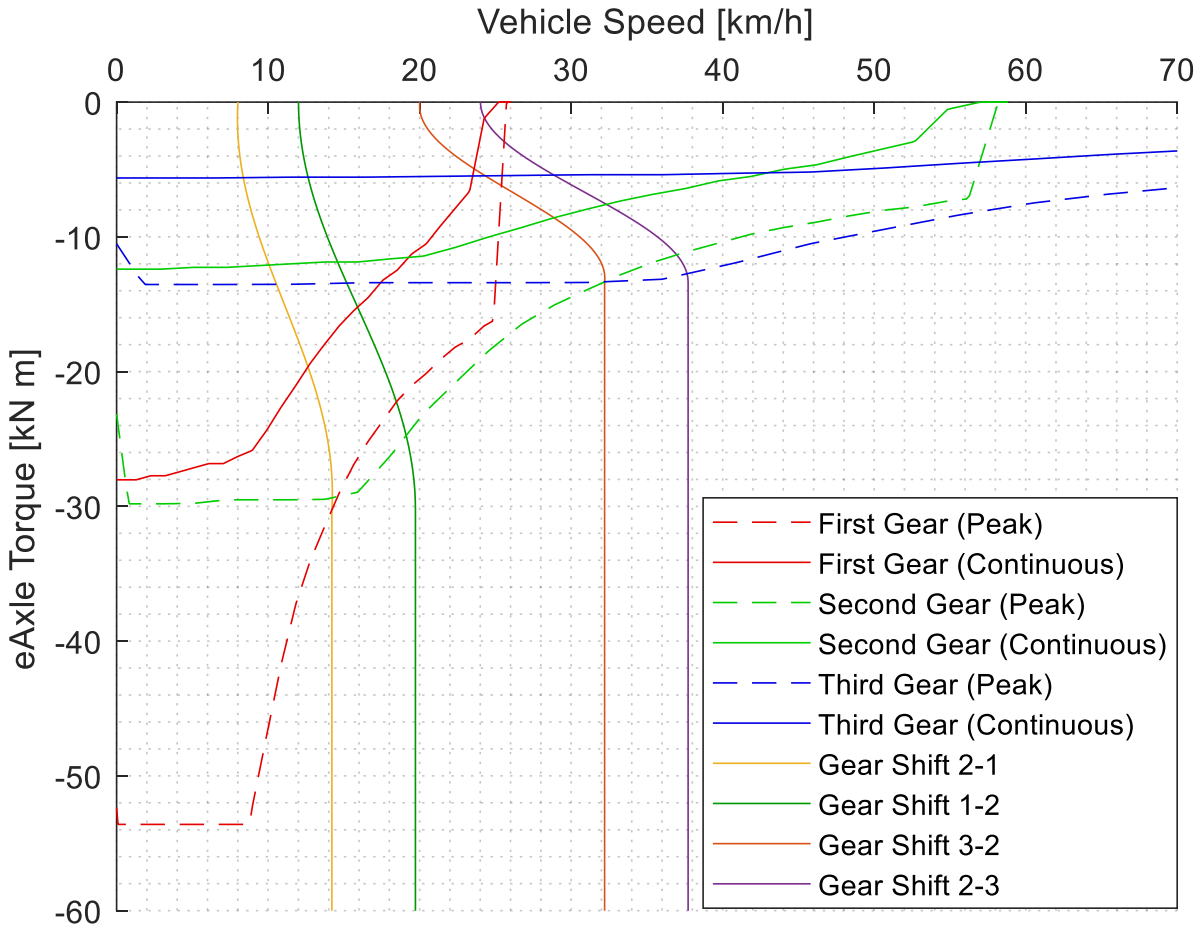



Fig. 4.12. Automatic gear-shifting curves and boundary curves for regenerative braking in each gear.

From a control perspective, it is more convenient to use transmission torque and speed in the gear selection algorithm because the transmission speed sensors can be directly measured with redundancy, and the transmission is closer to the traction machine which makes the torque estimate more accurate in this location compared to estimating torque at the wheels. Fig. 4.13 shows the gear selection curves overlayed on the eAxle transmission's torque-speed map.

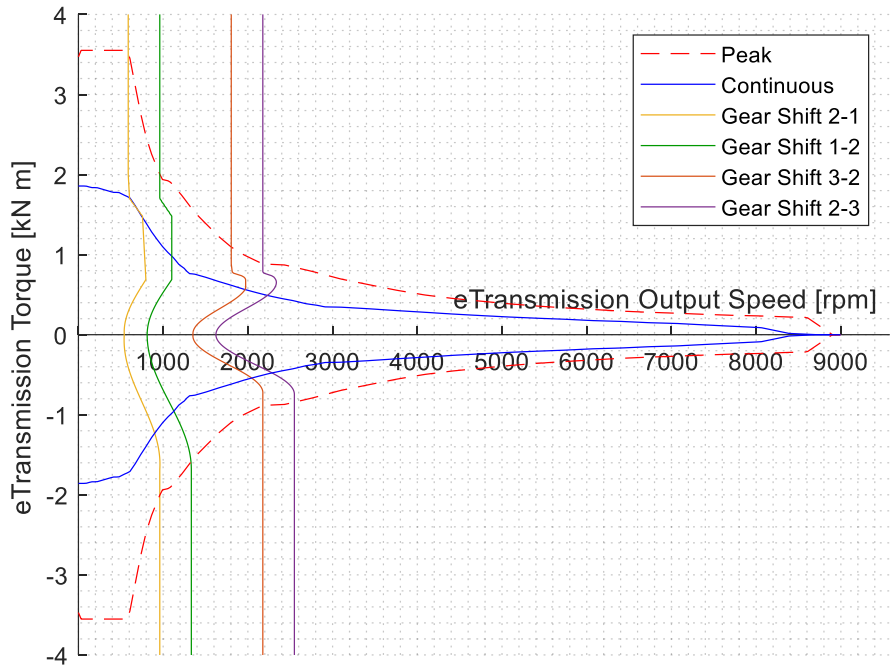



Fig. 4.13. Automatic gear-shifting curves for the eAxle's transmission torque-speed map.

The performance of the efficiency-optimized gear selection map from Fig. 4.5 and the efficiency-derived gear shift curves from Fig. 4.10 are compared in Fig. 4.14. Both gear selection strategies were simulated on a simple acceleration and breaking profile where a vehicle is accelerated to a speed of 25 km/h before cruising with some variation in speed and decelerating to a standstill. The nominal cruising torque-speed operating point coincided with the second to third gear transition on the gear shift curve with no hysteresis in Fig. 4.9. This results in multiple gear change requests as the vehicle's speed varies as shown in the second plot in Fig. 4.14. Once hysteresis is added, the vehicle remains in third gear for the entirety of the cruise segment as can be seen in the third plot in Fig. 4.14.

In addition to gear shift hysteresis, adding debounce to gear selection requests also helps to eliminate unwanted gear change requests. Consider a situation where a vehicle travels over an unexpected bump in the road that causes the driver to unintentionally change their throttle application for a brief period. If this happens at a transmission operating point near a gear selection curve, a gear change would be requested and subsequently cancelled in quick succession, as seen in the first plot in Fig. 4.15. In the second plot in Fig. 4.15, the gear selection request is passed through a debounce filter. This eliminates any gear change request that does not last for the debounce filtering duration, which was set to 200 ms in this example.

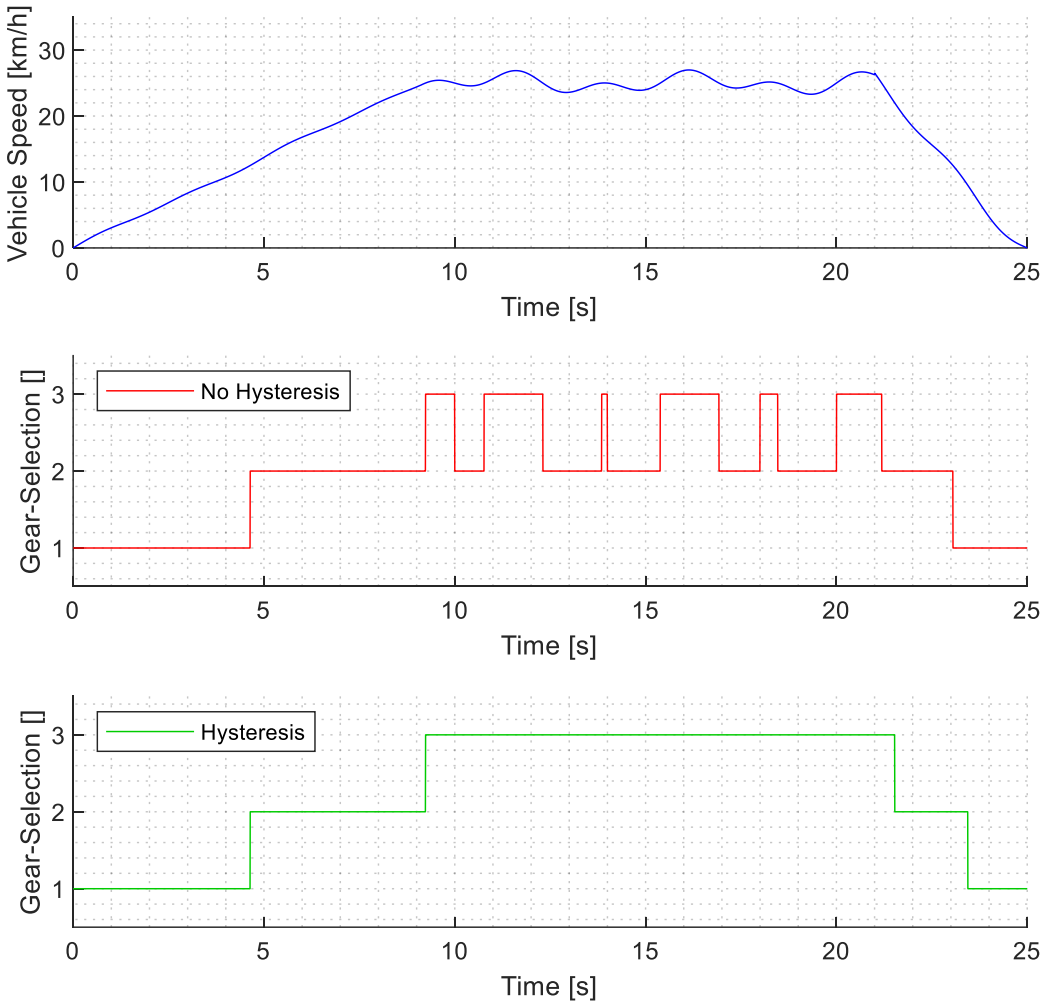



Fig. 4.14. Vehicle speed, gear selection without hysteresis and gear selection with hysteresis vs. time.

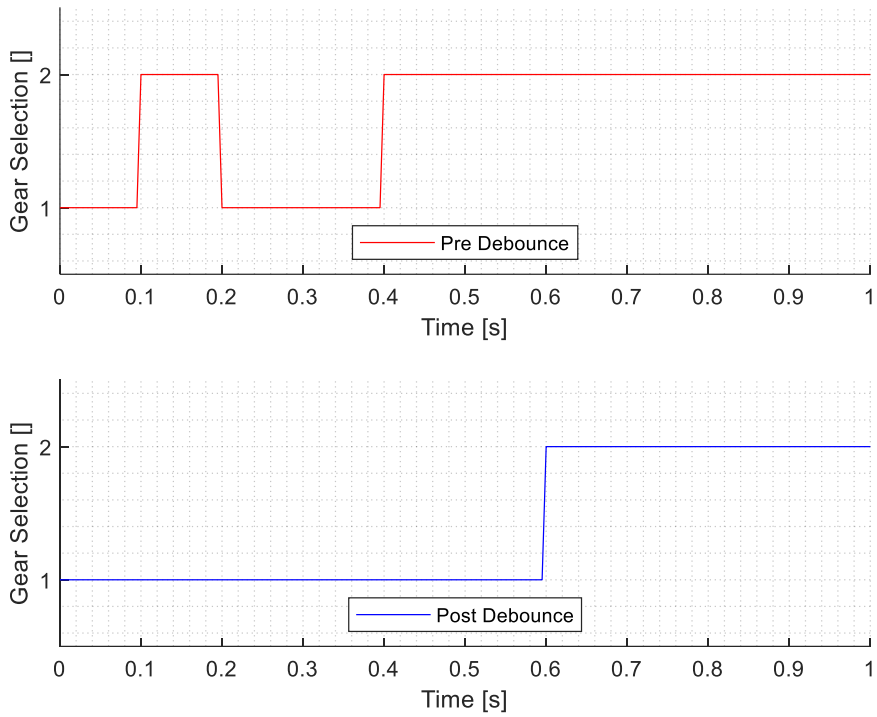



Fig. 4.15. Gear selection debounce filter input and output.

## 4.5 eAxle Testing

### 4.5.1 eAxle Test Setup

The eAxle's gear selection strategy was tested using the same protype hardware and dynamometer apparatus described in Section 2.7.1.

### 4.5.2 Traction and Regenerative Braking Profiles

The durability testing on the eDifferential consisted of several traction and regenerative braking profiles that were run repeatedly until the equivalent work done by the eDifferential was equivalent to its design life. One of these cycles, designed to represent typical on-highway acceleration and braking is shown in Fig. 4.16. During the cycle, the axle accelerated through its three gears (denoted by 1000, 2000, 3000 on the y-axis) in traction and maintained a constant speed in third gear for five seconds before regenerative braking back to zero-speed while downshifting through its gear range. Some speed ripple was added to the half-shaft speeds to ensure that the spider gears within the differential rotated slightly throughout the test. This is the cause of the torque ripple seen on the half-shaft torque outputs. The transmission output torque, transmission output speed and gear selection are shown in Fig. 4.17. During a gear change, the motor must be disconnected from the downstream drivetrain so that it can perform a speed match and synchronize its speed with the transmission input speed required for the new gear.

This results in the temporary torque reductions shown on the plots during gear-shifting. The change in torque polarity during gear shifts is partially due to this speed matching but it is also influenced by the inertia of the eAxle as it loads the dynamometers when its torque source has been removed. Note that for each of these plots the gear selection signal reported by the EACU updates after the new gear has been engaged.

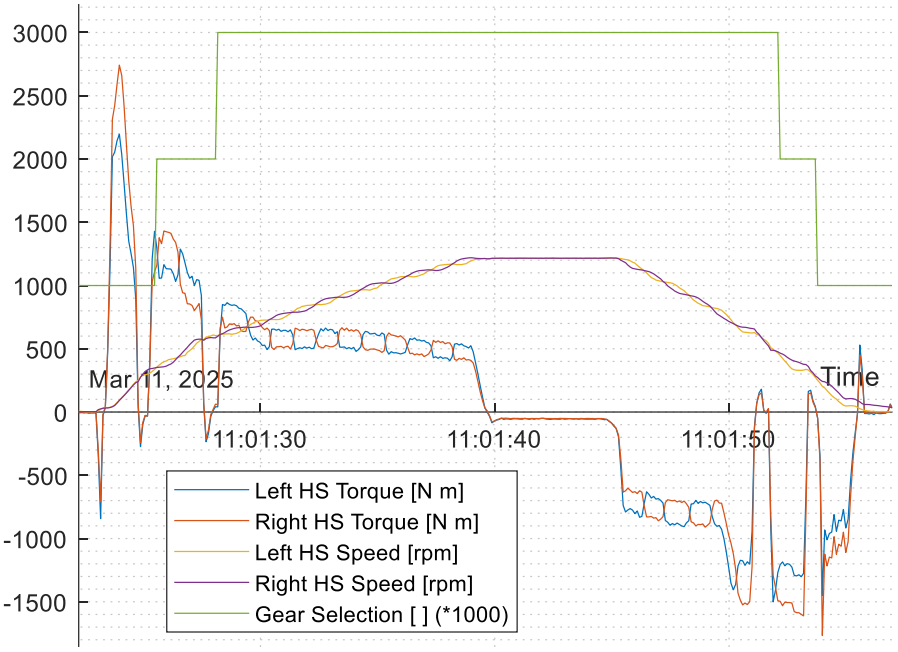



Fig. 4.16. HS torques, HS speeds and gear selection vs. time (hh:mm:ss) for a traction and regenerative braking cycle.

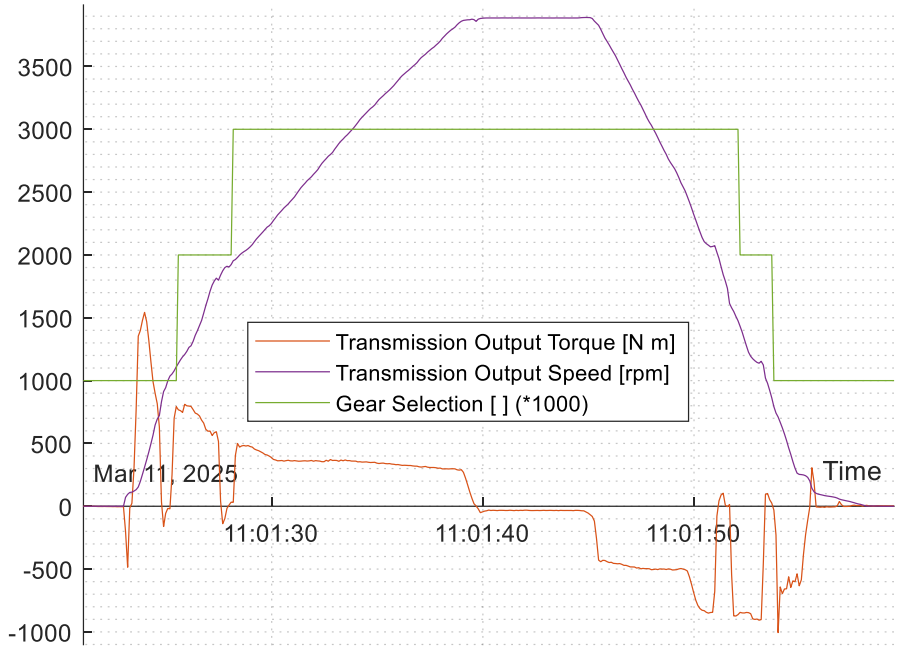



Fig. 4.17. Transmission torque, transmission speed and gear selection vs. time (hh:mm:ss) for a traction and regenerative braking cycle.

### 4.5.3 PEAK ACCELERATION PROFILES

The eAxle is also required to complete a smaller number of more aggressive peak on-highway acceleration cycles. The half-shaft torques, half-shaft speeds and gear selection for this cycle are shown in Fig. 4.18, and the transmission output torque, transmission output speed and gear selection can be seen in Fig. 4.19. While the typical on-highway cycle made use of all three gears when accelerating, this peak cycle starts in second gear. The reasons for this are discussed in Section 1.5.2 and the automatic gear selection strategy using only second and third gear that was discussed in the same section is implemented on the eAxle here. This test validated that the automatic gear selection strategy using only second gear and third gear is optimal for maximum accelerations on low grades. The eDifferential testing successfully verified the gear selection strategies and proved the durability of the clutches, actuators and drivetrain components were suitable for use on the eAxle throughout its design life.

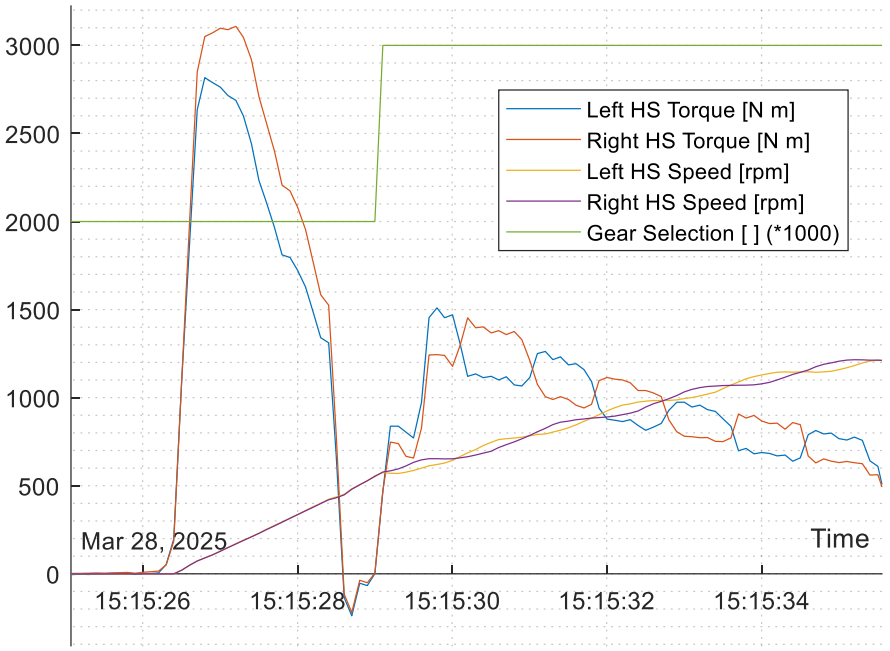



Fig. 4.18. HS torques, HS speeds and gear selection vs. time (hh:mm:ss) for a peak acceleration cycle.

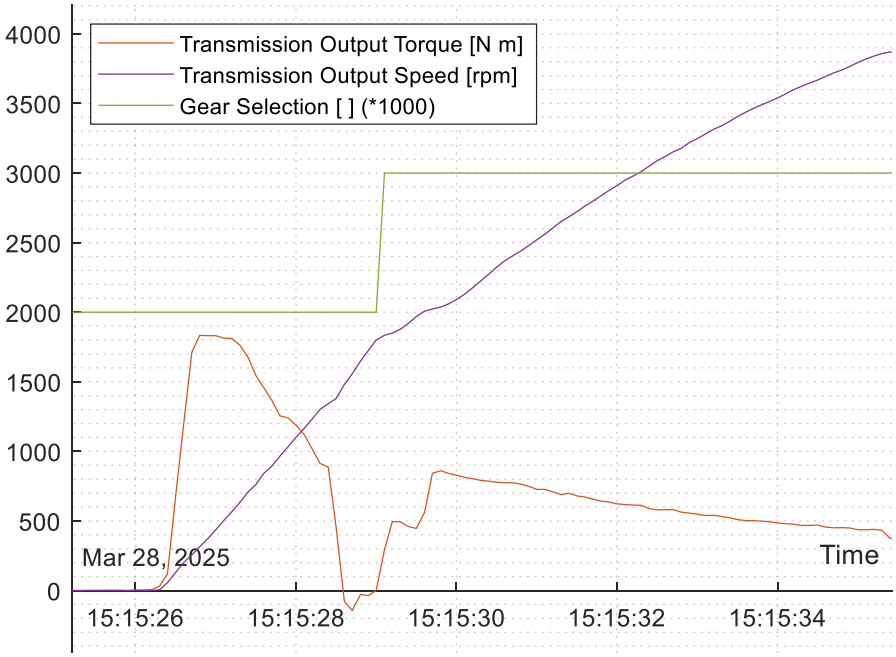



Fig. 4.19. Transmission torque, transmission speed and gear selection vs. time (hh:mm:ss) for a peak acceleration cycle.

## 4.6 CONCLUSIONS

The development of an efficiency-optimized automatic gear selection strategy for a 9-tonne modular heavy-duty eAxle was discussed in this chapter. Raw power loss data for an inverter and motor system

was post-processed for usability and combined with the eAxle's drivetrain efficiency to produce power loss and efficiency maps for each gear. The per-gear efficiency maps were interpolated onto a common set of lookup vectors which allowed the most efficient gear for each operating point to be selected. While it is optimal from an efficiency perspective, the resulting gear selection map was not suitable for direct application in vehicles. Efficiency-derived upshift and downshift gear selection curves are developed to overcome this issue. Both gear selection strategies are compared in simulation. The performance of the automatic gear selection curves and the durability of the eDifferential's components are verified by a dynamometer testing program consisting of several acceleration and regenerative braking cycles.

The eAxle is in use on prototype vehicles in varying applications, allowing the performance of the automatic gear selection strategy to be evaluated in the field. Future work will include tuning of the upshift and downshift curves to suit the vehicle application. Further characterization of the efficiency of the inverter and motor system along with the eAxle drivetrain is also of interest. This could be achieved by adding a third torque meter to the dynamometer test setup between the motor output and the transmission input. This would allow a more accurate measurement of motor power for use in power loss and efficiency calculations

# 5 CONTROL OF DRIVELINES WITH MULTIPLE ELECTRIFIED AXLES

## 5.1 ABSTRACT

This chapter describes the main algorithms implemented on a Driveline Control Unit (DCU) fitted on a hybrid or electric vehicle with multiple eAxles. The DCU is configurable for vehicle drivelines with 2, 3 or 4 eAxles and acts as an interface between a vehicle integrator's Vehicle Control Unit (VCU) and the eAxle Control Units (EACUs). Some key DCU features include speed measurement, wheel-slip calculation, available torque calculation, torque vectoring, wheel-slip limitation, driveline efficiency optimization, gear selection, staggered gear-shifting, differential lock actuation and the management of driveline functional safety. The DCU provides additional benefits to vehicle integrators, including reducing the VCU CAN bus requirements and allowing the VCU to maintain a conventional torque control algorithm focused on vehicle-level torques.

The vehicle control architecture is discussed in Section 5.2. The speed calculation algorithm is described in Section 5.3. Section 5.4 discusses the available-torque calculation algorithm. The torque vectoring algorithm is described in Section 5.5. The gear selection algorithm is discussed in Section 5.6. An overview of the DCU test setup is given in Section 5.7. The chapter is concluded in Section 5.8.

The work in this chapter has been published as follows:

- C. Healy and J. G. Hayes, "Speed vectoring algorithms for drivelines with multiple modular e-axles", *International Scientific Conference on Electric Power Engineering (EPE)*, 2024 [45].

## 5.2 VEHICLE CONTROL ARCHITECTURE

From a high-level view, the vehicle uses a four-tier control system with a vehicle control unit (VCU) sitting on top of a driveline control unit (DCU) that communicates with the eAxle control unit (EACU) in each axle which in turn communicates with the motor control unit (MCU) within each eAxle's inverter. The Controller Area Network (CAN) communication protocol is used [46] and the DCU uses the Society of Automotive Engineers (SAE) J1939 format [47]. A computer-aided design (CAD) rendering of an 8x8 driveline, complete with the DCU and eAxles, is shown in Fig. 5.1 [5]. A high-level block diagram of the vehicle control architecture can be seen in Fig. 5.2. As this is a control focused chapter, only control signals and connectors are shown.

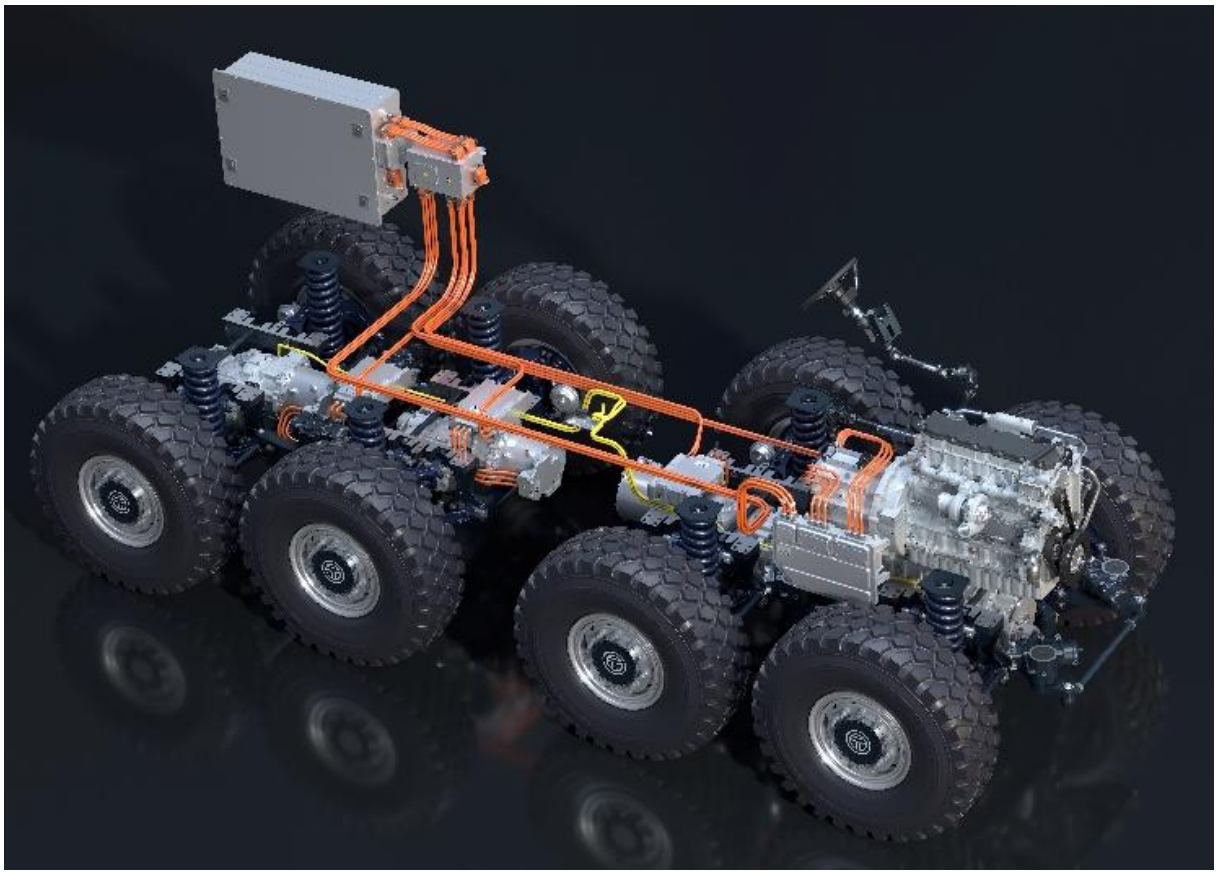


Fig. 5.1. A CAD rendering of an 8x8 series-hybrid driveline.

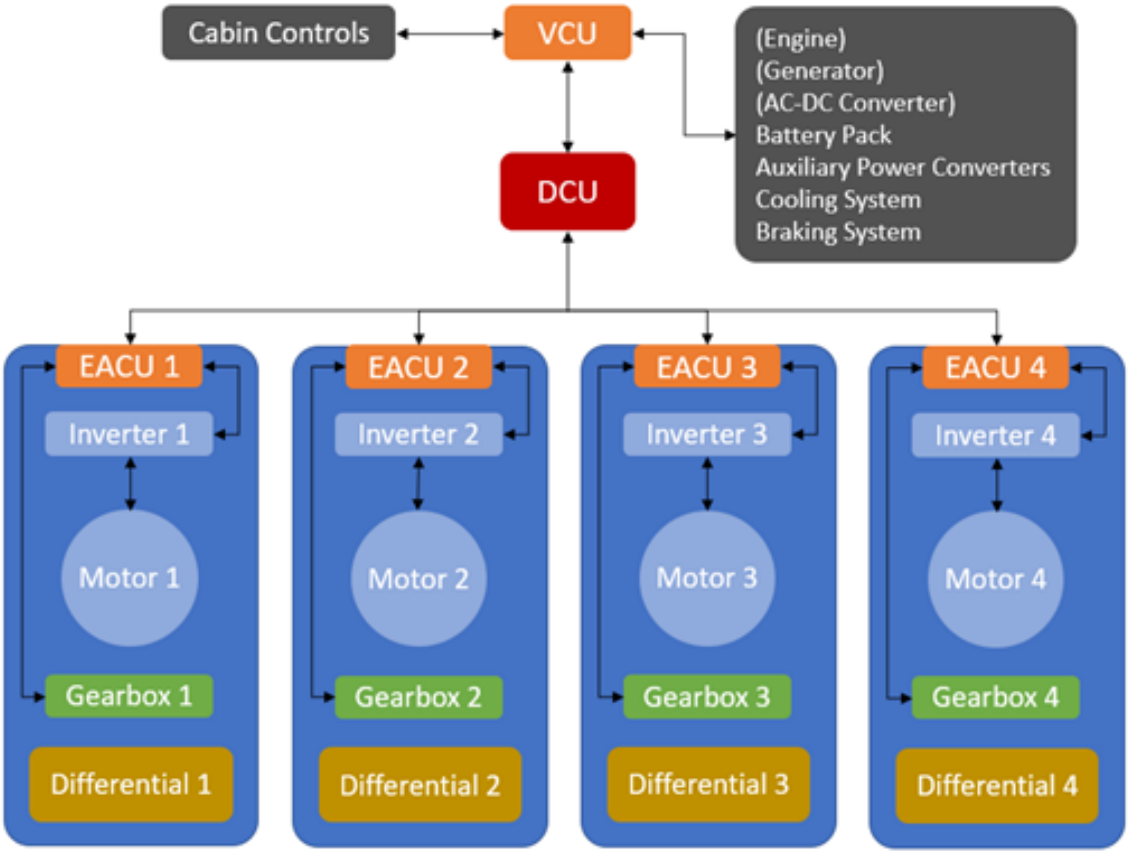



Fig. 5.2. High-level vehicle control architecture for an 8x8 vehicle.

The VCU takes instructions from the cabin controls and is responsible for controlling the vehicle-level systems. Many heavy-vehicle companies are using series-hybrid powertrains that require an engine, generator, and AC-DC converter in addition to the battery pack, auxiliary power converters and cooling and braking systems. For heavy-duty battery-electric vehicles, such as airport fire trucks, the engine, generator, and AC-DC converter are not required.

Each eAxle has an EACU that is responsible for controlling the inverter, motor, three-speed transmission, a CAN-controlled oil pump and differential lock.

The DCU acts as an interface between the VCU and the EACUs. The VCU sends total vehicle requirements and the DCU vectors these into per-axle requirements using a torque-vectoring algorithm. The DCU can measure up to 8 wheel speed sensors simultaneously, thus, enabling the speed of each wheel on an 8x8 vehicle to be directly measured. This avoids CAN latency and improves reaction times to wheel-slip and wheel-lock events when torque vectoring. The DCU combines the per-axle outputs from the EACUs into vehicle-level signals and sends them to the VCU to close the vehicle-level torque control loop. This allows a conventional torque control loop to be used on the VCU. The DCU hardware has six CAN buses allowing dedicated connections for a diagnostic and programming port in the cabin, the VCU and four eAxles.

From a functional safety perspective, the driveline control system has been designed with ISO 26262 [48] automotive safety integrity level C (ASIL-C) intent. This is enabled by several hardware and software features on the controllers. First, a dual processor architecture is used on the DCU and EACUs that enables all sensor readings, CAN end-to-end verifications and algorithm calculations to be performed on both processers before completing a plausibility analysis to verify that both processors' results are the same. The dual processor architecture also allows the system to bring itself to a fail-safe state in the event of any single-point processor failure. In addition, the driveline control system features redundant emergency-stop inputs (both hardwired and CAN based), redundant ignition/KL15 inputs, redundant speed sensors that enable plausibility analysis to be performed on all speed measurements, end-to-end protection on all CAN signals and memory protection algorithms built into the controllers. Furthermore, each EACU is configured with a unique source address so that any mismatching of axles in the wiring harness will result in CAN timeout faults and zero torque capability. The DCU, EACU and inverter each have independent motor-overspeed protection mechanisms to protect against excessive back emf.

## 5.3 SPEED CALCULATION ALGORITHM

The purpose of the DCU's speed calculation algorithm is to estimate the nominal wheel speeds of each axle in the driveline based on the vehicle's steering input, steering mode and driveline geometry. The inputs to the speed calculation algorithm are the steering angle, steering mode, wheel speeds and driveline geometry. The steering angle can be measured at the steering column or on the pitman arms. When a steering column sensor is used, the steering gear ratio must be used to calculate the pitman arm angles from the steering wheel angle. The DCU has the capability to store steering geometry matrices for 4x4, 6x6 and 8x8 vehicles. Vehicles fitted with the DCU may use any combination of several steering modes including front single-axle steering (FSAS), front twin-axle steering (FTAS), rear twin-axle steering (RTAS), crab steering (CBS), pivot steering (PTS) and all-wheel-steering (AWS).

One of the main limiting factors on the minimum turning radius in a vehicle is the front axle back-lock angle ($\delta_{BL}$) on the inside wheel making the turn. The upper limit on the back-lock angle is dependent on several factors including steering arm, suspension and hull geometry. If pneumatic brake callipers are used, the brake chambers can also limit back-lock angles. Typically, it is not possible to mount spring applied pneumatic-release parking-brake chambers on steered axles due to interference issues, particularly when axial brake callipers are fitted. Radial callipers typically produce less interference but ultimately still cause a back-lock angle limitation. The maximum front back-lock angle is typically in the region of 34 ° to 36 °. A high-level diagram showing the front back-lock angle can be seen in Fig. 5.3.

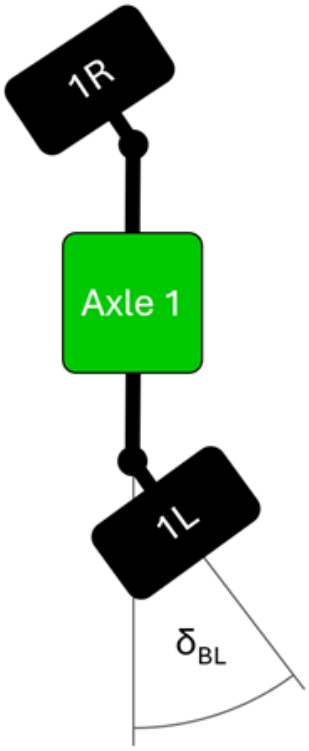



Fig. 5.3. Front axle back-lock angle.

A diagram of a 6x6 vehicle with front twin-axle Ackermann steering [49] completing a turn is shown in Fig. 5.4. Looking at this figure, the axles are numbered 1, 2 and 3 from front to rear respectively. The motor speeds on each axle are proportional to the average of the axle's wheel speeds. The motor speed on axle 1 is the average of the speeds of wheel 1L and wheel 1R, this is not the same as the motor speed on axle 2 which is the average of the speeds of wheel 2L and wheel 2R and so on. Once the vehicle's wheelbases ($W_{B1\text{-}2}$ and $W_{B2\text{-}3}$), trackwidth ($W_{T1}$) and knuckle-to-knuckle distance ($W_{K1}$) are known, a steering geometry matrix can be constructed to calculate the wheel and axle speeds for a given steering input.

There are three significant turning radii that should be noted. The normal radius ($r_N$) is the perpendicular distance from the chassis centreline of the vehicle to the centre of rotation and is used for calculating the normalized turning radius of each wheel and the normalized wheel and axle speeds. The radius at which the vehicles centre of gravity (CoG) rotates about the centre of rotation ($r_{CoG}$) is the radius that should be used for centripetal force calculations. Note that where the points of intersection between $r_N$ and $r_{CoG}$ with the chassis centreline differ, the centripetal force vector can be divided into longitudinal and lateral components to calculate the weight transfer during cornering. Finally, the vehicle turning radius ($r_T$) is the radius at which the outermost point of the vehicle rotates about the centre of rotation. The sign convention used in the model is that positive steering inputs result in counterclockwise (CCW)

rotation and negative steering inputs result in clockwise (CW) rotation. The turning radii are signed positive for CCW turns and negative for CW turns.

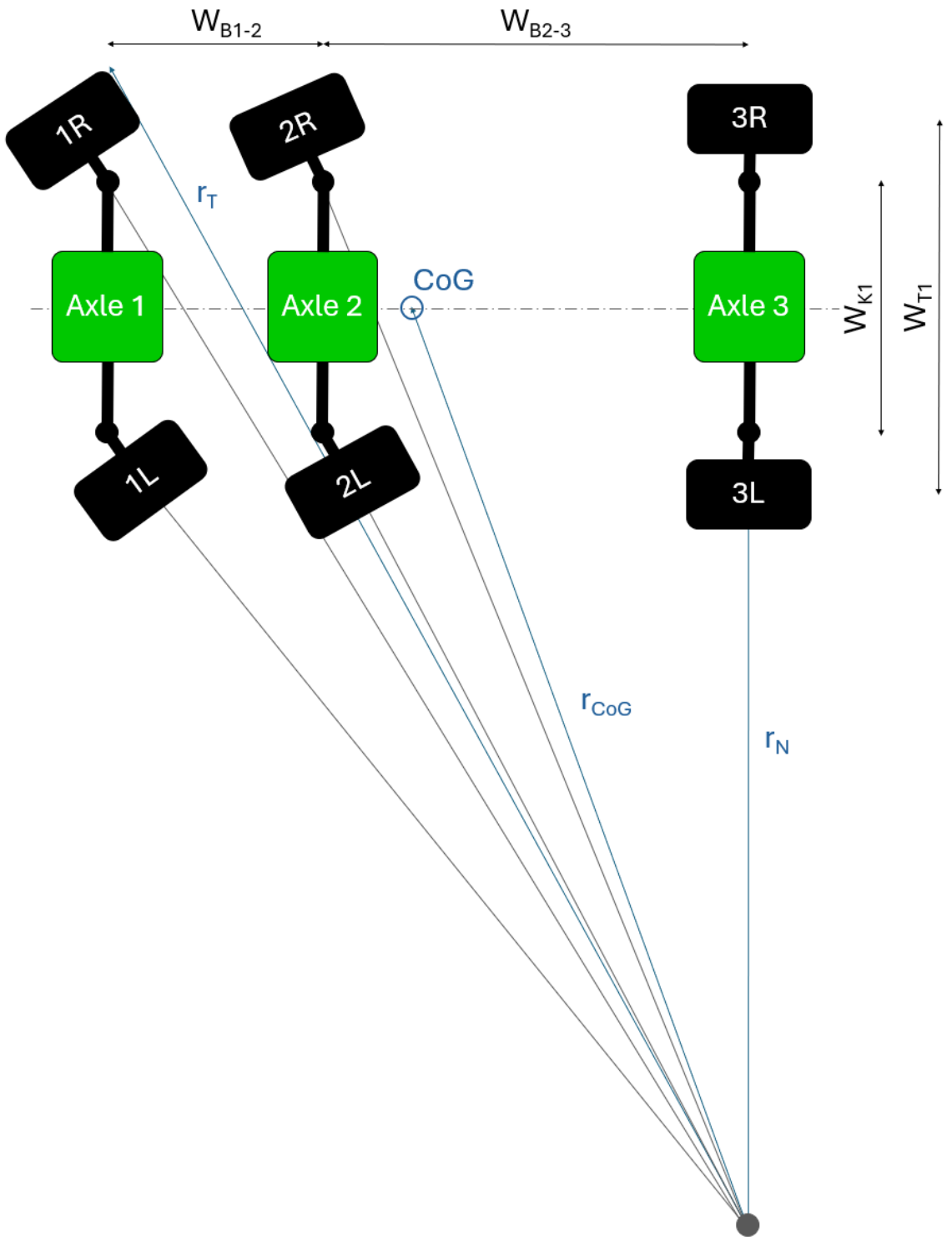



Fig. 5.4. A 6x6 vehicle with front twin-axle Ackermann steering completing a turn.

The three turning radii for this steering configuration are plotted against the front axle back-lock angle in Fig. 5.5. Normalized wheel speeds for each axle are plotted against normal turning radius in Fig. 5.6 and normalized axle speeds are plotted against normal turning radius in Fig. 5.7.

The AWS configuration allows for a minimum vehicle turning radius ($r_T$) of 8.64 m. At a 10 m normal turning radius, the normalized wheel speeds vary from approximately 0.875 to 1.190 and the normalized axle speeds vary from approximately 1.028 to 1.074.

It should be noted that the turning radii are all infinite when the front back-lock angle is 0 ° and all normalized wheel and axle speeds approach 1 as the turning radius tends towards infinity.

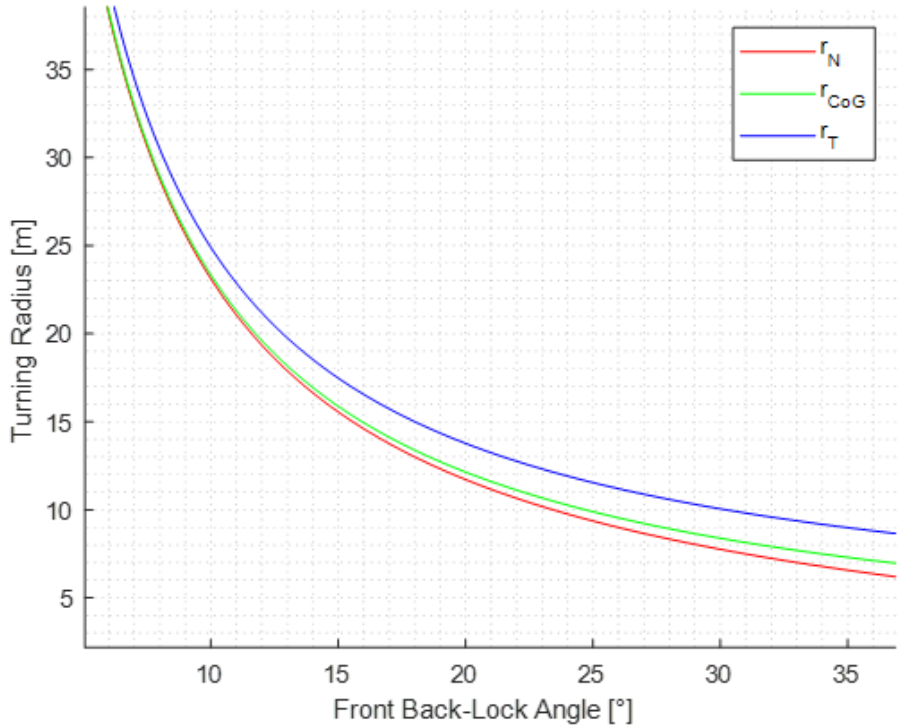



Fig. 5.5. Notable turning radii vs. front axle back-lock for a 6x6 vehicle with FTAS.

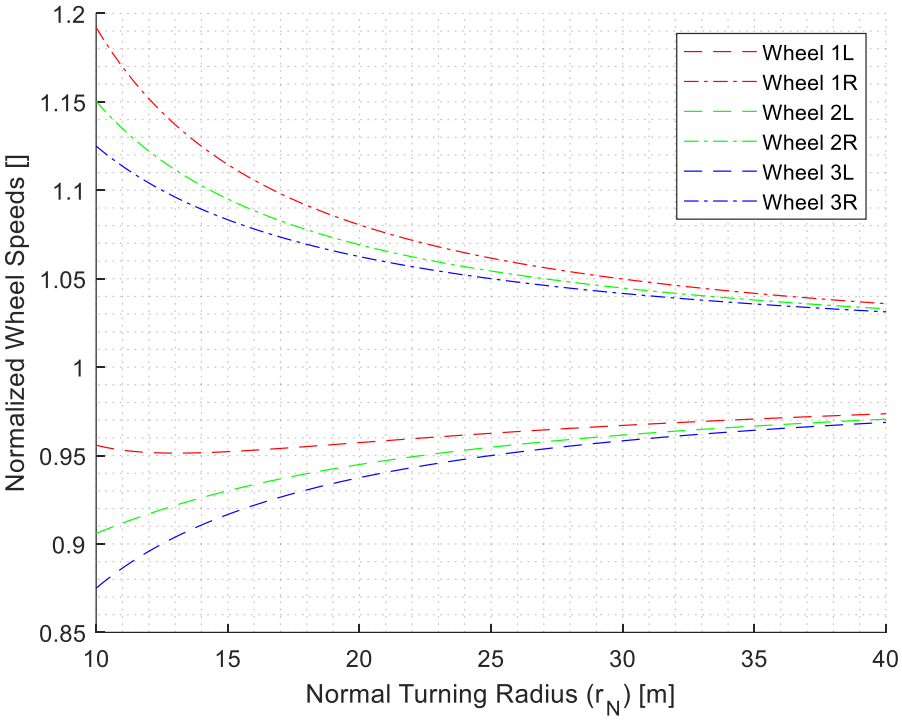



Fig. 5.6. Normalized wheel speeds vs. turning radius for a 6x6 vehicle with FTAS.

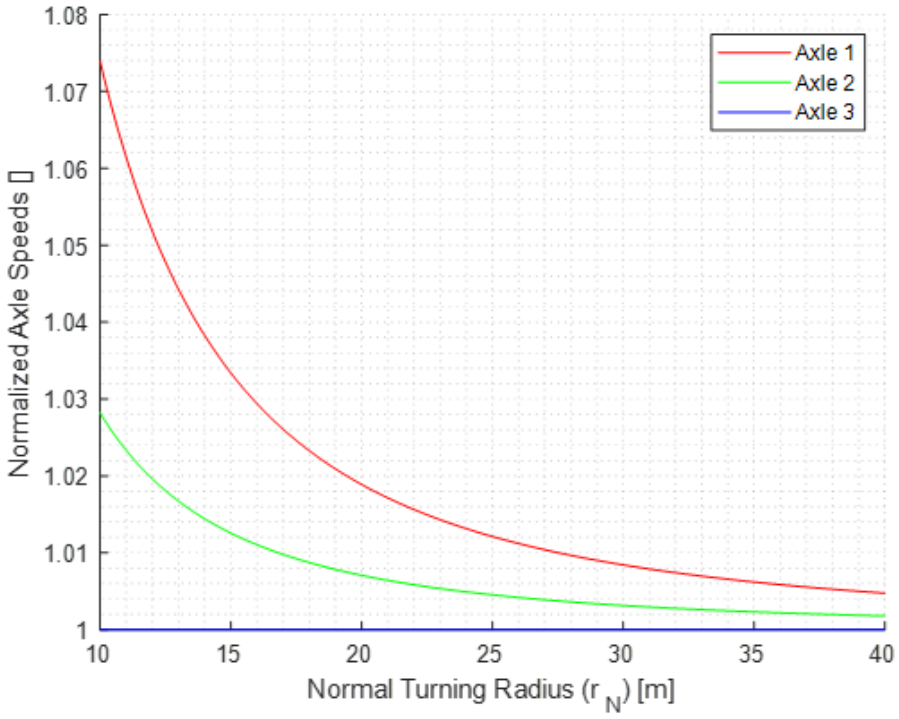



Fig. 5.7. Normalized axle speeds vs. turning radius for a 6x6 vehicle with FTAS.

Once the normalized wheel speeds for each axle are known, the speed calculation algorithm can divide the DCU's wheel speed measurements by the product of the normalized wheel speed and the vehicle

reference speed to determine the wheel-slip at each wheel. In situations where wheel-slip or wheel-lock are excessive, the available torque calculation algorithm, discussed in Section 5.4 applies a torque derating until the wheel speeds return to an acceptable value.

## 5.4 AVAILABLE TORQUE CALCULATION ALGORITHM

The purpose of the DCU's available torque calculation algorithm is to determine the maximum torque that can be produced by each eAxle without causing excessive wheel-slip or wheel-lock. The available torques are used to set limits on the amount of traction and regen torque that can be requested of each axle by the torque vectoring algorithm. The primary inputs for this algorithm are the available axle and motor torques reported by the EACUs, the wheel speed measurements and wheel-slip ratios of each wheel on the vehicle, axle torque limits from the VCU and a vehicle speed limit from the VCU. The emergency stop input and diagnostic trouble codes (DTCs) are continuously monitored by the algorithm. A preconfigured torque derating curve is used where excessive wheel-slip or excessive wheel-lock are detected. In situations such as front axle lift-off when cresting a steep grade climb where wheel-slip can be particularly excessive, the DCU can command a small amount of regenerative braking torque to decelerate the eAxle until its wheel speeds are back in-line with other eAxles on the vehicle. The available torque calculation algorithm also monitors component temperatures and can limit available torque to prevent thermal runaway.

When the vehicle is fitted with an inertial measurement unit (IMU), additional inputs, including three-axis accelerations, chassis pitch, chassis roll, and vehicle yaw rate, are available. These can be used to add a predictive element to the available torque calculation by estimating the relative weight distribution of each axle and wheel station. This is done using the gradient and acceleration-based weight transfer calculations discussed in Section 2.3. The predictive available torque calculations also include estimates of the slip-limiting friction coefficient between the vehicle's tyre and the road. Thes are stored on the DCU for the different cabin selected road surfaces and central-tyre-inflation-system (CTIS) tyre pressure settings along with the turning radius is taken from the speed calculation algorithm which allows the weight distribution calculation to consider the impact of centripetal force on vehicle weight distribution and its implications on available torque.

## 5.5 TORQUE VECTORING ALGORITHM

The torque vectoring algorithm is used to calculate the optimum torque distribution between a vehicle's eAxles. The calculation is based on the vehicle's weight transfer to avoid wheel-slip and driveline efficiency optimization to minimise the power losses at a given operating point.

The inputs to the torque vectoring algorithm are the driveline torque command, the eAxle speeds from the speed calculation algorithm, the available torques from the available torque calculation algorithm along with the vehicle-level battery-management-system (BMS) limits for battery charging and discharging currents. The efficiency-optimized torque vectoring algorithm uses the inverter and motor's power loss and efficiency data, as presented in Section 4.2, to calculate the most efficient (minimum power loss) operating point for a given vehicle-level torque and speed. Torque ramp-rate limits are also included. These limits protect the powertrain components and are at their lowest when the torque polarity is changing.

Fig. 5.8 shows the eAxle torques and chassis pitch of a 4x4 vehicle as it transitions from a flat surface to a 60 % grade climb. As the grade increases and the vehicle weight transfers rearward, wheel-slip limitations mandate that torque be vectored from the front axle to the rear axle to avoid excessive wheel-slip. Note that the chassis pitch reaches a maximum value that is equivalent to a 72 % grade due to compression of the rear suspension.

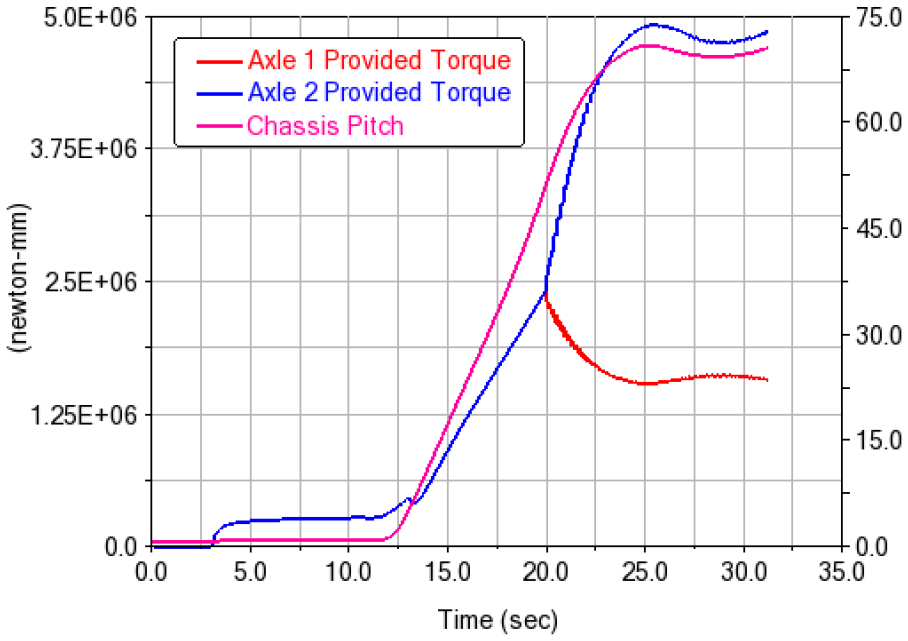



Fig. 5.8. eAxle torques and chassis pitch of a 4x4 vehicle completing a grade climb.

## 5.6 GEAR SELECTION ALGORITHM

The DCU's gear selection algorithm implements the upshift and downshift gear selection curves described in Section 4.4. It should be noted that each is checked independently, so in some situations, such as torque vectoring where axle torques differ or cornering where axle speeds differ, different axles

may be in different gears. The amount of gear-shift hysteresis can be configured to suit customer preferences and typically increases as torque increases.

For drivelines with multiple eAxles, the staggered gear-shifting algorithm takes the gear selection requests from the gear selection algorithm and staggers when they are sent to the eAxles to maintain continuous torque delivery to the road. The staggered gear-shifting algorithm uses recursive counters to determine which axles have been shifted least recently. When multiple gear-selection request changes occur simultaneously, the axle that has changed gear least recently is shifted first, and so on.

To make the shifting as smooth as possible, the eAxles that are not completing a gear shift will increase their torque output to compensate for the torque that the eAxle being shifted was producing and to overcome the negative torque produced by torque mirroring where the speed matching the traction machine's speed with the new gear causes the output torque of the eAxle completing a gear shift to become negative during a gear shift as discussed in Section 4.5.2. A torque reduction state machine is used to control the torque ramp-down before a gear shift, sending the new gear selection request to the EACU, waiting for the EACU to report that the gear shift has been completed and the torque ramp-up back to the desired torque request. Note that the DCU waits until torque ramp-down is completed before sending the gear selection request to the EACU. This will be discussed in more detail during the commentary on Fig. 5.15 in Section 5.7. The concept of staggered gear-shifting for an 8x8 vehicle is illustrated graphically in Fig. 5.9.




Fig. 5.9. Staggered gear shifts for an 8x8 vehicle.

It is essential to avoid any risk of over speeding the motor on the last axle to be shifted, as this can result in excessive back emf and can cause irreparable damage to the powertrain. The time between each gear shift is reduced as the vehicle's acceleration increases. The maximum delay between shifts is approximately 500 ms and the minimum delay can be as low as 0 ms. This is more than adequate to allow for one eAxle to ramp-down torque, complete its gear shift and ramp up torque before the next eAxle is requested to change gear. The staggered gear selection algorithm is bypassed during

emergency-stop (E-STOP) situations or when 0 N m of driveline torque is requested by the VCU. Fig. 5.10 shows a simulation of staggered gear selection on an 8x8 vehicle with 500 ms between each gear shift.

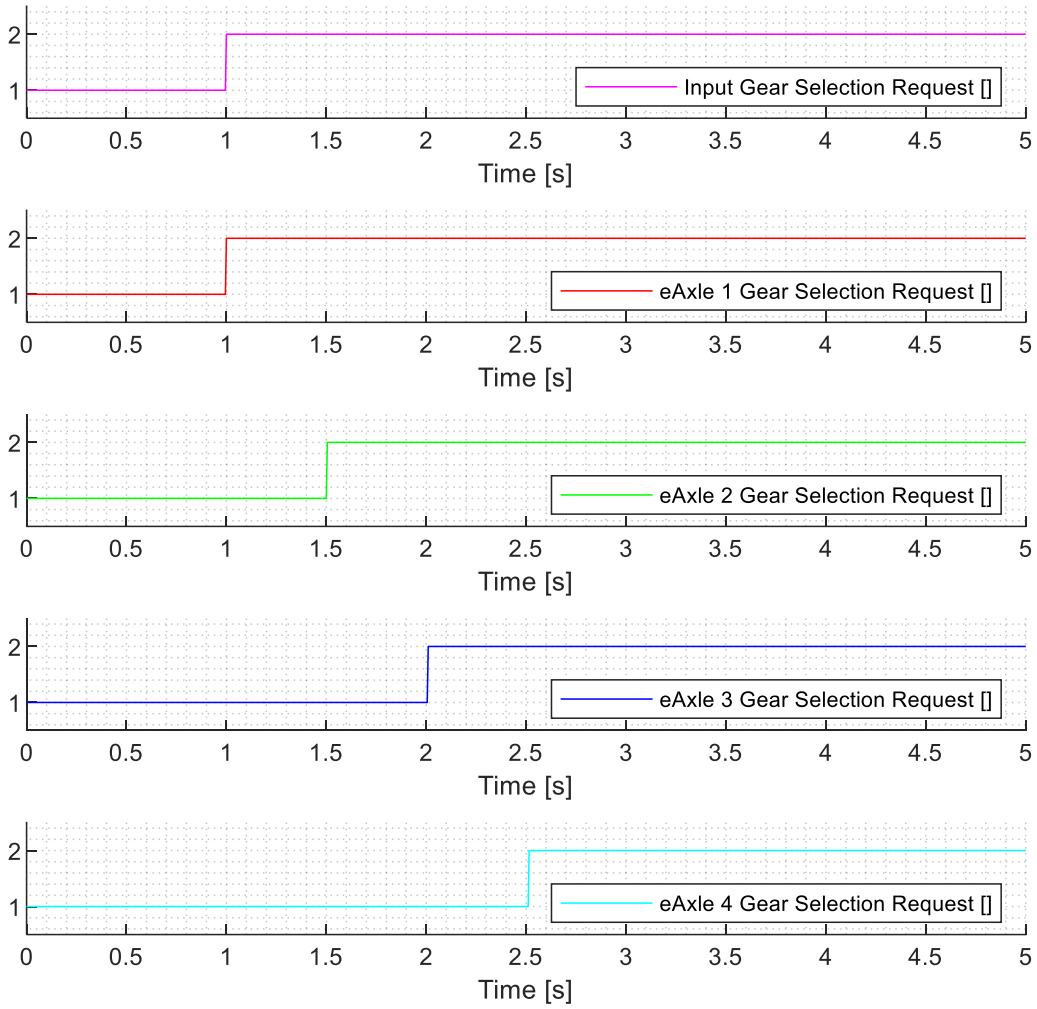



Fig. 5.10. Staggered gear selection on an 8x8 vehicle with 500 ms between shifts for an 8x8 vehicle.

An 8x8 vehicle's simulated speed vs. time curves during maximum accelerations using the eAxles' peak and continuous performance, first without and then with staggered gear-shifting are shown in Fig. 5.11 and Fig. 5.12. In Fig. 5.11, all eAxles were shifted simultaneously resulting in a temporary plateau in the vehicle's speed vs. time curve corresponding to zero-acceleration. In Fig. 5.12, the gearshifts on the 8x8 are staggered with 500 ms between shifts meaning that the vehicle is always propelled by at least three eAxles. This results in a significantly smoother experience for the occupants and improves vehicle stability. Note that the benefits of staggered gear-shifting become more pronounced as the number of axles increases. The reason for this is that for a 4x4 vehicle, 1/2 of the vehicle's total torque

capability can be used during a gear shift. This increases to 2/3 of the torque capability for a 6x6 and ¾ of the torque capability for an 8x8.

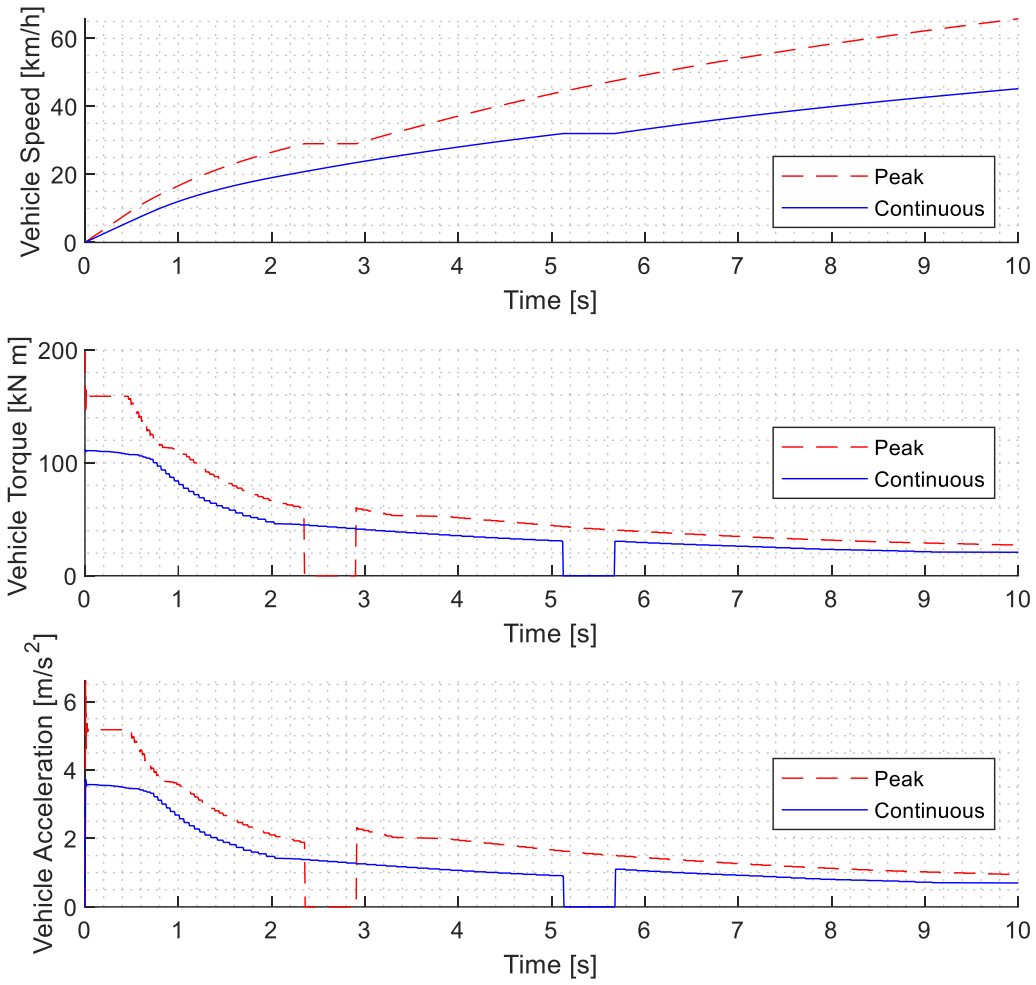



Fig. 5.11. Vehicle acceleration simulation without staggered gear-shifting for an 8x8 vehicle.

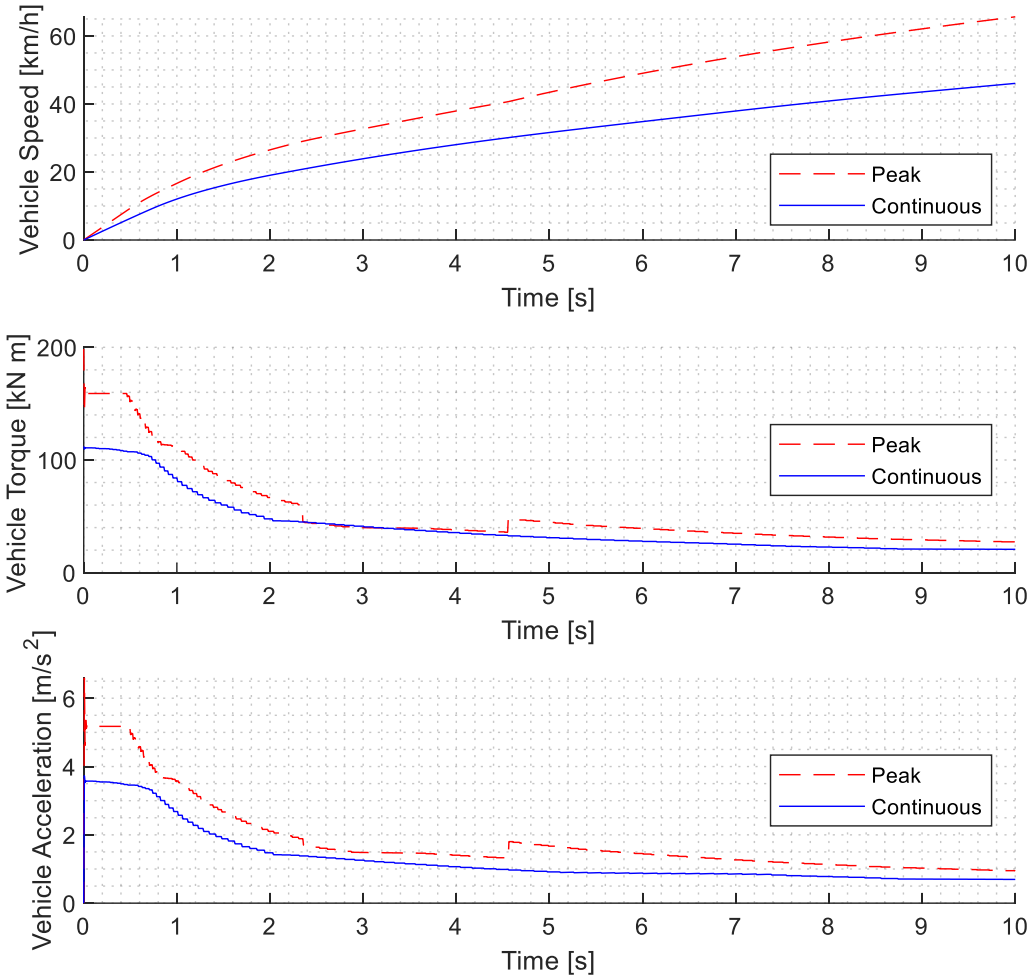



Fig. 5.12. Vehicle accleration simulation with staggered gear shifting for an 8x8 vehicle.

## 5.7 DRIVELINE CONTROL UNIT TESTING

### 5.7.1 SOFTWARE-IN-THE-LOOP TESTING

Throughout its development, the DCU was tested using a combination of MATLAB, Simulink, Adams Car, and USB to CAN interfaces. MATLAB was used to emulate the VCU and EACUs while the vehicle plant models for various 4x4, 6x6 and 8x8 vehicles were modelled in Adams Car. Simulink was used to facilitate the co-simulation interface between MATLAB and Adams. The test setup allowed for verification of the emergency stop functionality, characterization of the algorithms' performance, optimization of the lookup tables and fault injection testing. A high-level diagram of the DCU development and validation framework is shown in Fig. 5.13. The Simulink model from the development and validation framework in Fig. 5.13 is shown in Fig. 5.14. An acceleration test for an 8x8 vehicle fitted with the DCU is shown in Fig. 5.15.

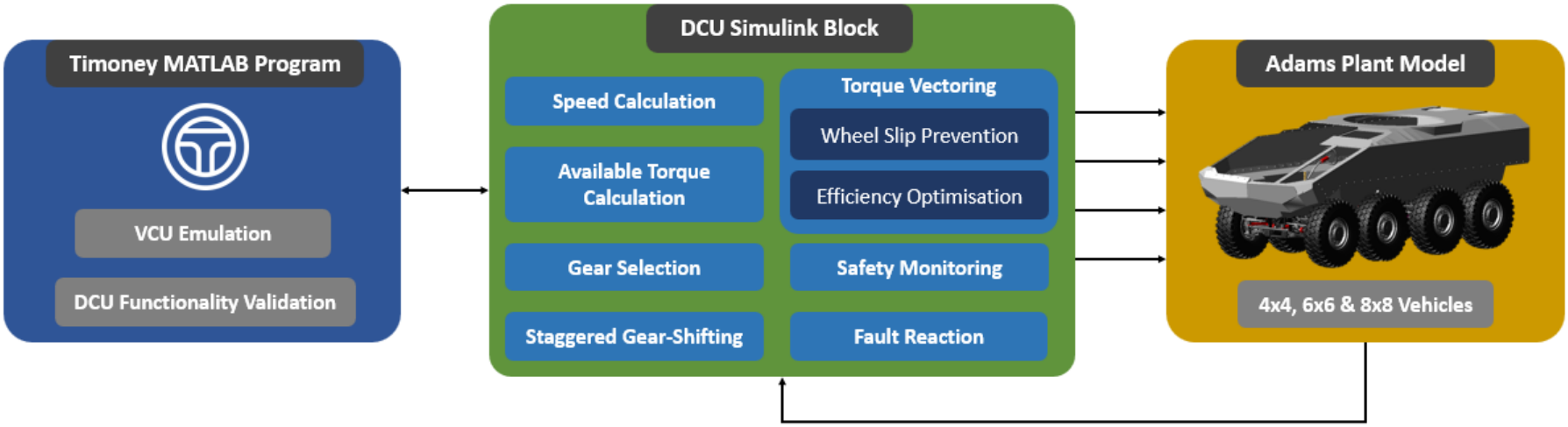



Fig. 5.13. DCU development and validation framework.

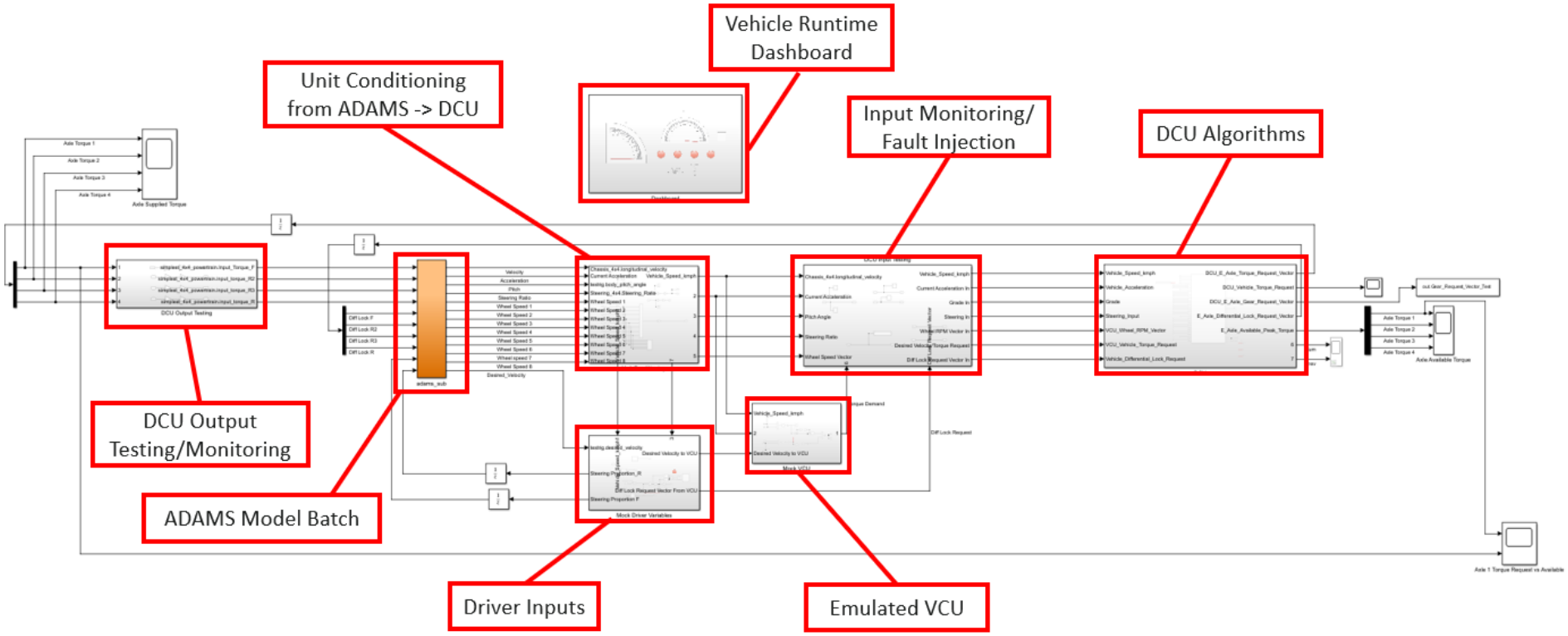



Fig. 5.14. DCU development and validation Simulink model.

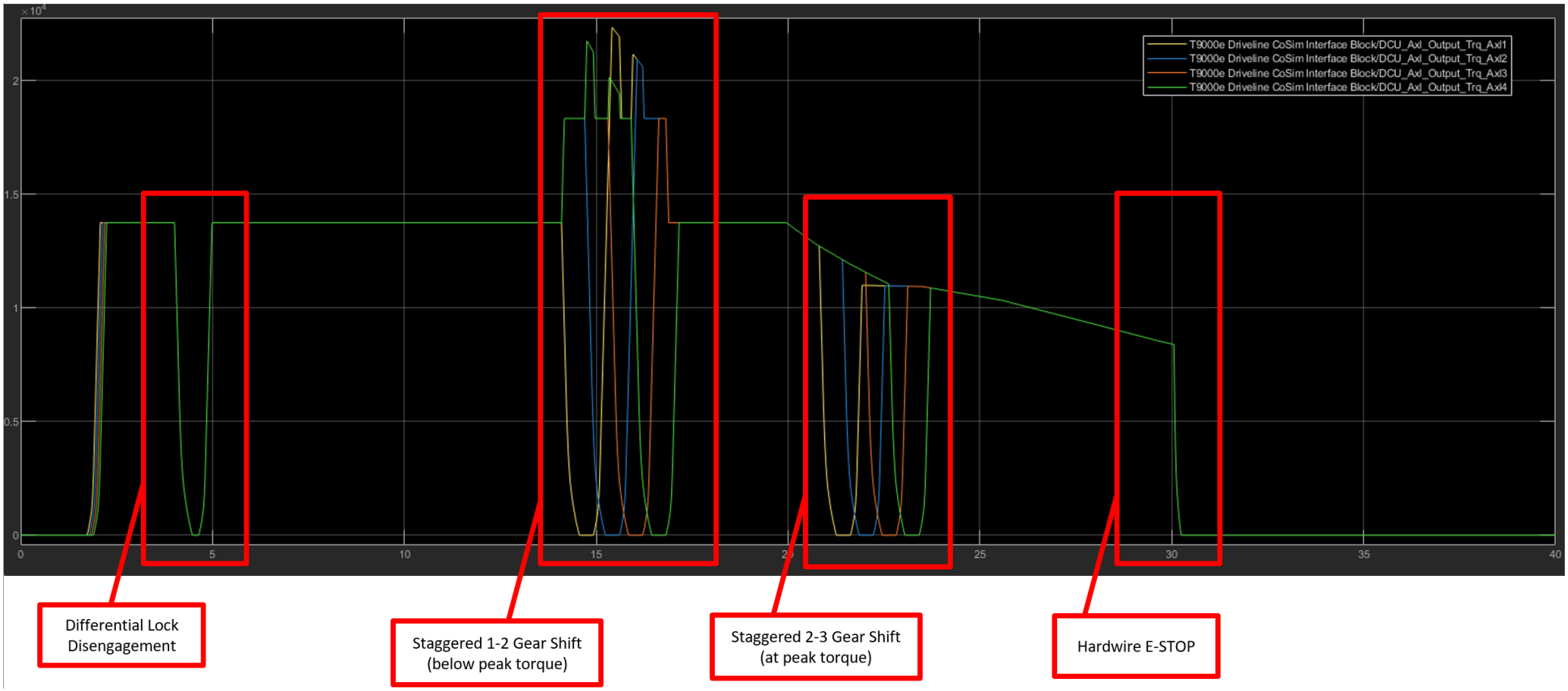



Fig. 5.15: DCU acceleration test for an 8x8 vehicle.

In the acceleration test in Fig. 5.15, the vehicle starts at zero-speed with the differential locks engaged on all eAxles. Note that this vehicle uses a single pneumatic valve to actuate all four differential locks, so staggered differential lock actuation is not applied here.

A constant driveline torque request of 55 kN m is sent to the DCU after 2 seconds and maintained throughout the test. The vehicle begins to accelerate, and the differential locks are disengaged after 4 seconds. The torque reduction state machine discussed in relation to gear selection in Section 5.6 is used to control the torque ramp-down, differential lock disengagement and torque ramp-up. The same ramp-rates are used for differential lock actuation and gear selection. The ramp-rate decreases as torque decreases to ensure that torque changes near 0 N m are sufficiently low to prevent gear wear and excessive acoustic noise caused by teeth coming in and out of contact when torque is removed.

After approximately 14 seconds, the gear selection algorithm initiates a staggered gear shift from first gear into second gear across the four axles. The torque reduction state machine is used to control the torque ramp-rates and gear selection requests are sent to the EACUs. As the driveline torque request is less than the available driveline torque, the torque delivered by the eAxles that are not completing a gear shift increases to maintain the driveline torque request. The staggered gear shift completes after approximately 17.5 seconds.

The vehicle continues to accelerate. After 20 seconds the driveline can no longer match the 55 kN m driveline torque request and the torque delivered reduces as speed increases. This behaviour is typical of a traction machine operating in field-weakening mode above its base/rated speed [1].

After 21 seconds the staggered gear selection algorithm begins a staggered gear shift from second gear to third gear. Again, the torque reduction state machine is used to control the torque ramp-rates, and the delivery of the gear selection requests to the EACUs. On this occasion, it is not possible to increase the torque of the eAxles not completing a gear shift as they are already delivering their maximum available torque. The staggered gear shift completes after approximately 23.5 seconds.

After 30 seconds, a hard-wire E-STOP request is applied. This results each eAxle's torque ramping down at an increased ramp-rate. Note that for redundancy purposes, the DCU features a hard-wire E-STOP and a CAN E-STOP. The hard-wire E-STOP is configured as a soft E-STOP which applies the increased ramp-rate discussed above. The CAN E-STOP can request either a soft E-STOP or a hard E-STOP. A hard E-STOP results in an immediate 0 N m torque request (i.e. no ramp-rate limits are applied).

### 5.7.2 HARDWARE-IN-THE-LOOP TESTING

Once the algorithms are verified and tuned in software, MATLAB's Vehicle Network Toolbox is used to communicate with the DCU hardware via a 6-channel CAN-USB interface. The hardware test setup allowed for verification of emergency stop functionality and CAN end-to-end protection of the algorithms' performance in real-time, measurement of the CAN bus loading and further fault injection testing. The DCU hardware in the loop setup (without EACU hardware) is shown in Fig. 5.16.

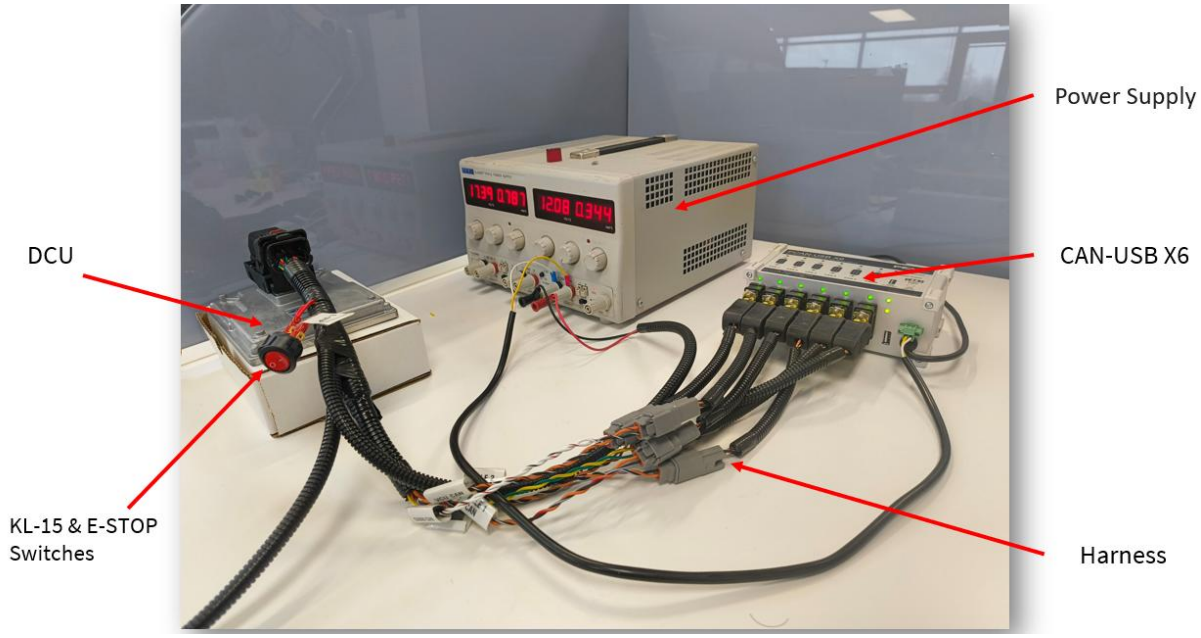



Fig. 5.16. DCU hardware-in-the-loop test setup.

## 5.8 CONCLUSIONS

This chapter discusses the development driveline control algorithms for the coordination of multiple modular eAxles on 4x4, 6x6 and 8x8 vehicles. The main DCU algorithms include speed calculation, available torque calculation, torque vectoring gear selection and staggered gear-shifting. Some key DCU features include longitudinal torque vectoring and driveline efficiency optimization, efficiency-optimized automatic gear selection, the hardware and algorithms are developed to meet ISO-26262 functional safety standards, avoiding EACU pre-configuration, reducing VCU CAN bus requirements, allowing for the VCU control algorithm to be like that of a conventional vehicle and measurement of up to 8 wheel-speed sensors.

The DCU algorithms are continuously under test using hardware-in-the loop setups, bench testing with eAxles and installation on prototype vehicles. Future developments will include refinement of the algorithms and lookup tables based on feedback from vehicle commissioning and analysis of in-field

data, along with the control of upstream powertrain components including the engine, generator, battery pack and cooling system.

# 6 CONCLUSIONS AND FUTURE WORK

## 6.1 CONCLUSIONS

This aims and objectives of this thesis are to develop a modular eAxle for all-terrain heavy-duty vehicle applications along with control strategies for multi-eAxle vehicles. The eAxle is developed for 4x4, 6x6 and 8x8 drivelines but can also be used in vehicles where not all axles are powered, such as 6x4 and 8x6 vehicle configurations. The eAxle utilises an existing independent suspension system, is interchangeable with an existing mechanical axle and can be used in multiple on-road and off-road applications, including agriculture, construction vehicles, forest machinery, fire trucks and mining and powered trailers. The eAxle is compatible with series-hybrid, battery-electric and hydrogen fuel cell powertrains.

Chapter 2 documents the design and test of the 9 tonne eAxle with a focus on novel weight-transfer based powertrain sizing methods and validation through dynamometer testing. The powertrain was sized based on the tractive effort requirements of a 27-tonne 6x6 vehicle along with several other potential applications. A novel method considering weight transfer on gradients and wheel-slip limitations is developed for sizing the powertrain. Considering weight transfer ensures that the powertrain is not undersized for grade-climbing. The performance of the 6x6 vehicle is evaluated for constant-speed operating points and transient accelerations. The sizing of the powertrain is verified through a comprehensive dynamometer testing program focusing on worst-case operating points. The eAxle is now in use on a variety of prototype vehicles at different customer locations.

Chapter 3 focuses on a novel eAxle powertrain layout using an over-the-shoulder architecture where the eAxle's motor and transmission are placed on the opposite side of the differential to the pinion gear that drives it. Such packaging allows for a more symmetrical eAxle relative to its driveshafts which is crucial for meeting short vehicle wheelbase requirements. The over-the-shoulder concept enables auxiliary kits and drives to be mounted on the pinion-gear side of the differential. The kits include inboard parking brakes and ground-driven steering pumps, both of which are essential to for vehicle safety and redundancy. The eAxle can be positioned in the vehicle with its motor facing either forwards or rearwards. Varying the orientation of eAxles is helpful for accommodating other driveline components around and meeting requirements for maximum approach and departure angles. A patent application for the novel over-the-shoulder packaging concept [42] was submitted on June 5$^{th}$, 2024. The expected publication date is December 5$^{th}$, 2025, 18 months after the original submission date.

Efficiency-optimized gear selection strategies for the eAxle are discussed in Chapter 4. Raw power loss data, provided by the inverter and motor system supplier is analysed and post-processed for usability. When combined with the eAxle's drivetrain efficiency, these are used to produce power loss and efficiency maps for the eAxle in each of its gears. The per-gear efficiency maps were interpolated onto a common set of lookup vectors allowing the most efficient gear for each operating point to be selected.

The resulting gear selection map is used to inform the design of efficiency-derived upshift and downshift gear selection curves. The benefits of gear-shift hysteresis and debounce are demonstrated in simulation. The performance of the gear selection strategy curves and the durability of the transmission's components are verified through dynamometer testing. The program included several acceleration and regenerative braking cycles. The eAxle is in use on prototype vehicles in varying applications. This allows the performance of the automatic gear selection strategy to be evaluated in the field.

Chapter 5 gives an overview of driveline control strategies implemented on multi-eAxle vehicles. The algorithms are implemented on a DCU that acts as an interface between the VCU and each eAxle. The key algorithms include speed calculation, available torque calculation, torque vectoring gear selection and staggered gear shifting. The DCU's main features are longitudinal torque vectoring, driveline efficiency optimization, automatic gear selection, avoiding EACU pre-configuration, reducing VCU CAN bus requirements, allowing for the VCU control algorithm to be like that of a conventional vehicle and measurement of up to 8 wheel-speed sensors. The DCU has been developed with ISO-26262 ASIL-C intent. The DCU algorithms are continuously under test using co-simulation and hardware-in-the loop setups.

## 6.2 LIMITATIONS AND FUTURE WORK

Future work on the topics of chapter 2 will include applying the powertrain sizing methodology to the design of eAxles for lighter weight classes, along with further evaluation of the powertrain performance of the current eAxle using results from in-field testing where the performance of the eAxle in various ambient operating conditions is of particular interest. Future work on eAxle packaging will include integrating the latest state-of-the-art powertrain components into the eAxle package along. Continuing to innovate will bring new features and benefits, further exploiting the packaging concept presented in chapter 3. Future work on the topic of chapter 4 will include tuning of the upshift and downshift curves to suit vehicle applications. It would be useful to characterize of the efficiency of the inverter and motor system along with the eAxle drivetrain. Adding a third torque meter to the dynamometer test setup between the motor output and the transmission input would allow a more accurate motor torque and power measurements to be taken. This would provide accurate power loss data to inform efficiency calculations. Future DCU developments include the refining of the algorithms and the tuning of lookup tables based on feedback from vehicle applications and analysis of in-field data. The DCU's functionality will be expanded to control the upstream powertrain components including the ICE, generator, battery pack and cooling system.

## REFERENCES


[1] J. G. Hayes and G. A. Goodarzi, Electric Powertrain: Energy Systems, Power Electronics and Drives for Hybrid, Electric and Fuel Cell Vehicles, John Wiley & Sons, 2018.

[2] M. Ehsani, Y. Gao, S. Longo and K. M. Embrahimi, Modern Electric, Hybrid Electric and Fuel Cell Vehicles, 3rd ed., CRC Press, 2018.

[3] C. Healy and J. G. Hayes, "Design and Test of a Modular 200 kW eAxle for All-Terrain Heavy-Duty Vehicle Applications," *IEEE Transactions on Transportation Electrification,* under review.

[4] C. Healy and J. G. Hayes, "Design of a modular e-axle for all-terrain heavy-duty applications considering gradient weight transfer," in *IEEE Transportation Electrification Conference and Expo*, 2023.

[5] Timoney Technology, "Timoney - Vehicle Design Specialists," [Online]. Available: https://www.timoneygroup.com/. [Accessed 05 05 2025].

[6] C. Healy and J. G. Hayes, "An efficiency optimized automatic gear selection map for a 200 kW modular eAxle," *IEEE Transactions on Transportation Electrification,* under review.

[7] C. Healy and J. G. Hayes, "An efficiency optimized gear-shift map to maximise the performance of a modular e-axle," in *International Scientific Conference on Electric Power Engineering (EPE)*, 2024.

[8] Volvo Trucks, "Volvo Trucks presents a new fully electric axle for extended range," [Online]. Available: https://www.volvotrucks.com/en-en/news-stories/press-releases/2022/sep/volvo-trucks-presents-a-new-fully-electric-axle-for-extended-range.html. [Accessed 05 05 2025].

[9] Merritor, "14XeTM," [Online]. Available: https://www.cummins.com/components/drivetrain-systems/epowertrains/14xe. [Accessed 05 05 2025].

[10] ZF Group, "ZF CeTrax 2 Dual," [Online]. Available: https://www.zf.com/products/en/cv/products_72192.html#details_divider658792. [Accessed 05 05 2025].

[11] Dana, "Dana Electrified," [Online]. Available: https://www.dana.com/e-mobility/. [Accessed 05 05 2025].

[12] Allison, “Allison eGEN,” [Online]. Available: https://www.allisontransmission.com/applications--products/products/egen-power. [Accessed 05 05 2025].

[13] Kessler & Co. GmbH, “E-Mobility Systems,” [Online]. Available: https://kessler-co.com/en/e-mobility. [Accessed 05 05 2025].

[14] ABB, “ABB Motors for heavy electric vehicles,” [Online]. Available: https://new.abb.com/motors-generators/iec-low-voltage-motors/heavy-electric-vehicles. [Accessed 05 05 2025].

[15] Danfoss, “Electric Machines,” [Online]. Available: https://www.danfoss.com/en/products/dps/electric-converters-and-machines/electric-converters-and-machines/electric-machines/#tab-overview. [Accessed 05 05 2025].

[16] Borg Warner, “Electric Drive Motors,” [Online]. Available: https://www.borgwarner.com/technologies/electric-drive-motors. [Accessed 05 05 2025].

[17] S. Janardhann, L. Laine, M. Jonasson, B. Jacobson and M. Alaküla, “Concept design of electric cruise and startability axles for long haul heavy vehicles to maximise driving range,” in *IEEE Vehicle Power and Propulsion Conference (VPPC)*, 2021.

[18] A. Belyaev, S. Manyanin, A. Tumasov, V. Makarov and V. Belyakov, “Development of 8x8 all-terrain vehicle with individual wheel drive,” in *International Conference on Vehicle Technology and Intelligent Transport Systems (VEHITS)*, 2019.

[19] D. Jin, Z. Wang and J. Wang, “Lightweight design and optimization of three-speed electric drive axle,” in *IOP Conference Series: Earth and Environmental Science*, 2020.

[20] L. Jin, D. Tian, Q. Zhang and J. Wang, “Optimal torque distribution control of multi-axle electric vehicles with in-wheel motors based on DDPG algorithm,” *Energies,* vol. 13, no. 1331, 2020.

[21] W. Liu, A. Khajepour, H. Hongwen, H. Wang and Y. Huang, “Integrated torque vectoring control for a three-axle electric bus based on holistic cornering control method,” *IEEE Transactions on Vehicular Technology,* vol. 67, no. 4, pp. 2921-2933, 2018.

[22] D. Seward, Race Car Design, Red Globe Press, 2014.

[23] Eaton, “Heavy duty 4-speed EV transmission,” [Online]. Available: https://www.eaton.com/gb/en-gb/catalog/emobility/hd-ev-transmission.html. [Accessed 05 05 2025].

[24] V. Mali, A. Mache, R. Mulik and S. Ramasi, “Design methodology for gear shift map of automated manual transmission,” *Materials Today,* vol. 5, no. 11, pp. 23898-23907, 2018.

[25] A. Fofana, O. Hass, V. Ersanill, K. Burnham, J. Mahtani, C. Woolley and K. Vithanage, “Multi-objective genetic algorithm for an automatic transmission gear shift map,” *IFAC-PapersOnLine,* vol. 69, no. 3, pp. 123-128, 2016.

[26] G. Li, D. Görges and M. Wang, “Online optimization of gear shift and velocity for eco-driving using adaptive dynamic programming,” *IEEE Transactions on Intelligent Vehicles,* vol. 7, no. 1, pp. 123-132, 2022.

[27] A. S. Vashurin, A. V. Tumasov, E. V. Stepanov, A. D. Yarzhemskii and E. I. Toperov, “Optimizing Gear Shifts in an Automatic Transmission for Light Commercial Vehicles,” *Russian Engineering Research,* vol. 43, no. 7, pp. 877-882, 2023.

[28] D. Jeoung, K. Min and M. Sunwoo, “Automatic Transmission Shift Strategy Based on Greedy Algorithm Using Predicted Velocity,” *International Journal of Automotive Technology,* vol. 21, no. 1, pp. 159-168, 2020.

[29] F. A. Machado, P. J. Kollmeyer, D. G. Barroso and A. Emadi, “Multi-speed gearboxes for battery electric vehicles: Current status and future trends,” *IEEE Open Journal of Vehicular Technology,* vol. 2, no. 1, pp. 419-435, 2021.

[30] C. T. Nguyen, P. D. Walker and N. Zhang, “Optimization and coordinated control of gear shift and mode transition for a dual-motor electric vehicle,” *Mechanical Systems and Signal Processing,* vol. 158, 2021.

[31] B. Gao, Q. Liang, Y. Xiang and L. Gao, “Gear ratio optimization and shift control of 2-speed I-AMT in electric vehicle,” *Mechanical Systems and Signal Processing,* vol. 137, no. 6, pp. 615-631, 2015.

[32] Y. Lee, Y. kim and K. nam, “Loss Minimizing Gear Shifting Algorithm based on Optimal Current Sets for IPMSM,” in *IEEE Transportation Electrification Conference and Expo (ITEC)*, 2017.

[33] Tesla, “Cybertruck,” [Online]. Available: https://www.tesla.com/cybertruck. [Accessed 22 03 2025].

[34] Ford, “F-150 Lightning,” [Online]. Available: https://www.ford.com/trucks/f150/f150-lightning. [Accessed 22 03 2025].

[35] Rivian, “R1T,” [Online]. Available: https://www.rivian.com/R1T. [Accessed 22 03 2025].

[36] Tesla, “Semi,” [Online]. Available: https://www.tesla.com/semi. [Accessed 22 03 2025].

[37] Mercedes-Benz, “eActros 600,” [Online]. Available: https://www.mercedes-benz-trucks.com/gb/en/trucks/eactros-600. [Accessed 22 03 2025].

[38] S. Singh, N. Endla, A. Arya, S. Anad, K. Chatterjee, S. Gopalan and S. Sirur, “Improving anti-slip performance in multi-motor single inverter based heavy electric vehicle,” in *IEEE Transportation Electrication Conference and Expo*, 2024.

[39] D. Savitski, V. Ivanov, K. Augsburg, T. Emmei, H. Fuse and H. Fujimoto, “Wheel slip control for the electric vehicle with inwheel,” *IEEE Transactions on Industrial Electronics,* vol. 67, no. 10, pp. 8535-8544, 2020.

[40] I. Aghabali, J. Bauman, P. J. Kollmeyer, Y. Wang, B. Bilgin and A. Emadi, “800-V electric vehicle powertrains: Review and analysis of,” *IEEE Transactions on Transportation Electrification,* vol. 7, no. 3, pp. 927-948, 2021.

[41] J. Malavatu, S. R. Kandke, S. Gupta and B. Agrawal, “Design challenges in electrification of off-highway applications,” in *IEEE Transportation Electrification Conference (ITEC-India)*, 2019.

[42] C. Healy, D. McCarry, M. Doody and G. Fitzpatrick, “An eAxle”. United Kingdom Patent GB2408020.2, 05 06 2025, to be publshed.

[43] N. Mohan and S. Raju, Analysis and Control of Electric Drives, 2021: John Wiley & Sons.

[44] N. Abhay, J. Dong, P. Bauer and S. Nouws, “Efficiency Map based Modelling of Electric Drive for Heavy Duty Electric Vehicles and Sensitivity Analysis,” in *IEEE Transportation Electrification Conference & Expo (ITEC)*, 2021.

[45] C. Healy and J. G. Hayes, “Speed vectoring algorithms for drivelines with multiple modular e-axles,” in *International Scientific Conference on Electric Power Engineering (EPE)*, 2024.

[46] International Standardization Organization, “Road Vehicles - Controller Area Network (CAN) - ISO 11898-1”.

[47] Society of Automotive Engineers, “Serial Control and Communications Heavy-Duty Vehicle Network - Top-Level Document - J1939”.

[48] International Standardization Organization, “Road Vehicles - Functional Safety - ISO 26262-18,” 2018.

[49] T. D. Gillespie, Fundamentals of Vehicle Dynamics, SAE International, 1992.